

## **RENSIT: RadioElectronics. NanoSystems. Information Technologies**

Journal "Radioelectronics. Nanosystems. Information Technologies" (abbr. RENSIT) publishes original articles, reviews and brief reports, not previously published, on topical problems in **radioelectronics (including biomedical) and fundamentals of information, nano- and biotechnologies and adjacent areas of physics and mathematics.**

Designed for **researchers, graduate students, physics students of senior courses and teachers.**  
It turns out **2 times a year** (that includes 2 issues)

Authors of journal are academicians, corresponding members and foreign members of Russian Academy of Natural Sciences (RANS) and their colleagues, as well as other russian and foreign authors on presentation of their manuscripts by the members of RANS, which can be obtained by authors before sending articles to editors.  
And also after its receiving - on recommendation of a member of editorial board of journal, or another member of Academy of Natural Sciences, that gave her opinion on article at request of editor.  
The editors will accept articles in both **Russian and English** languages.

Articles are internally peer reviewed (**double-blind peer review**) by members of the Editorial Board.  
Some articles undergo external review, if necessary.

Journal RENSIT is included in the **DB SCOPUS, EBSCO Publishing**, in the international abstracts database - **Ulrich's International Periodicals Directory**, (USA, New York, <http://www.ulrichsweb.com>), in the **AJ and DB VINITI RAS** (<http://www.viniti.ru>), and DB **Russian Science Citation Index (RSCI)** ([http://elibrary.ru/project\\_risc.asp](http://elibrary.ru/project_risc.asp)).

**Full-text content** is posted in the DB of the **Russian Scientific Electronic Library** - information resource on the Internet <http://elibrary.ru> and is available for registered users.  
And also - in Open Access **CyberLeninka NEB** of Russian Federation <http://cyberleninka.ru>.

On journal's website <http://www.rensit.ru> posted metadata publications and **RENSIT: Radioelectronics. Nanosystems. Information Technologies - english version** (cover-to-cover translation) of journal, which is a party to **CrossRef**.

---

The founder - the **Russian Academy of Natural Sciences**  
Publisher - Publishing Center of the Russian Academy of Natural Sciences  
Publisher Address: 29/16, Sivtsev Vrazhek lane, Moscow 119002, Russian Federation

## CONTENTS

### PREFACE TO ISSUE

RESEARCH IN THE FRYAZINO BRANCH OF THE KOTELNIKOV INSTITUTE OF RAS ON RADIOLOCATION AND INFORMATION TECHNOLOGIES

Lev E. Nazarov, Vladimir M. Smirnov ..... 3

### RADIOLOCATION

RADIO OCCULTATION ON THE VENERA-D MISSION: A CONCEPT OF RADIO FREQUENCY SUBSYSTEM AND RADIO SCIENCE TECHNIQUE

Anatoly L. Gavrik, Sergey F. Kolomiets, Yaroslav A. Ilyushin, Mikhail I. Bondarenko, Lyudmila A. Lukanina, Tatiana F. Kopnina ..... 5

SPATIAL-TEMPORAL CONDITIONS OF THE MOON BISTATIC SOUNDING

Olga V. Yushkova, Vyacheslav V. Yushkov, Roman A. Rudamenko, Taisiya N. Dymova ..... 13

BACKSCATTERING FROM THE NEAR-SURFACE LAYER OF THAWED/FROZEN SOILS OF ALASKA FROM SENTINEL 1 RADAR DATA

Natali V. Rodionova ..... 21

POTENTIAL OF PHASE MEASUREMENTS IN RADAR INTERFEROMETRY FOR THE OBSERVATION OF EMERGENCY SITUATIONS BUREYA LANDSLIDE CASE

Alexander I. Zakharov, Liudmila N. Zakharova ..... 31

MICROWAVE SCATTERING IN DRY LAYERED SNOW

Valery A. Golunov ..... 39

SEASONAL VARIATIONS OF VEGETATION COVER SCATTERING PROPERTIES

Liudmila N. Zakharova, Alexander I. Zakharov ..... 49

### INFORMATION TECHNOLOGIES

THE SCINTILLATION MODELS FOR SIGNAL PROPAGATION THROUGH SATELLITE IONOSPHERIC CHANNELS

Lev E. Nazarov, Dmitry V. Antonov, Vitaly V. Batanov, Andrey S. Zudilin, Vladimir M. Smirnov ..... 57

THE INVESTIGATION OF IONOSPHERIC CHANNEL INFLUENCES FOR PHASED SHIFT KEYING DIGITAL SIGNAL

Lev E. Nazarov, Vitaly V. Batanov ..... 65

POLARIZATION-ANGULAR DEPENDENCES OF THE REFLECTION AND TRANSMISSION COEFFICIENTS OF FREE PLATES OF QUASI-ANISOTROPIC ICE IN THE L-RANGE

Mikhail G. Evtikhov, Galina V. Arzamastseva ..... 73

COMPARISON OF INTERPOLATION METHODS WHEN ACHIEVING SUPER-RESOLUTION OF IMAGES BASED ON THE ANALYSIS OF SEVERAL FRAMES.

Alexander V. Kokoshkin, Vadim A. Korotkov, Evgeny P. Novichikhin ..... 85

### CHRONICLE

THIRD RUSSIAN CONFERENCE "GRAPHENE: A MOLECULE AND 2D CRYSTAL", Novosibirsk, 5-9 August 2019

Alexander V. Okotrub, Yuliya V. Fedoseeva ..... 92



RUSSIAN ACADEMY  
OF NATURAL SCIENCES

DEPARTMENT OF  
RADIOELECTRONICS,  
NANOPHYSICS AND  
INFORMATION TECHNOLOGIES  
PROBLEMS

# RENSIT:

**RADIOELECTRONICS,  
NANOSYSTEMS,  
INFORMATION  
TECHNOLOGIES.**

**2019, VOL. 11, № 1**

FOUNDED IN 2009

2 ISSUES PER YEAR

MOSCOW

*Editor-in-Chief*

VLADIMIR I. GRACHEV  
grachev@cplire.ru

*Executive Secretary*

ROSTISLAV V. BELYAEV  
belyaev@cplire.ru

EDITORIAL COUNCIL

Chairman

Alexander S. Ilyushin

Deputy Chairman

Sergey P. Gubin

Anatoly V. Andreev

Vitaly A. Barishpolets

Oleg V. Betzkiy

Vladimir A. Bushuev - deputy chief

Vladimir A. Cherepenin

Alexander S. Dmitriev

Yuri K. Fetisov

Yaroslav A. Ilyushin

Anatoly V. Kozar

Vladimir V. Kolesov - deputy chief

Albina A. Kornilova

Vladimir A. Makarov

Aleksey P. Oreshko

Andrey I. Panas

Igor B. Petrov

Vyacheslav S. Rusakov

Alexander S. Sigov

Valentine M. Silonov

Eugeny S. Soldatov

Lkhamsuren Enkhtor (Mongolia)

Yoshiyuki Kawazoe (Japan)

Kayrat K. Kadyrzhanov (Kazakhstan)

Peter Paul Mac Kenn (USA)

Deleg Sangaa (Mongolia)

Andre Skirtach (Belgium)

Enrico Verona (Italy)

Eugeny V. Ushpurus (Republic  
of Lithuania)

ISSN 2414-1267

The journal on-line is registered by the Ministry of Telecom and Mass Communications of the Russian Federation. Certificate EL no. FS77-60275 on 19.12.2014

All rights reserved. No part of this publication may be reproduced in any form or by any means without permission in writing from the publisher.

©RANS 2019

EDITORIAL BOARD ADDRESS

218-219 of., 7 b., 11, Mokhovaya str.,  
125009 MOSCOW, RUSSIAN FEDERATION,  
TEL. +7 495 629 3368

FAX +7 495 629 3678 FOR GRACHEV

From the Editors

*This issue of RENSIT is devoted to the works of the Fryazino Branch of the Kotelnikov Institute Radioengineering and Electronics of RAS*

---

## RESEARCH IN THE FRYAZINO BRANCH OF THE KOTELNIKOV INSTITUTE OF RAS ON RADIOLOCATION AND INFORMATION TECHNOLOGIES

Lev E. Nazarov, Vladimir M. Smirnov

Kotelnikov Institute of Radioengineering and Electronics of RAS, Fryazino branch, <http://fire.relarn.ru>  
Fryazino 141190, Moscow region, Russian Federation

[levnaz2018@mail.ru](mailto:levnaz2018@mail.ru), [vsmirnov@sunclass.ire.rssi.ru](mailto:vsmirnov@sunclass.ire.rssi.ru)

---

**Abstract.** The information on the publication of a number of works in the Fryazino branch of the Kotelnikov Institute (FIRE) of RAS on Radiolocation and Information Technologies, dedicated to the 160th anniversary of the birth of the outstanding Russian scientist, inventor of the radio Alexander S. Popov. A selection of publications presents inevitably to the limited range of work carried out in FIRE on this topics, however, it reflects their diversity and level.

*Keywords:* radar, radio sounding of planets, radiophysical technologies, information technologies

**PACS 01.10 VF**

*Received 23.04.2019, accepted 26.04.2019*

*RENSIT*, 2019, 11(1):3-4

**DOI: 10.17725/rensit.2019.11.003**

---

In 2019, the 160th anniversary of the birth of the outstanding Russian scientist, radio inventor Alexander Stepanovich Popov (1859-1905) is celebrated. Creation and public demonstration of A.S. On May 7, 1895, the Popov wireless radio system laid the foundation for the emergence and development of many completely new ideas and scientific directions on the theory and methods of transmitting and processing information, on radiolocation, on studying radio channels of transmission, on radiophysical methods of remote sensing of the earth's surface, on radiophysical technologies of research planets and the sun. Each of these areas includes a complex independent set of scientific and technical problems, the solutions of which are relevant to the present time when creating terrestrial and satellite communication systems based on developed mathematical theories; in the development and creation of radar systems, in particular, remote sensing systems (Earth remote sensing) and systems of radiophysical studies of the planets of the solar system; with the development of information technology. The structural appearance of these systems implements the approach of integrating and combining a number of functional components of subsystems

of various purposes and levels - the transfer of information in digital format using the methods of noise protection; archiving, storage and processing of information; adaptability in order to reduce the distorting effects of transmission channels of various physical nature; probing technologies and techniques for the thematic processing of remote sensing data and radiophysical studies of the planets; software and hardware implementation of systems, etc.

The activities of the divisions of radio engineering FIRA them. VA Kotelnikov of the Russian Academy of Sciences from the moment of its formation to the present is closely connected with the solution of these complex problems. Scientific radio engineering studies currently being conducted are based on the fundamental work of the Institute's staff, who conceptually formed, headed and coordinated relevant thematic areas (V. Kotelnikov, N. Armand, G. M. Petrov, A. E. Basharinov, A. M. Shutko, V.M. Polyakov, A.V. Sokolov, O.I. Yakovlev, A.G. Paveliev, N.A. Savich, V.A. Andrianov, Yu.G. Tishchenko and many others).

This issue of the journal presents the work of the FIRE employees, whose scientific activities are related to the designated radio engineering topics.

Radiolocation and radio sounding of planets is an important and basic direction developed in FIRE. In the release of this direction is represented by two works.

In the article Gavrik A.L. with co-authors a number of tasks were formulated with co-authors on the subject of radio occultation experiments in the planned Venus-D mission, in particular, studying the propagation of wave processes from the atmosphere to the ionosphere of the planet Venus.

In the article Yushkova O.V. with co-authors, the problems of the bistatic radiolocation of the moon from the spacecraft were formulated with the aim of studying the physical parameters of its surface and the subsurface structure of the soil.

Earth remote sensing is a traditional and at the same time key research area of FIRE. One of its branches - active and passive sensing of earth covers - is presented in the issue with articles that show the results of studies of the most significant environments for human existence - vegetation and snow cover, the aquatic environment, and monitoring of emergency areas.

In the work of Rodionova N.V. outlines the results of using radar data from the Sentinel-1 satellite to determine the seasonal state of soil covers. The possibility of identification of thawed and frozen soils of Alaska in the upper 5 cm layer is shown, which is confirmed by the data of ground stations.

The features of seasonal variations in the radiophysical properties of the vegetation covers of the Transbaikalia according to the PALSAR cosmic polarimetric radar, including the reflective properties of trees and the dominant mechanisms of scattering of the probing signal by elements of crowns and trunks, are studied in the article Zakharova L.N. and Zakharov A.I. The significant effect of seasonal variations in air temperature on the signal reflection level and the nature of the dominant scattering mechanism is shown, which should be taken into account when building automated algorithms for classifying boreal forest types and evaluating their biophysical parameters.

The possibilities of phase methods, which form the basis of radar interferometry, for monitoring areas of emergency situations are disclosed in the article by A.I. Zakharov and Zakharova L.N. on the example of the processing of radar images of the

landslide coastal slope of the Bureya River from the Sentinel-1 satellite.

In the work of Golunov V.A. The results of theoretical and experimental radiophysical studies of the features of volume scattering and the formation of thermal radiation in dry, layered snow are presented.

In the work of Evtikhov M.G. and Arzamastseva G.V. algorithms have been developed for calculating the dependences of the reflection and transmission coefficients of free plates, which are applied in the L-range for quasi-anisotropic ice.

The scientific direction related to information technologies and developed at FIRE determines the creation and development of the theory and methods of transmitting information through various physical channels through the development of methods for processing, storing and archiving information, including images of remote sensing data in digital format, creating mathematical models and specialized software that implements the developed computational algorithms. In the issue this direction is represented by the work of Kokoshkin A.V. with co-authors (results are given on the development and computer simulation of an interpolation algorithm for solving the problem of achieving super-resolution of images in a digital format) and the works of Nazarov L.E. with co-authors (the results of theoretical and experimental studies of satellite radio lines regarding the estimation of energy losses due to the influence of signal fading (scintillation) and due to the influence of the Earth's ionosphere as a dispersion medium with respect to the propagation of signals in free space are given.

# RADIO OCCULTATION ON THE VENERA-D MISSION: A CONCEPT OF RADIO FREQUENCY SUBSYSTEM AND RADIO SCIENCE TECHNIQUE

Anatoly L. Gavrik, Sergey F. Kolomiets, Mikhail I. Bondarenko, Lyudmila A. Lukanina, Tatiana F. Kopnina

Kotelnikov Institute of Radioengineering and Electronics of RAS, Fryazino branch, <http://fire.relarn.ru>  
Fryazino 141190, Moscow region, Russian Federation

**Yaroslav A. Ilyushin**

Lomonosov Moscow State University, Physical Faculty, Atmospheric Physics Department, <http://atm563.phys.msu.ru>  
Moscow 119991, Russian Federation

Kotelnikov Institute of Radioengineering and Electronics of RAS, Fryazino branch, <http://fire.relarn.ru>  
Fryazino 141190, Moscow region, Russian Federation

[alg248@hotmail.com](mailto:alg248@hotmail.com), [bottom@mail.ru](mailto:bottom@mail.ru), [ilyushin@physics.msu.ru](mailto:ilyushin@physics.msu.ru), [linuxoid2013@mail.ru](mailto:linuxoid2013@mail.ru), [lukaninal@hotmail.com](mailto:lukaninal@hotmail.com), [tkopnina@hotmail.com](mailto:tkopnina@hotmail.com)

*Abstract.* Main goals of radio-occultation experiments in VENERA-D mission are formulated. It is shown, based on the results of radio-occultation experiments obtained earlier with high potential radio-links in the Venusian gaseous envelop, that using variations of power and frequency at two coherent radio waves, one can study a fine structure of refracting medium which may bring fundamentally new information about the atmosphere-ionosphere system of Venus. Given the accuracy of data interpretation depends on different high-frequency subsystem performance characteristics, it is shown that the prime direction of the development, must be the balanced increase of the energy potential of radio links and improving the stability of the oscillators used. A novel technique of data interpretation applicable to high potential measurements in the ionosphere and atmosphere of the planet is discussed. Among all the other things the suggested technique makes it possible to see and study propagation of disturbances from the atmosphere into the ionosphere. Moreover, it is shown that the correlation between amplitude and frequency of signals which is underpinning the technique mentioned can be seen as an effective criterion of the validity of geometrical optics spherically symmetrical approximations for the inverse problem solution.

*Keywords:* wave propagation, occultation, ionosphere and atmosphere of Venus

UDC 535.37:523.42

*Bibliography* - 15 references

*Received* 17.04.2019, *accepted* 23.04.2019

RENSIT, 2019, 11(1):5-12

DOI: 10.17725/rensit.2019.11.005

## CONTENTS

1. INTRODUCTION (5)
  2. TASKS OF RADIO OCCULTATION EXPERIMENTS IN THE VENUS-D MISSION (6)
  3. METHODS OF RADIO OCCULTATION EXPERIMENT (7)
  4. DATA PROCESSING TECHNIQUE (8)
  5. DIAGNOSTICS OF LAYERED STRUCTURES IN THE IONOSPHERE (9)
  6. CONCLUSION (11)
- REFERENCES (11)

## 1. INTRODUCTION

For several decades, radio occultation sounding has been developed as a diagnostic technology

for the gas envelopes of space objects: the Earth, planets, comets and the Sun [1]. Radio-occultation studies on Venus began in 1967 [2]. Thanks to the successful missions of the spacecraft (SC) MARINER-5,-10, VENUS-9,-10, PIONEER-VENUS, VENUS-15,-16, MAGELLAN, VENUS-EXPRESS, AKATSUKI, more than 1500 radio transmissions of the Venosphere and Venus atmosphere were conducted [3-9]. The amount of radio sounding data accumulated to date is relatively small (~1500 sessions), while the amount of radio sounding of the Martian

gas envelope exceeds 6000, the number of radio sounding of the near-earth shell is several thousand per day and several million sessions have been conducted.

Using the available experimental data, the structural characteristics of the ionosphere and the upper atmosphere of Venus were investigated and described in the literature [1-9]. These results cover a wide range of altitudes above the surface of the planet and solar activity. It is important to say that, although much is known about the Venus ionosphere, our understanding remains rather superficial in most aspects. Venus, like the Earth, is a complex world, and in order to take another step towards its adequate understanding, the planned mission of VENER-D [10] should focus on the issue of obtaining new data that are more likely to lead to new knowledge, and not only to the accumulation of measurement statistics using known tools and data analysis methods.

In the VENERA-D mission [10], our interest is focused on small-scale (from 0.5 km to 10 km) features of the ionosphere and atmosphere, as well as on processes that affect their structure. The most attractive are the least studied questions: the interaction between the lower ionosphere and the upper atmosphere of Venus, as well as wave processes both in the atmosphere and in the ionosphere. The experience of previous missions shows that, having sufficient energy potential of radio lines, it is possible to reveal the properties of all layers of the ionosphere [11], including by comparing radio occultation data with direct measurements of sensors installed on the orbital apparatus of the VENER-D project.

The analysis of radio-sounding data is usually performed in the approximation of geometric optics, and the dispersion interferometer method is used to separate radio effects from the ionosphere and atmosphere. The known integral relations describing the corresponding formulation of the inverse problem allow us to calculate the radial profiles of the electron

concentration in the ionosphere, density and temperature in a neutral atmosphere from changes in the frequency or power of the probing signals [1]. However, questions about the accuracy of the radio sounding method in determining the parameters of the atmosphere and the ionosphere are still relevant [12, 13], and the issues of extracting information about the gas envelope from experimental data require improving measurement techniques and analyzing experimental results [14].

The experience of all previous missions to Venus allows us to choose the optimal conditions for radio occultation experiments. The improved data processing model discussed in this article, applicable to the results of high-potential measurements, being the basis of the experiment, will provide new reliable data on the night ionosphere, on the lower part of the daytime ionosphere and on the propagation of disturbances from the atmosphere into the ionosphere. As a result, radio sounding using equipment installed on an orbiter in the VENER-D mission can be considered as one of the most inexpensive and reliable ways to obtain unknown and important information about the gas envelope of Venus.

## **2. TASKS OF RADIO REPLACEMENT EXPERIMENTS IN THE VENER-D MISSION**

Radiophysical studies in the VENERA-D mission can be carried out with coherent two-frequency radiation in the  $X$  (3.6 cm) and  $S$  (13.7 cm) bands with a high potential of radio lines. Three categories of experiment and observation are possible. First, the study of the planetary atmosphere and ionosphere. These measurements can be performed both with direct (implying that the transmitters are on board), and with reverse (transmitters on Earth) translucency. Secondly, studies of the so-called “bistatic scattering” properties, when the receiving station on Earth registers not only the direct signal from the spacecraft, but also

the signal reflected from the surface of Venus. Thirdly, the study of the properties of the solar wind and the solar corona using direct radio sound transmission with small periods of signal sampling, including its synchronous reception by several ground stations (interferometric reception). Thus, the following studies will be possible:

Obtain electron concentration data in the altitude range from ~70 km to ~1000 km and obtain data on temperature, density, and pressure in the atmosphere in the altitude range from ~40 km to ~100 km as a function of altitude, latitude, local time, and season.

The study of the dynamics of multilayer structures in the atmosphere and ionosphere of Venus, their connection with wave processes, solar activity and the flow of the solar wind.

Identification of links between processes in the ionosphere, the thermosphere and the lower atmosphere on the day and night side of Venus.

The study of the scattering properties of the surface of Venus, the dielectric constant and density of the soil, identifying areas with abnormal scattering coefficients.

Study of the dynamics of small-scale and large-scale inhomogeneities of interplanetary and near-solar plasma.

The study of the propagation of radio waves in space environments.

### 3. TECHNIQUE OF RADIO-CHANGING EXPERIMENT

The radio sounding scheme of the gas envelope of the planet is shown in Fig. 1. At

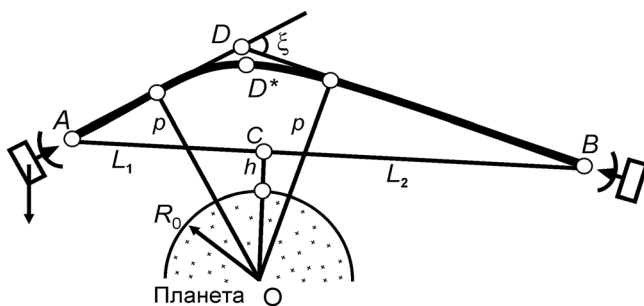


Fig. 1. Scheme of radio occultation experiment. The transmitter is at point A, the receiver is at point B. The curvature of the radio path AD\*B is due to the refraction of the radio wave in the gas envelope.

the beginning of the experiment, the radio path between the source and receiver of the signals passes above the ionopause. The orbiting object A emits signals received by the object B (the radial approximation relations used below are independent of the direction of radiation). It is assumed that the speed of the line of sight AB in the shell of the planet  $V = db/dt$  ( $b$  is the height of the line AB above the surface of the planet), as well as the distances CA and CB from the pericenter of the line AB to the radiator  $L_1$  and receiver  $L_2$  during the sensing process change slightly so the change of these parameters in the experiment can be neglected. In a spherically symmetric medium, the asymptotes AD and DB of the curved radio beam AD\*B have an impact parameter  $p(t)$ , the value of which, due to the small angle of refraction  $\xi(t)$ , is equal to the distance OD\* of the beam turning point. Such a model is permissible when probing the near-planetary environment of Venus above the cloud layer.

The transmitter KA emits two continuous coherent radio waves in the process of moving, the measuring system uses only limited portions of the radio field that fall into the aperture of the receiving antenna on the measurement time intervals  $\tau$ . The receiver determines the average for the time interval  $\tau$  the power of each signal, which is then normalized to the signal power level in the control area in the absence of the medium being probed. The recorded power variations of the signal  $Xap(t) = Xa(t) + Xp(t)$  are the sum of the changes in plasma power  $Xp(t)$  and in the neutral medium  $Xa(t)$ , which depend only on the deformation of the ray tube in the absence of absorption and scattering of radio waves. Near the lower boundary of the ionosphere it is unambiguous to separate  $Xp(t)$  and  $Xa(t)$  from the  $Xap(t)$  function [14]. The receiver also determines the increments for the time  $\tau$  of the phase  $\varphi(t)$  of each signal and calculates the instantaneous frequency  $f(t) = (2\pi)^{-1}d\varphi(t)/dt$ . The change in the frequency of the signal  $fap(t) = fa(t) + fp(t)$  is due to the

change in the angle of refraction  $\xi(t)$  when the radio beam is immersed in the shell of the planet containing neutral and ionized components (terms  $fa(t)$ ,  $fp(t)$ ). To isolate the plasma effect, the difference frequency  $\delta f(t)$  is calculated from data on the frequency variations of the received coherent signals  $f_D(t)$  and  $f_C(t)$ :

$$\delta f(t) = q^2 \cdot (q^2 - 1)^{-1} \cdot [f_D(t) - f_C(t) \cdot q^{-1}]. \quad (1)$$

In the case of rectilinear propagation of radio waves,  $\delta f(t)$  coincides with a change in the frequency of the low-frequency signal in the plasma  $fp(t)$  ( $q$  is the ratio of the high radiated frequency to the low frequency). In the Venus probed ionosphere, the trajectories of signals of different ranges pass at different heights, therefore  $fp(t)$  differs from  $\delta f(t)$ . A technique has been developed to restore  $fp(t)$  from variations  $\delta f(t)$ , the error in determining  $fp(t)$  does not exceed the amount of instrumental noise ( $10^{-2} \dots 3 \cdot 10^{-3}$  Hz at  $\tau = 1$ s) [6].

The experience of previous missions shows that the dynamic range of the radio links used must be at least 45 dB and be balanced. The latter is no less important for reliable data interpretation and requires ensuring the potential of both lines is high enough to prevent the noise of one of them from dominating the final results. Radio measurements in the VENERA-D mission imply the use of ground antennas with diameters of 70 and 64 m, and hydrogen maser receivers assembled according to a scheme that involves parallel implementation of recording signals in the  $X$  (3.6 cm) and  $S$  (13.7 cm) bands, as in a narrow band (with phase locked loop), and in a wide band. The latter allows one to expect reliable and interpretable signal registration, when its power is rather low for normal operation of the phase tracking subsystem.

To perform all the studies listed above, there must be a transmitter in the  $X$ -range of more than 30 W and no less than 40 W of the transmitter in the  $S$ -range. Both of them are expected to be well stabilized and effectively shielded to provide the required stability over time intervals from 0.05 s to 600 s, which correspond to the

typical duration of signal sampling periods in various radio-dark experiments. Considering that short-term frequency deviations can be directly projected onto the fine structure of the planetary environment, it is advisable to use on-board local oscillators with a frequency stability value no worse than  $10^{-12}$  for a time interval of up to 10 s. Thus, the main direction of development of a radio-technical complex that performs radio sounding experiments is to increase the energy potential of a radio link and to improve the stability of the equipment used, since the accuracy of the information in the interpretation of these radio insights depends on the relationship between the radiophysical effects caused by the medium under study and the interfering factors.

#### 4. DATA PROCESSING TECHNIQUE

The accuracy of determining the parameters of the atmosphere and ionosphere in solving the inverse problem of radio sounding is unsatisfactory in the region of the lower boundary of the ionosphere at altitudes from 75 km to 120 km [11]. To study the atmosphere-ionosphere system, a method using the main merit of radio sounding is necessary: continuous (within 2 ... 5 min) recording variations of the refraction angle  $\xi(t)$  from which the refractive index profile  $n(h)$  is calculated along the vertical from the upper ionosphere to the cloud layer the atmosphere. The ways to solve the inverse problem of radio sounding of the atmosphere and the ionosphere are different, but the principle of determining  $n(h)$  is based on the integral connections of the functions  $fa(t)$ ,  $Xa(t)$ ,  $fp(t)$ ,  $Xp(t)$  with the parameters of the medium being probed [15]. In [11], it was shown that the information obtained on the solution of the inverse problem of small variations  $n(h)$  is not always reliable. In particular, near the lower boundary of Venus's ionosphere in a region of  $\sim 40$  km (in the altitude range 75 ... 120 km), the insufficient accuracy of determining  $n(h)$  in the atmosphere and ionosphere limits the possibility of studying stratified layers.

The developed new method [11] uses the relation (1) to separate the effects of the atmosphere and the ionosphere, which distinguishes the plasma effect  $\delta f(t)$ . Using  $\delta f(t)$ , we calculate the frequency change due to the influence of the ionosphere  $f\dot{p}(t)$ , then from the function  $f_D(t)$  we determine the influence of the atmosphere  $f_a(t)$ . The functions  $f_a(t)$ ,  $Xa(t)$ ,  $f\dot{p}(t)$ ,  $Xp(t)$  are related to the refractive index  $n(h)$  of the medium being examined and the angle of refraction  $\xi(t)$  by well-known relations [15]. For a stratified non-absorbing radio wave medium having the property of spherical symmetry in a solid angle less than  $10^\circ$ , it is possible to obtain approximate formulas by eliminating from the multiparameter relations given in [15] all the terms whose contribution does not exceed random fluctuations. In this case, with  $L_2 \gg L_1$  and a small parameter  $\xi(t)$ , the following relations are valid:

$$Xap(t) = \{1 - L_1 \cdot d\xi(t)/dp\}^{-1}, \quad (2)$$

$$p(t) = R_0 + b(t) + L_1 \cdot \xi(t), \quad (3)$$

$$fap(t) = \xi(t) \cdot V \cdot L_1 \cdot \lambda^{-1}, \quad (4)$$

where  $R_0$  is the radius of the planet,  $\lambda$  is the length of the radio wave. The error of formulas (2) - (4) with  $\xi(t) < 10^{-3}$  rad,  $|n(h) - 1| < 10^{-4}$  does not exceed the distortion caused by noise.

Differentiation of formulas (3), (4) and their use to transform formula (2) allows to obtain the following relations:

$$dp(t)/dt = V \cdot Xap(t). \quad (5)$$

$$Xap(t) = 1 + [\lambda \cdot L_1 \cdot V^{-2}] \cdot dfap(t)/dt. \quad (6)$$

Formula (5) establishes a connection between the vertical component  $V$  of the speed of spacecraft and the speed of immersion of a curved radiobeam into the shell of the planet  $dp(t)/dt$ , this connection was previously detected experimentally, but the limits of applicability of the empirical formula in real experiments in studying thin layers remained unclear. The formula (5) obtained by the transformations of the known relations (2) - (4) proves the validity of its use for arbitrary variations of  $n(h)$  that do not violate the limitations of the ray approximation.

The relation (6) opens up prospects for solving new problems of diagnosing the atmosphere-ionosphere system. Using the non-energy signal parameters  $f_a(t)$ ,  $f\dot{p}(t)$ , one can calculate the predicted refractive changes by formula (6) and compare them with the energy parameters of the signals  $Xa(t)$ ,  $Xp(t)$ . The presence of correlation between measured and calculated parameters will allow to distinguish small variations of  $n(h)$  in the stratified layers of the atmosphere-ionosphere system against the background of similar-shaped interference, since random fluctuations of energy and non-energy parameters are statistically independent. The lack of correlation between variations of the measured and calculated parameters will indicate the dominant influence of noise and/or the inapplicability of the approximations used.

## 5. DIAGNOSTICS OF LAYERED STRUCTURES IN THE IONOSPHERE

The proposed method for analyzing radio-sounding data will provide important information on the propagation of disturbances in the gas envelope in the new mission to Venus. A reliable criterion for detecting stratified layers in the atmosphere is the coincidence of  $Xa(t)$  variations with measured functions  $X_D(t)$  or  $X_C(t)$ , and in the ionosphere the coincidence of  $Xp(t)$  variations with  $X_D(t)$  or  $X_C(t)$ . In addition, such coincidences will confirm the validity of applying the ray approximation and spherical symmetry in solving the inverse problem, since relation (6) is satisfied only within the framework of the adopted model. In experiments, one can observe a correlation of pulsations  $Xa(t)$ ,  $Xp(t)$ ,  $X_D(t)$ ,  $X_C(t)$ , which do not coincide in amplitude. In this case, the studied effects are masked by interfering factors, which include: an insufficiently short data sampling interval  $\tau$ , signal fluctuations due to noise or turbulence of the medium, absorption or scattering of radio waves, violation of the applicability of radiation approximation or spherical symmetry. In such cases, the interpretation of the data will require

careful analysis of possible sources of error and justification of the accuracy of the information obtained.

Using the data of the VENER-15,-16 missions and the original data processing methods, we finally managed to form a solid experimental basis for the above theoretical relationships and show that in the field of application of geometric optics, the energy flux density of signals in a medium with spherical symmetry changes in direct proportion wave vector [11]. This means that fluctuations of the signal power in experiments on radio sounding of the atmosphere and the ionosphere are directly correlated with the rate of change of frequency, since the medium can be considered as spherically symmetric due to the influence of the gravitational field. At the same time, true stochastic fluctuations (noise) of power and frequency are not correlated. Considering that this is a new way of presenting signals, it opens up prospects for the application of new data processing technology, which we hope will allow deeper penetration into the ionosphere and more reliably explore the processes of interaction between the atmosphere and the ionosphere, including the propagation of wave processes from the atmosphere into the ionosphere.

The effect underlying this study can be found in a spherically layered medium if the layers are sufficiently dense and the level of hardware noise is low, and diffraction and absorption of electromagnetic waves are absent. That is why the data from the VENUS-15,-16 missions, which operated at higher power and at a lower frequency than most other missions, were critically needed to test the concept of a new data processing technology. The most intriguing result obtained using data from the VENUS-15,-16 spacecraft is that the layered structures of the Venusian ionosphere are found and studied at extremely low altitudes 80...120 km above the surface of the planet, where the electron concentration is extremely small compared to the error of its determination in

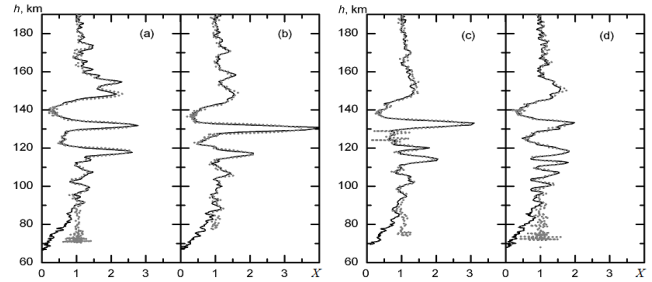


**Fig. 2.** Comparison of the refractive power change  $X_0(h)$  of a signal with a wavelength of 32 cm. Venus-15 spacecraft, -16 (solid curve) with the refractive change  $X_1(h)$  (gray dots) calculated from frequency data in four radio-echo sounding sessions. The vertical axis is the height of the radio beam above the surface of Venus.

the case of applying the traditional method of solving the inverse problem of radio sounding.

Typical stratified periodic variations of power  $X_0$  and  $X_1$  are presented in **Fig. 2** for four sessions of radio sounding. The idea of detecting ionospheric disturbances is to compare two diagrams with signal power values ( $X$  axis) along altitudes ( $Y$  axis), while one of them ( $X_0$ ) represents experimentally observed variations and fluctuations in signal power due to the influence of the ionosphere and atmosphere and the other ( $X_1$ ) means “prediction” of the same parameter calculated using relation (6) based on variations in the signal frequency in the ionosphere. It can be seen in Fig. 2 is a good match between the  $X_0$  and  $X_1$  diagrams in the altitude range of 90 to 180 km. Fluctuations above 180 km have a pure stochastic character, which indicates that this altitude interval does not contain detectable ionized layers with stable deviations of the average refractive index. As follows from Fig. 2, below 85 km, the plasma layers are also absent, and the attenuation of power during refraction in the atmosphere rapidly increases.

The variations of  $X_1(h)$  in Fig. 2 due to the rarefaction or concentration of the beam beams with a change in the refractive index in the ionosphere. At altitudes from 90 to 160 km, there is a correlation of  $X_0(h)$  with  $X_1(h)$ , reaching values of 0.9, which indicates the influence of the plasma layers and the absence of the influence

## RADIOLOCATION

of the atmosphere. The most important is the detection of alternation of maxima and minima of  $X_o(h)$  below 120 km, coinciding with  $X_i(h)$ , which indicates the presence of numerous stratified ionized structures in the Venusian lower daytime ionosphere. In foreign experiments on the radio sounding of the Venus ionosphere [2, 3, 5, 7, 8, 9], this effect was almost imperceptible due to the limited accuracy of the technique used. The detected periodic oscillations  $X_i(h)$ , which coincide with the oscillations  $X_o(h)$ , indicate the regular existence of stratified periodic perturbations  $n(h)$  due to fluctuations in the electron concentration in the lower boundary of the Venus ionosphere. This circumstance indicates the possibility of studying the interaction between the lower ionosphere and the upper atmosphere of Venus, and also opens up the prospect of studying wave processes both in the atmosphere and in the ionosphere in radio sound experiments of the planned VENERA-D mission.

### 6. CONCLUSION

To solve the fundamental problems of comparative planetology in the VENERA-D project, it is proposed to perform multiple radio-echo sounding of the Venosphere ionosphere and atmosphere, sounding of the surface of Venus using the method of bistatic radar, radio-sounding of the interplanetary medium and the near-solar plasma when Venus sets behind the Sun. The most important are the least studied issues: the interaction between the lower ionosphere and the upper atmosphere of Venus, as well as wave processes both in the atmosphere and in the ionosphere. The experience of previous missions showed that, having sufficient energy potential of radio lines, it is possible to reveal the properties of all layers of the ionosphere, including by comparing radio occultation measurements and data collected from instruments installed on the VENERA-E orbiter. It is shown that an improved data processing model applicable to high-potential

measurements, being the basis for the experiment, will provide new reliable information about the night ionosphere, the lower part of the daytime ionosphere and the distribution of disturbances from the atmosphere into the ionosphere. The presented analysis of radio-radiation data in the mission Venus-15,-16 indicates that the ionized layers constantly exist not only in the lower ionosphere of the Earth (in region  $D$ ), but also in the daytime ionosphere of Venus. A deeper investigation of the nature of such disturbances will be possible in the mission of VENERA-D. The proposed approach will allow us to study the fine structure of the interaction of the atmosphere and the ionosphere using variations in the power and frequency of two coherent signals. Optimization of the radio frequency subsystems on the basis of summarizing the experience of previous missions will effectively apply modern approaches to obtain fundamentally new information about the atmosphere and ionosphere of the planet, as well as about the state and dynamics of the plasma in the Solar System. As a result, new knowledge can be obtained on the propagation of disturbances from the atmosphere into the ionosphere, including the propagation of wave disturbances, the nature of which has not been studied to date.

### ACKNOWLEDGMENTS

*The work was performed within the framework of a state task and was partially supported by the Program of the Russian Academy of Sciences No. 28.*

### REFERENCES

1. Armand NA, Gulyaev YuV, Gavrik AL, Efimov AI, Matyugov SS, Pavel'ev AG, Savich NA, Samoznaev LN, Smirnov VM, Yakovlev OI. Results of solar wind and planetary ionosphere research using radiophysical methods. *Physics-Uspеkhi*, 2010, 53 (5):517-523.
2. Fjeldbo G, Kliore AJ, Eshleman VR. The Neutral Atmosphere. *The Astronomical Journal*, 1971, 76 (2):123-140.

3. Fjeldbo G, Seidel B, Sweetnam D, Hovard T. The Mariner 10 Radio Occultation Measurement of the Ionosphere of Venus. *Journal of the Atmospheric Sciences*, 1975, 32 (2):1232-1236.
4. Savich ON., Gavrik AL., Samoznaev LN. Analysis of diffusion processes in the daytime Venus ionosphere according to radio emission data of Venus-9,10 satellites. *Space research*, 1983, 21 (5):737-745.
5. Brace LH, Kliore AJ. The structure of the Venus ionosphere. *Space Science Reviews*, 1991, 55:81-163.
6. Gavrik AL, Gavrik YuA, Kopnina TF, Samoznaev LN. Variations of the amplitudes and frequencies of coherent radio signals when radiating Venus's daytime ionosphere. *Radioengineering and electronics*, 2010, 55(3):277-284.
7. Jenkins JM, Steffes PG, Hinson DP et al. Magellan spacecraft: 2. Results from the October 1991 experiments. *Icarus*, 1994, 110:79-94.
8. Gérard JC, Bougher SW, López-Valverde MA, Pätzold M, Drossart P, Piccioni G. Aeronomy of the Venus Upper Atmosphere. *Space Sci. Rev.*, 2017, 212 (3-4):1617-1683.
9. Imamura T, Ando H, Tellmann S, Pätzold M, Häusler B, Yamazaki A, Sato TM, Noguchi K, Futaana Y, Oschlisniok J, Limaye S, Choudhary RK, Murata Y, Takeuchi H, Hirose C, Ichikawa T, Toda T, Tomiki A, Abe T, Yamamoto Z, Noda H, Iwata T, Murakami S, Satoh T, Fukuhara T, Ogohara K, Sugiyama K, Kashimura H, Ohtsuki S, Takagi S, Yamamoto Y, Hirata N, Hashimoto GL, Yamada M, Suzuki M, Ishii N, Hayashiyama T, Lee YJ, Nakamura M. Venus orbiter mission Akatsuki. *Earth, Planets and Space*, 2017, 69 (1):137.
10. Glaze LS, Wilson CF, Zasova LV, Nakamura M, Limaye S. Future of Venus Research and Exploration. *Space Sci Rev.*, 2018, 214:89.
11. Gavrik AL, Gavrik YuA, Kopnina TF, Kuleshov EA. Oscillations near the lower boundary of the Venus ionosphere using radio occultation data from Venus-15,-16 satellites. *Radioengineering and electronics*, 2013, 58 (10):1013-1024.
12. Gavrik AL, Samoznaev LN. Analysis of the errors of the results of the radio sounding of the daytime Venus ionosphere due to its nonsphericity. *Space research*, 1985, 23 (1):148-15.
13. Withers P. Prediction of atmospheric properties measured by radio occultation experiments. *Advances in Space Research*, 2010, 46:58-73.
14. Gavrik AL, Bondarenko MI, Smyslov AA, Kopnina TF. Method of diagnostics of layered structures in the atmosphere and ionosphere according to radio sounding data. *Journal of Radioelectronics [online journal]*. 2017, 11:7; <http://jre.cplire.ru/jre/nov17/9/text.pdf>.
15. Yakovlev OI. *The propagation of radio waves in space*. Moscow, Nauka Publ., 1985, 214 p.

# SPATIAL-TEMPORAL CONDITIONS OF THE MOON BISTATIC SOUNDING

Olga V. Yushkova, Vyacheslav V. Yushkov, Roman A. Rudamenko, Taisiya N. Dymova

Kotelnikov Institute of Radioengineering and Electronics of RAS, Fryazino Branch, <http://fire.relarn.ru>  
Fryazino 141190, Moscow Region, Russian Federation

[o.v.y@mail.ru](mailto:o.v.y@mail.ru), [iushkov@physics.msu.ru](mailto:iushkov@physics.msu.ru), [crasher22@yandex.ru](mailto:crasher22@yandex.ru), [tasinidze@gmail.com](mailto:tasinidze@gmail.com)

*Abstract.* In a framework of the Russian project “Luna-Resurs”, the study of the lunar soil using bistatic radio sounding involving the Irkutsk Incoherent Scatter Radar is envisaged. Measurements are planned in the “up link” mode. According to the Fresnel approximation, the region of greatest reflection is defined as a region on the surface whose center is determined from the condition of equality of angles between the normal to the surface and directions from the base of the normal to the receiver and transmitter. The linear dimensions of the reflection region are associated with the Fresnel zones. Measurements are considered optimal if the region of greatest reflection falls within the visibility range of the orbital radar. The distance from the spacecraft to the center of the radio reflection region depends on the ballistic coordinates of the spacecraft, sometimes it equals to 500 kilometers or more, which must be taken into account when experiments are planned. The article presents the derivation of the formula, which determines the optimal time of reception of the reflected signal by the orbital radar for the bistatic location of the Moon in the “up link” mode.

*Keywords:* bistatic radar, coordinates, reflected spot, the Moon, spacecraft

UDC 523.34-83

*Bibliography* - 6 references

*Received* 13.03.2019, *accepted* 29.03.2019

RENSIT, 2019, 11(1):13-20

DOI: 10.17725/rensit.2019.11.013

## CONTENTS

1. INTRODUCTION (13)
  2. TECHNICAL PARAMETERS OF GROUND AND ORBITAL RADARS (14)
  3. SCHEME OF BISTATIC REMOTE SENSING OF THE MOON IN “UP LINK” MODE (15)
  4. LOCATION OF THE VISIBILITY ZONE OF THE ORBITAL RADAR AND THE REFLECTING SPOT OF RADIOSIGNAL (17)
  5. TIME OF REGISTRATING OF REFLECTED SIGNAL WITH ORBITAL RADAR (18)
  6. CONCLUSION (18)
- REFERENCES (19)

## 1. INTRODUCTION

The main aim of the Russian mission “Luna-Resource” is to study the structure and mineralogical composition of the upper cover of the Moon. Radiolocation is one of the remote methods that allow

achieving the goal. To study the Moon surface with radiophysical methods, the radar complex RLK-L will be installed on board the Luna-26 orbiter, the launch of which is planned for 2023 [1]. The device operation is provided both in monostatic and in bistatic mode in conjunction with the Irkutsk Incoherent Scatter Radar (IRNR) of the Institute of Solar-Terrestrial Physics of the Siberian Branch of Russian Academy of Sciences[2].

Bistatic sounding of the Lunar soil were carried out from the spacecraft “Luna 10, 11, 12, 14, 19, 22”, “Lunar orbiter 1”, “Explorer 35”, “Apollo 14,15,16”, “Clementine”, the radio signals were generated by the transmitters of the service radio complexes of satellites, and the echo was transmitted out on Earth. This location

of receiving and transmitting equipment for Lunar probing was called “down link”, unlike the “up link” scheme tested in 2006, when the radio complex of the Arecibo observatory was used as a transmitter, and radio signals were received on the "Lunar Reconnaissance Orbiter spacecraft (LRO)". Since the resolution of radar depends on the transmitter's energy potential, generation on Earth makes it possible to use a high-power radio signal for sensing, which is not limited to energy consumption norms and electromagnetic compatibility requirements with sensitive scientific and service devices. Thus, the peak power of the Arecibo chirp signal with a center frequency of 2379.2 MHz with a deviation of 1.6 MHz corresponded to 200 kW. In the bistatic location of the moon, planned for under the Luna Resource mission, the IRNR will generate a chirp signal in the frequency range from 154 to 162 MHz with a peak power of 3.2 MW, and its reflection from the Moon will be recorded by the RLK-L device.

There are techniques that allow determining the properties of the soil layer in the region of the reflection of radio waves based on a comparison of the characteristics of the emitted and received signals [3]. The main problem of the moon's bistatic radar experiments is the difficulty of defining the zone that forms the reflected radio signal, its distance from the point under the spacecraft and, as a result, in the absence of the possibility of parallel recording of the reflective surface of video and photo equipment. One of the particular problems of this problem is the choice of the optimal reception time by the orbital radar of the reflected signal: a signal too short in time may not contain useful information, and an unnecessarily

long one requires allocating too much onboard processor memory and additional time resources when broadcasting scientific information to Earth. This article discusses issues related to determining the optimal time of reception of the reflected signal by the orbital radar, which depends on its location over the Moon, that is, on the coordinates of the spacecraft. Ballistic parameters of a spacecraft – its height  $H_s$ , longitude  $\varphi_s$  and latitude  $\theta_s$  are determined by the Flight Control Center and are provided for processing the measurement results in the selenographic coordinate system.

## 2. TECHNICAL PARAMETERS OF GROUND AND ORBITAL RADARS

Irkutsk incoherent scatter radar is under the jurisdiction of the Institute of Solar-Terrestrial Physics of the SB RAS. It is a monostatic, pulsed radar with frequency scanning in the North-South direction in the sector  $\pm 30^\circ$  by changing the carrier frequency in the range 154-162 MHz. The peak power of the generated radio signal reaches 3.2 MW, the repetition frequency of the probe pulses is 25 Hz. The duration of the probe pulse is from 70 to 900  $\mu\text{s}$ , the antenna gain is about 35 dB.

The radio complex RLK-L, installed on the spacecraft "Luna-26", consists of two radar – radar-20 and radar-200. The device is designed to study the top layer of soil in the mode of monostatic location. Initially, the frequency range from 17.5 to 22.5 MHz was selected for the Radar-20, and from 175 to 225 MHz for the Radar-200. Then it was decided to add the monostatic regime of the moon's radar with bistatic measurements. Since it is planned to use IRNR as a transmitter, to ensure joint

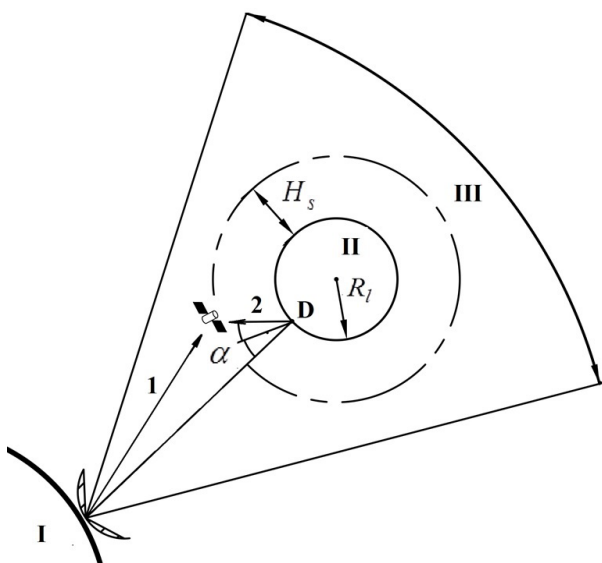
operation with ground equipment, the frequency range of the Radar-200 is reduced to 140-180 MHz.

**3. SCHEME OF BISTATIC REMOTE SENSING OF THE MOON IN “UP LINK” MODE**

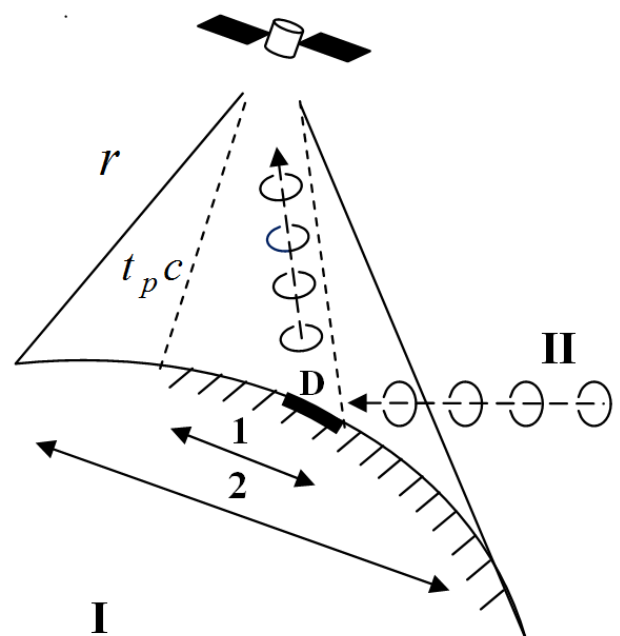
Bistatic measurements are carried out while the Moon and the spacecraft are in the scanning sector of the ground-based radar. **Fig. 1** shows the location of the receiver and transmitter during the bistatic measurements of the Moon according to the “up link” mode: the number I indicate Earth, the number II indicates the Moon, and the III indicates the scanning sector of the ground-based radar. In the same figure, the number 1 indicates the path of the “direct” signal propagating from the ground-based radar to the spacecraft; and 2 – the path of the “reflected” signal, which passes the distance from the Earth to the Moon and, reflecting from the Moon, to the spacecraft. The center of the reflection region is found from the condition that the angles between the normal to the surface of the Moon and the direction to the Earth and between the same normal and the direction to the spacecraft are equal (Fresnel law). In

Fig. 1, this angle is marked  $\alpha$ , and the center of the reflection region is indicated by point *D*.

The reflection of radio waves from an inhomogeneous surface is usually considered as the sum of two components: diffuse scattering and quasi-specular reflection. When ground-based radar is in operation, the entire surface of the Moon visible from Earth is a region of diffuse scattering. **Fig. 2** shows a diagram of the formation of the reflected signal: the signal propagates to the Moon (in the figure it is indicated by the number I) from the Earth (the number is II). The shaded area in the diagram corresponds to the part of the surface involved in the formation of diffuse scattering. The quasi-mirror reflection of radio waves in the remote sensing approximation of radiophysics is modeled by a ray tube whose diameter is associated with two or three Fresnel zones [4]. In Fig. 2, this component is shown in gray. The ray tube limits the most essential



**Fig. 1.** Scheme of the Moon bistatic radar sounding.



**Fig. 2.** Radio signal reflection in bistatic radar sounding experiments.

region for reflection on the surface, in Fig. 2 this surface area is painted black, its center is marked with the letter  $D$ . Orbital radar can receive a signal reflected from the ground from the territory of diffuse scattering and the area bounded by the ray tube. The time of the work of RLC-L  $t_p$  will be considered optimal if it received of all quasi-mirror component of the ground-based radar radio signal, but its diffuse component is recorded as little as possible.

For solving the problems of bistatic radar sounding using the orthogonal system of selenographic coordinates (SC) MOON ME. The Moon is approximated by a sphere with a radius  $R_l = 1737.4$  km in this system:

$$x^2 + y^2 + z^2 = R_l^2. \quad (1)$$

The center of the sphere (1) coincides with the center of mass of the Moon and with the center of the coordinate system MOON ME. Axes  $OX$  and  $OY$  lie in the plane of the lunar equator, while the first is directed to the initial meridian, i.e. to the ground. During the experiment, the directions to the Earth and to the ground-based radar coincide. The second axis faces east, toward Mare Crisium. The axis  $OZ$  is located along the average position of the axis of rotation of the body and is directed to the North Pole. A spherical system of selenographic coordinates is associated with a three-dimensional orthogonal system, in which the longitude is measured from the zero meridian. The meridians can be numbered in two ways - from  $0^\circ$  to  $360^\circ$  east (as when processing the results of NASA lunar missions), or from  $0^\circ$  to  $+180^\circ$  east and up to  $-180^\circ$  west. We will use the second method of counting longitude to preserve the analogy with the earthly

mapping technology. Longitude  $\varphi$  is defined as the dihedral angle between the plane of the prime meridian and the plane of the meridian passing through the observation point. Selenographic latitude  $\theta$  is the length of the arc along the meridian and is measured from the equator (to the north with a plus sign, to the south with a minus sign). The coordinates of the spacecraft in the rectangular and spherical systems are related by the formulas:

$$\begin{pmatrix} x_s \\ y_s \\ z_s \end{pmatrix} = \begin{pmatrix} (R_l + H_s) \cos \theta_s \cos \varphi_s \\ (R_l + H_s) \cos \theta_s \sin \varphi_s \\ (R_l + H_s) \sin \theta_s \end{pmatrix}.$$

For solving posed problem, it suffices to consider the plane passing through the spacecraft, the Moon center and the ground-based radar with coordinates  $(L - R_e; 0; 0)$ . Here  $L$  is the distance between the Earth center and the Moon one. Denote the plane  $\beta$  and find its equation:

$$\begin{vmatrix} x & y & z \\ L - R_e & 0 & 0 \\ x_s & y_s & z_s \end{vmatrix} = 0.$$

After the transformation, the equation of the plane  $\beta$  will be  $y = z \frac{y_s}{z_s}$  or  $y = \chi \operatorname{ctg} \theta_s \sin \varphi_s$ . It means, that it passes through the axis  $OX$  and is tilted to the equatorial plane at an angle  $\psi$ , whose tangent is  $\operatorname{tg} \psi = \operatorname{tg} \theta_s / \sin \varphi_s$ .

In the plane  $\beta$  we construct a rectangular SC as follows: the axis  $OX$  of this system coincides with the axis  $OX$  of the original MOON ME system, and the axis  $OZ^*$  perpendicular to it is connected to the  $OZ$  axis of the MOON ME system as follows:

$$z = z^* \sin \psi = z^* \frac{\sin \theta_s}{\sqrt{\sin^2 \theta_s + \cos^2 \theta_s \sin^2 \varphi_s}}. \quad (2)$$

With rectangular SC  $XOZ^*$  plane  $\beta$  is connected polar SC. In this SC the spacecraft position is uniquely determined

by two parameters: a segment OK, whose length is equal to  $R_l + H_s$ , and an angle  $\eta$ . The geometrical location of the spacecraft is denoted by a point K on Fig. 3. The angle  $\eta$  can be determined from the triangle OEK in the MOON ME with the coordinates of points O,  $E(R_l + H_s; 0; 0)$ , where E is the point of intersection of the zero meridian with the equator, and K. As result we have formula:  $\cos\eta = \cos\theta_s \cos\varphi_s$ . The maximum value at  $\eta$  for altitude in 50 km is  $103^\circ$ , for 100 km –  $110^\circ$ .

**4. LOCATION OF THE VISIBILITY ZONE OF THE ORBITAL RADAR AND THE REFLECTING SPOT OF RADIOSIGNAL**

The “radar visibility zone” is a part of the surface bounded by the line of intersection of the sphere (1) and the cone, whose axis coincides with the straight line OK in Fig. 3, and the generator KF is equal to the distance from the spacecraft to the most distant points of the lunar surface, from which it is still possible take the reflected signal. If the time of reception of the reflected signal is large, then the value is equal to the length of the tangent from the point K to the circle (Fig. 3); so  $r = \sqrt{2R_l^2 + 2R_lH_s + H_s^2}$ . The value  $r$  depends only on the height of the

apparatus (on Fig. 2 this line corresponds to the solid straight line marked  $r$ ). If the registration time is limited as  $t_p < r/c$ , where  $c$  is the speed of light, then the linear dimensions of the visibility zone decrease: the distance to the most distant points of the surface becomes equal  $t_p c$ . In Fig.2, the straight line of such a cone, which limits the zone of visibility, is shown by a dashed straight line. The length of the arc along the surface of the Moon in the radar visibility zone is equal to  $2L$ , where

$$L = R_l \arccos\left(\frac{(R_l + H_s)^2 + R_l^2 - t_p^2 c^2}{2(R_l + H_s)R_l}\right).$$

Next, we discuss how to highlight the area of reflection of the radio signal. The coordinates of point D, according to [5], are determined on the basis of the conditions of geometrical optics. It is believed that the radio signal from the IRNR propagates along the straight line AD, parallel to the axis OX to point D on the surface of the Moon, and after reflection from the surface along the line DK (Fig. 3). Point D is such that the angle ADN is equal to the angle NDK. Due to the parallelism of the AD and OX, the angles of XOD, ADN and NDK are equal, we denote angles as  $\alpha$ . Maximum value of the angle  $\alpha$  is  $90^\circ$ .

If the angle  $\alpha$  associated with the ballistic coordinates of the spacecraft was known, then in the SC  $XOZ^*$  the coordinates of point D were determined by the relations:

$$\begin{aligned} x_D &= R_l \cos\alpha \\ \text{and} \\ z_D^* &= R_l \sin\alpha. \end{aligned} \tag{3}$$

In order to find  $\alpha$ , we consider the triangle KOD on Fig. 3. From the known theorem follows formula:

$$\frac{OK}{\sin \angle NDK} = \frac{OD}{\sin \angle OKD}.$$

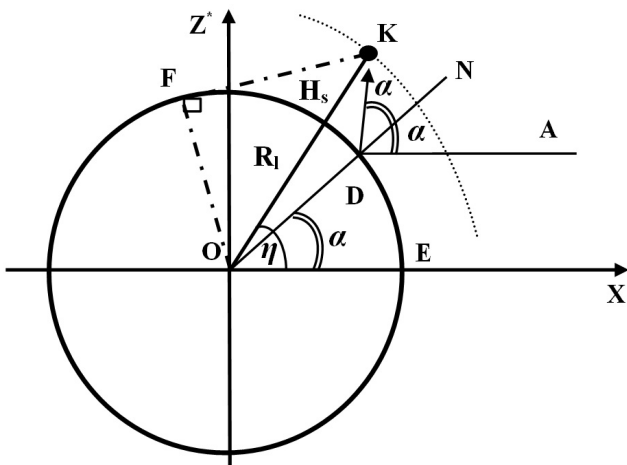


Fig. 3. Rectangular coordinate system of plane  $\beta$ .

From  $\angle OKD = 180^\circ - \angle KOD - \angle ODK$ , follows  $\sin \angle OKD = 2\alpha - \eta$ . Thus, the angles  $\alpha$  and  $\eta$  connected expression:

$$(R_r + H_r)\sin(2\alpha - \eta) = R_r \sin \alpha. \quad (4)$$

From equation (4) the value  $\alpha$  is found numerically. Equation (4) has several roots, but the physical formulation of the problem is satisfied by the angle located between  $0^\circ$  and  $\eta$ .

According to the found value of the angle  $\alpha$ , the coordinates of point  $D$  are determined by expressions (3) in SC  $XOZ^*$ , and in SC MOON ME according to (2) the coordinates of point  $D$  will look like:

$$x_D = R_r \cos \alpha$$

and

$$y_D = \frac{R_r \sin \alpha \cos \theta \sin \varphi}{\sqrt{\sin^2 \theta + \cos^2 \theta \sin^2 \varphi}}. \quad (5)$$

The third coordinate of point  $D$  is determined either from equation (1) or from the digital 3D model of the lunar surface, if it is used to analyze the problem.

According to [4], the reflecting spot is an elliptic region; size of the elliptic section is evaluated with the approximate relations:

$$\Delta y \approx k(s\lambda)^{1/2} \cos^{-1} \eta, \quad \Delta x \approx k(s\lambda)^{1/2}. \quad (6)$$

Here  $\Delta y$  is the linear dimension of the section along the tangent to point  $D$  in the plane  $\beta$ , and  $\Delta x$  - one in the perpendicular direction,  $\lambda$  is the wavelength for the monochrome signal. Since the IRNR signal is chirp, for the calculations is used 154 MHz. The coefficient  $k$  specifies the number of Fresnel zones taken into account for estimate the reflection zone. It is usually considered to be 3-4 [4], but in practice and in mathematical modeling this value is taken much more [6]. Formula (6) includes a parameter  $s$  that is equal to the distance from the spacecraft to the center of the reflection site. Its value,

taking into account (5), is determined by the formula

$$s = \sqrt{(x_s - x_D)^2 + (y_s - y_D)^2 + (z_s - z_D)^2}.$$

## 5. TIME OF REGISTRATING OF REFLECTED SIGNAL WITH ORBITAL RADAR

Next, we consider what conditions the radar operating time should satisfy, so that the region most main for reflection gets into the visibility range of the device.

Point  $D$  is the midpoint of the segments  $\Delta y$  and  $\Delta x$ . Due to the fact that  $\Delta y \ll R_r$ , the length of the arc of a circle in the plane  $\beta$ , the ends of which connects this segment, is also equal to  $\Delta x$ . In this case, the length arch from point under spacecraft to the point farthest from the spacecraft, but still included in the region of the maximum of reflection is equal to the total length of arc corresponding to an angle  $\eta - \alpha$  (Fig. 3) and an arc  $\Delta y/2$  corresponding to an angle  $\Delta y/2R_r$ .

Thus, the distance between the spacecraft and this point is equal to  $R = \sqrt{(R_r + H_r)^2 + (R_r)^2 - 2(R_r + H_r)R_r \cos(\eta - \alpha + k(s\lambda)^{1/2} / 2R_r \cos \eta)}$ . And, therefore, the time of the radar is calculated by the formula:  $t_p = c^{-1}R$ .

## 6. CONCLUSION

In the framework of the Russian project "Luna-Resource", the study of the soil of the Moon by the radar complex RLK-L using the bistatic radio sounding method involving the Irkutsk incoherent radar is envisaged. Measurements are planned in the "up link" mode. Based on the Fresnel approximation, the region of greatest reflection is defined as a portion of the surface whose center is found from the condition of equality of angles between the normal to the surface and the directions from the base of the

## RADIOLOCATION

normal to the receiver and transmitter. The linear dimensions of the reflection area are associated with two to three Fresnel zones. Measurements are considered optimal if the area of greatest reflection is within the visibility range of the orbital radar. The distance from the spacecraft to the center of the radio reflection region depends on the ballistic coordinates of the spacecraft, and sometimes is 500 kilometers or more, which must be taken into account when planning experiments in determining the time of orbital radar operation and allocating the necessary memory for recording the reflected radio signal. The article presents the derivation of a formula for determining the optimal reception time depending on the location of the spacecraft. A preliminary analysis of the results of numerical simulation of the bistatic radar sounding of the Moon showed that the optimal registration time of the reflected signal depends on the height of the spacecraft and the angle  $\eta$ , the value of which is related to the longitude and latitude of the spacecraft by the formula  $\eta = \arccos(\cos\theta_s \cos\varphi_s)$ . If the angle  $\eta$  is greater  $60^\circ$ , only part of the first Fresnel zone involved into the visibility range of the orbital radar. The registration time of the reflected signal in this case is the longest and amounts to  $1 \mu\text{s}$  with a vehicle height of 100 km.

If the angle  $\eta$  belongs to the interval from  $8^\circ$  to  $65^\circ$ , the time for receiving the signal and, consequently, the amount of memory required to store it is 3-4 times less, and up to 10 Fresnel zones involved into the radar view. The location of the spacecraft in this zone is optimal for carrying out natural measurements.

### ACKNOWLEDGMENT

*The work was carried out with partial support of the Basic Research Program No. 12 of the Presidium of the Russian Academy of Sciences "Problems of the Genesis and Evolution of the Universe with the methods of ground-based observations and space research".*

### REFERENCES

1. Smirnov VM, Yushkova OV, Marchuk VN, Abramov VV, Kvulinskiy YE, Lyahov YN. Luna-Glob Project: Radio Sounding of the Lunar Soil. *Journal of Communications Technology and Electronics*, 2013, 58(9):911-918.
2. Yushkova OV, Gavrik AL, Marchuk VN, Yushkov VV, Smirnov VM, Laptev MA, Chernyshev BV, Dutyshev IN, Lebedev VP, Medvedev AV, Petrukovich AA. Bistatic Radar Detection in the Luna-Resurs Mission. *Solar System Research*, 2018, 52(4):287-300.
3. Yushkova OV, Yakovlev OI. Analysis of the possibilities to determine lunar soil characteristics with the help of bistatic radar. *Journal of Communications Technology and Electronics*, 2017, 62(1):22-30.
4. Feinberg EL. *Rasprostranenie radiovoln vdol zemnoy poverkhnosti* [Propagation of radio waves along the earth's surface]. Moscow, USSR Academy of Sciences Publ., 1961, 496 p.
5. Yushkova OV, Rudamenko RA, Yushkov VV Localization of the reflection area in the moon's bistatic sounding. *Journal of Radio Electronics*, 2018, № 11. Available at <http://jre.cplire.ru/jre/jul18/2/text.pdf>, DOI 10.30898/1684-1719.2018.7.2 (in Russ.).

6. Smirnov VM, Yushkova OV, Karachevtseva IP, Nadezhdina IE. The influence of relief on formation of reflected signals of subsurface sounding radar. *Solar System Research*, 2014, 48(3):176-181.

# BACKSCATTERING FROM THE NEAR-SURFACE LAYER OF THAWED/FROZEN SOILS OF ALASKA FROM SENTINEL 1 RADAR DATA

Natali V. Rodionova

Kotelnikov Institute of Radioengineering and Electronics of RAS, Fryazino Branch, <http://fire.relarn.ru>

Fryazino 141190, Moscow Region, Russian Federation

[rnv@ire.rssi.ru](mailto:rnv@ire.rssi.ru)

*Abstract.* This paper considers the question of determining frozen/unfrozen status of 5 cm topsoil layer for seven ground stations in Alaska with latitude from 65° to 70° N by using radar Sentinel 1 C-band data for the period 2016-2017. Determine the status of frozen soil was carried out by two ways: using only radar data with finding the backscatter coefficient threshold, when the temperature in the upper soil layer falls below 0°C, and by using both radar data and ground-based measurements of soil temperature. In the latter case, the correlation between the backscattering coefficient and the soil temperature measured at 5 cm below the soil surface was calculated. Regression models were developed and radar backscatter thresholds for frozen soil were found. Local frozen/unfrozen soil maps were created. The comparison of threshold values obtained by two ways showed their closeness, which tends to decrease with decreasing correlation between radar and ground data. Linear regression between radar backscatter threshold and the area latitude have been received.

*Keywords:* C-band radar data, soil temperature, frozen/unfrozen soil, backscattering coefficient, Spearman's correlation coefficient

UDC 528.854, 528.88

*Bibliography* – 12 references

*Received* 13.03.2019, *attached* 29.03.2019

*RENSIT*, 2019, 11(1):21-30

**DOI: 10.17725/rensit.2019.11.021**

## CONTENTS

1. INTRODUCTION (21)
  2. GROUND DATA (22)
  3. THE INPUT S1 RADAR DATA (23)
  4. DETERMINATION OF FROZEN/THAWED SOIL STATE FROM S1 RADAR DATA (24)
  5. DETERMINATION OF THE STATE OF FROZEN SOIL BY CORRELATION BETWEEN RADAR AND GROUND DATA (27)
  6. CONCLUSION (28)
- REFERENCES (29)

## 1. INTRODUCTION

Remote sensing offers promising methods for monitoring the near-surface state of frozen/thawed soils on a wide geographical scale [1,

2]. The use of radiometers is limited to very large areas due to the low spatial resolution. Unlike IR and microwave radiometers, SAR systems can provide information at high spatial resolution about the dynamic state of the soil regardless of the cloud and the day time. The radar signal is mainly dependent on the soil dielectric permittivity (DP), which is directly related to the water and ice content, and on surface roughness and vegetation cover.

Active sensors distinguish frozen soil (FS) by changing the content of liquid water in the soil. These changes are associated with the values of the DP of soil [3]. The average

value of dry soil DP is about 2-3, while liquid water 80. DP soil grows in proportion to the volume content of liquid water in it. In critical winter conditions, most of the water in the soil freezes, which leads to a significant decrease in the average value of the soil DP. Frozen water has an ice value of 3.2 DP, which is similar to dry soil DP [4]. The reverse process occurs in the spring, when the ice in the soil melts, which leads to an increase in the backscattering coefficient by several decibels [5].

Soil properties (structure, texture, drainage) affect the water content in the soil and on the dynamics of its freezing process. Mineralized soils freeze faster and to a greater depth than organic soils due to their less ability to store water [5]. The same situation exists between sandy and clay soils.

The object of the study was FS in 7 ground stations in Alaska with the latitude of the place from 65° N to 70° N, where soil parameters are in free access by International soil moisture network (ISMN) [6].

Radar Sentinel 1 (S1) C-band IW (interferometric wide swath) mode, VV+VH polarizations, 20 m spatial resolution data for the period 2016-2017 were used in this investigation.

The aim of the work is the distinction between thawed/frozen soils in the upper

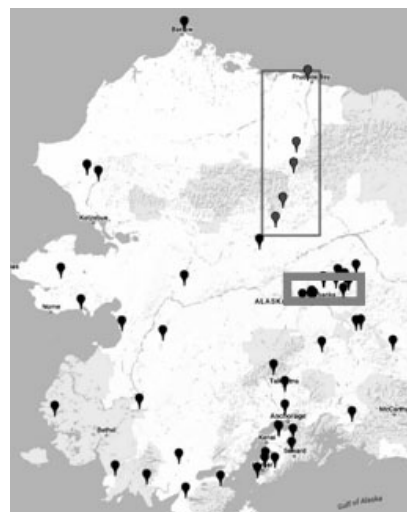


**Fig. 1.** The location of the considered ground stations in Alaska.

5-cm layer, to find the connection radar backscatter coefficient and the temperature of the upper soil layer; and also to build local maps of frozen/thawed soils using only radar data or radar data together with ground information.

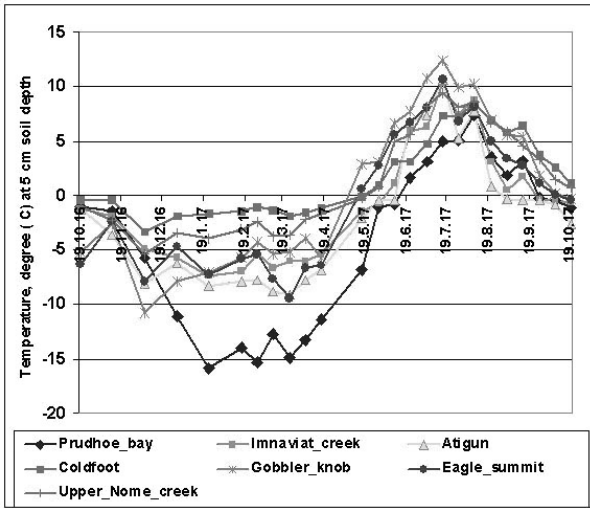
## 2. GROUND DATA

The work used ground measurements of soil parameters (temperature and humidity at depths of 5, 20 and 51 cm) and air temperature, which are free available in website of the International soil moisture network (<https://ismn.geo.tuwien.ac.at/>). Seven stations in Alaska were selected for which the time period of ground-based measurements coincided with available Sentinel 1 radar information. The location of

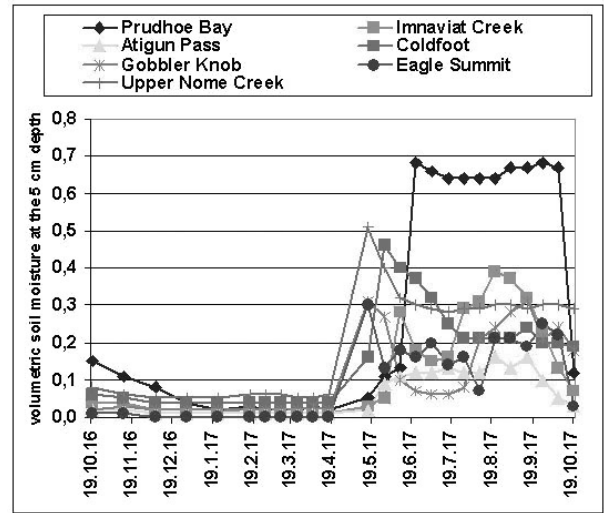
*Table 1.*

Information about Alaska ground stations (according to ISMN)

Station name	Latitude, N deg	Longitude, W deg.	Soil texture on the depth 0-30 cm, %
Prudhoe Bay	70.27	-148.57	silt – 48, sand-34, clay- 18
Imnaviat Creek	68.62	-149.3	sand-73, silt – 18, clay- 9
Atigun Pass	68.13	-149.48	sand-73, silt – 18, clay- 9
Coldfoot	67.25	-150.18	silt – 48, sand-34, clay- 18
Gobblers Knob	66.75	-150.67	sand-40, silt – 39, clay- 21
Eagle Summit	65.49	-145.61	sand-40, silt – 39, clay- 21
Upper Nome Creek	65.37	-146.59	sand-40, silt – 39, clay- 21



(a)



(b)

**Fig. 2.** Graphs of ground measurements of temperature (a) and volumetric soil moisture at a depth of 5 cm (b) in Alaska stations for the period 19.10.16-20.10.17 by ISMN data.

the stations is shown in **Fig. 1**. They are from north to south: Prudhoe Bay, Imnaviat Creek, Atigun Pass, Coldfoot, Gobblers Knob (the five stations marked by top rectangle), Eagle Summit and Upper Nome Creek (stations highlighted in bottom rectangle).

Information about Alaska ground stations is given in **Table 1**.

The graphs of ground-based measurements of temperature (a) and volumetric soil moisture at a depth of 5 cm (b) for stations in Alaska for the period 19.10.16 - 20.10.17 are shown in **Fig. 2**. Both values (soil temperature and humidity) are taken from the ISMN ground measurement database at the time of the site survey by Sentinel 1 radar. It should be noted that for winter time information about soil moisture is not reliable [6].

It follows from Fig. 2 that the lowest soil temperatures at a depth of 5 cm are for the Prudhoe Bay station- the northernmost of the stations under consideration. The highest temperatures in winter are for Coldfoot and Upper Name Creek stations. In the latter case, this is expected, since Upper Nome Creek

is the southernmost of the stations under consideration. For Coldfoot, this is probably due to the height of the snow cover. But, as shown by the graph in **Fig. 3**, the snow depth for these two stations is almost the same.

### 3. THE INPUT S1 RADAR DATA

In this work, we used Sentinel 1 C-band radar data IW (interferometric wide swath) mode with two polarizations (VV+VH) and a spatial resolution of 10 m. The S1 images were processed by a program S1Toolbox and later SNAP [7]. Pre-processing of the data

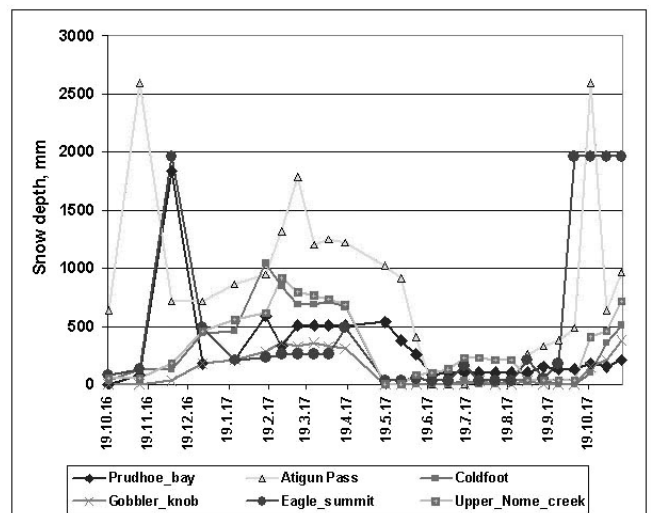


**Fig. 3.** Snow depth in mm for Alaska ground stations (ISMN data).

Table 2

Information on S1 radar data used

Station name	Number of S1 processed images	View angle	Radar survey time period used	Number points in profile
Prudhoe Bay	28	33°	19.10.16 – 25.11.17	~10
Imnaviat Creek	28	41°	21.10.16 – 27.11.17	~10
Atigun Pass	25	37°	31.10.16 – 7.11.17	~10
Coldfoot	24	42°	14.11.16 – 27.11.17	~10
Gobblers Knob	23	43°	14.11.16 – 27.11.17	~10
Eagle Summit	28	40°	23.10.16 – 29.11.17	~15
Upper Nome Creek	28	40°	23.10.16 – 29.11.17	~15

included selection of the fragment with the study area and radiometric calibration.

**Table 2** shows the data for each station by the number of processed survey sessions, viewing angle, time period of survey and the number of points in profile.

#### 4. DETERMINATION OF FROZEN/ THAWED SOIL STATE FROM S1 RADAR DATA

The depth of penetration of the e/m wave into the soil is determined by the equation  $\delta p = \lambda \sqrt{\varepsilon'} / (2\pi\varepsilon'')$ , where  $\lambda$  – the wavelength,  $\varepsilon = \varepsilon' + i\varepsilon''$  – the dielectric permeability of the soil. For S1 the wavelength is 5.4 cm. In the case of frozen soil with  $\varepsilon' \approx 5.5$  and  $0.1 \leq \varepsilon'' \leq 0.5$  we get a penetration depth  $4 \leq \delta p \leq 20$  cm.

The method of identification of thawed/frozen soil state is based on a 3-5 dB drop in during the transition to the state [1, 2].

Using the time series S1, we determine the date of the beginning of freezing/thawing of the soil by strong differences of  $\sigma^0$  and further stable low/high values of  $\sigma^0$ . **Fig. 4** shows graphs of the difference in the absolute value of  $\sigma^0$  VV polarization in dB for neighboring radar imagery dates. Two peaks allow to determine the date of beginning soil to freeze and thaw. For the Prudhoe Bay station, the first maximum

is 2.69 dB. This is  $\text{abs}(-11.53 + 14.22)$  [dB] =  $\text{abs}(\sigma_{29.5.2017}^0 - \sigma_{17.5.2017}^0)$  [dB] – these are the dates to begin soil thawing. The second maximum determines the date of beginning soil to freeze. Maximum equals 1.69 dB. This is  $\text{abs}(-16.36 + 14.67)$  [dB] =  $\text{abs}(\sigma_{20.10.2017}^0 - \sigma_{8.10.2017}^0)$  [dB] is the freezing of soil at a 5 cm layer. For Coldfoot ground station, the difference in soil freezing values is about 3.9 dB =  $\text{abs}(\sigma_{10.10.2017}^0 - \sigma_{28.09.2017}^0)$ . When determining the date of thawing of the soil there are difficulties with finding the appropriate maximum. It should be noted that the difficulty to determine maxima increases when the latitude is shifted to the South.

Another way to determine the state of FS only from radar data without using ground measurements is shown in the paper [8]. These authors, similar to [9], characterize the soil cover state by the surface state factor (SSF):

$$SSF = \frac{1}{2} + \frac{\sigma^0(t) - \sigma_{sum}^0}{\sigma_{sum}^0 - \sigma_{win}^0}, \quad (1)$$

where  $\sigma_{sum}^0$  and  $\sigma_{win}^0$  are the mean values of radar backscattering coefficient in summer and winter, respectively,  $\sigma^0(t)$  is the running value of radar backscattering coefficient, and  $t$  is time.

The authors [8] argue that the seasonal SSF variations are highly correlated with the

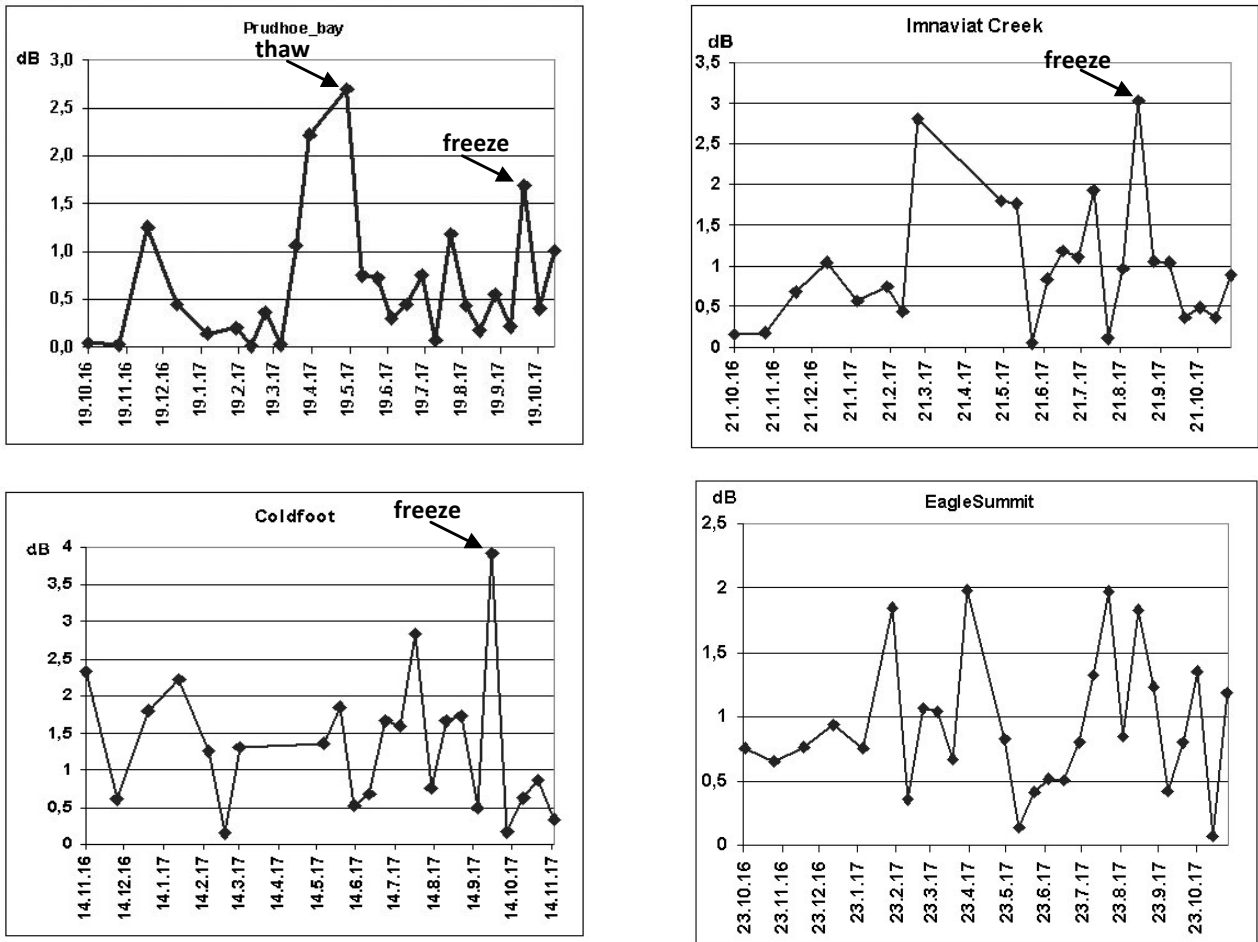


Fig. 4. Graphs of the difference between  $|\sigma^0|_{VV}$  polarization for the neighboring radar imagery dates.

seasonal variations of the soil temperature, taking negative values at soil temperatures below  $0^\circ\text{C}$ . Consequently, a 5-cm topsoil layer can be classified as frozen when the SSF, measured by radar, takes a negative value. SSF VV polarization graph for Prudhoe bay station is shown in Fig. 5.

The authors [8] noted a strong variability of SSF depending on the latitude. We use the data from table 3 for four stations Imnaviat Creek, Coldfoot, Eagle Summit, Upper Nome Creek to define a relationship  $\sigma_{thr}^0$  with

According to the equation (1) it turns out that the intersection of the value  $\text{SSF} = 0$  occurs for the same value, but for different times  $t$ , i.e. the value  $\sigma^0$  is the same for both the freezing point and the thawing point of the 5-cm topsoil layer. And this value can be determined for each place, knowing  $\sigma_{sum}^0$  and  $\sigma_{win}^0$ . Let's call this value  $\sigma^0$  as  $\sigma_{thr}^0$ . The  $\sigma_{thr}^0$  values calculated by the formula (1) for stations in Alaska under consideration are given in Table 3.

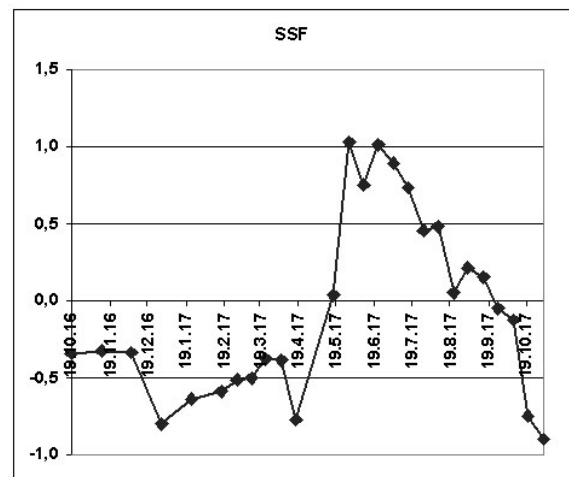


Fig. 5. SSF VV polarization for Prudhoe Bay.

Table 3.

$\sigma_{thr}^0$  values under SSF = 0.

Ground station	Prudhoe Bay	Imnaviat Creek	Atigun Pass	Coldfoot	Gobblers Knob	Eagle Summit	Upper Nome Creek
$\sigma_{thr}^0$ [dB]	-14.35	-17.56	-12.1	-14.6	-15.5	-11.66	-10.62

the latitude of the place. As a result, in Fig. 6 the obtained regression relation with the coefficient of determination 0.97 is shown, which connects the value  $\sigma_{thr}^0$  [dB] with the latitude of the place.

If the air temperature is known, the average summer and winter  $\sigma^0$  values can be determined using, for example, work [10], where the authors define winter and summer periods as follows: if the air temperature is less than the winter threshold (WT), equal to  $-3^\circ\text{C}$ , the corresponding date is considered as belonging to the winter period. Similarly, the threshold for summer at  $+3^\circ\text{C}$  is used to determine

the summer period. In both cases days with wet snow fall. So, for Prudhoe Bay, using ground-based measurements of air temperature by the ISMN, we receive, average  $\sigma^0$  for 22.6.17-14.9.17 and get  $\sigma_{sum}^0 = -12.96$  dB, and averaging the values of  $\sigma^0$  for the periods 19.10.16-17.5.17 and 20.10.17-25.11.17 received  $\sigma_{win}^0 = -15.68$  dB. The difference between these values and the values obtained without the use of air temperature data (using differences in  $|\sigma^0|$ ) is in the second decimal place.

Using  $\sigma_{thr}^0$  value, it is possible to construct the local maps of frozen/thawed soils. The local maps for Coldfoot station are shown in Fig. 7 for dates 28.09.2017 and 22.10.2017 (freezing) with  $\sigma_{thr}^0 = -14.16$  dB, and for dates 19/05/2017 and 12/06/2017 (thawing). The image size is  $4.2 \times 3.9$  km. Dark tone shows areas with frozen soil in 5-cm top layer. We note a significant increase in the area of freezing zones in the image for 22.10.2017 and a decrease in the area of frozen soil in the image for 12/06/2017 when thawing.

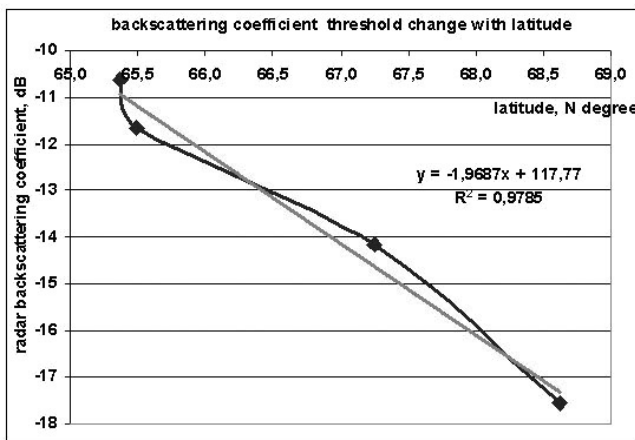


Fig. 6. The  $\sigma_{thr}^0$  change with latitude.

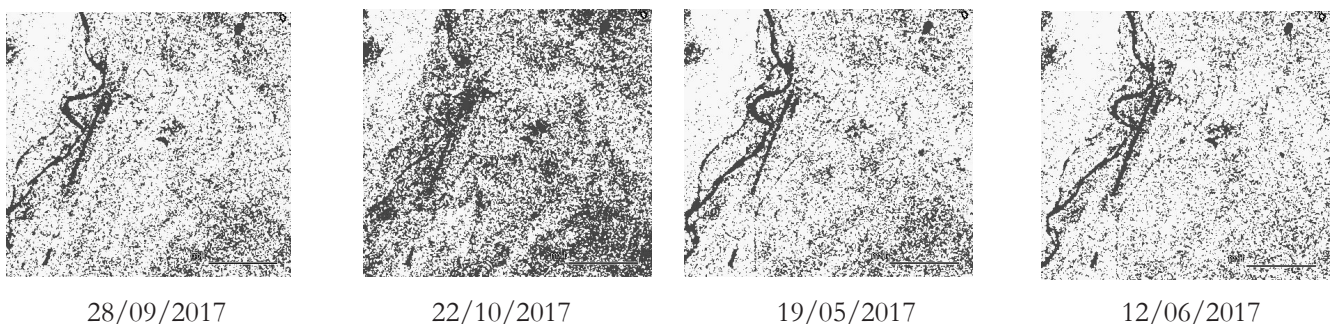


Fig. 7. Local maps of frozen (dark tone) and unfrozen soil at a 5 cm top layer for Coldfoot with  $\sigma_{thr}^0 = -14.16$  dB.

**5. DETERMINATION OF THE STATE OF FROZEN SOIL BY CORRELATION BETWEEN RADAR AND GROUND DATA**

For the first time, a strong correlation between  $\sigma^0$  and temperature of thawed/frozen soil in 5 cm top layer was experimentally established by [1, 2] for radar RADARSAT-1 measurements in C-band HH polarization. Simple linear regression showed a positive correlation between  $\sigma^0$  and soil temperature with different determination coefficients of (DC) depending on the mechanical soil composition. Regression models were obtained to find the threshold that was used to separate frozen and unfrozen soils. This  $\sigma_{thr}^0$  is the  $\sigma^0$  value at which the corresponding soil temperature is below 0°C. The authors used the empirically obtained temperature dependence of  $\sigma^0$  to construct a map of thawed and frozen soils on agricultural fields in the area of Quebec (Canada).

The authors of [11] showed the presence of a strong correlation between the co - polarization ratio (CR) of backscattered radar scattering cross sections on horizontal and vertical polarizations and the average temperature in the upper soil

layer with a thickness of 0.1 m. On the basis of this, the authors [11] proposed to remotely measure the average temperature in the upper soil layer by the measured CR values by ALOS PALSAR full polarimetry data.

In this work, to determine the correlation between  $\sigma^0$  and soil temperature at a 5 cm top layer, it was used S1 radar data C-band, VV polarization, and ground information from ISMN [6]. Linear regression model between  $T^\circ$  in 5 cm topsoil layer, and the  $\sigma^0$  can be used to predict  $T^\circ$  of soil and to construct maps of frozen soils using a threshold value  $\sigma_{thr}^0$ . The disadvantage here is that with a low coefficient of determination, the accuracy of determining the threshold will also be small.

**Table 4** shows the Spearman correlation coefficient between  $\sigma^0$  and ground measurements of soil temperature at a depths of 5, 20 and 51 cm, as well as air temperature (ISMN).

In **Fig. 8** the regression were shown for the stations with high correlation between  $\sigma^0$  and ground measurements of soil temperature at a depth of 5 cm: Prudhoe Bay, Imnaviat Creek, Upper Nome Creek and Coldfoot.

*Table 4.*

Spearman correlation coefficient between  $\sigma^0$  and ground measurements of air and soil temperature

	Prudhoe Bay	Eagle Summit	Upper Nome Creek	Imnaviat Creek	Atigun Pass	Coldfoot	Gobblers Knob
$T^\circ$ , air							
$\sigma_{vv}^0$	$\rho_s = 0.71, p=10^{-6}$	$\rho_s = 0.24, p=0.1$	$\rho_s = 0.64, p=10^{-4}$	$\rho_s = 0.8, p = 10^{-6}$	$\rho_s = -0.24, p=0.12$	$\rho_s = 0.58, p=10^{-3}$	$\rho_s = 0.44, p=0.02$
$T^\circ$ , soil 5 cm							
$\sigma_{vv}^0$	$\rho_s = 0.69, p=10^{-5}$	$\rho_s = 0.38, p=0.02$	$\rho_s = 0.78, p=0$	$\rho_s = 0.74, p=10^{-5}$	$\rho_s = 0.37, p=0.03$	$\rho_s = 0.65, p=10^{-4}$	$\rho_s = 0.49, p=0.01$
$T^\circ$ , soil 20 cm							
$\sigma_{vv}^0$	$\rho_s = 0.5, p=10^{-3}$	$\rho_s = 0.36, p=0.03$	$\rho_s = 0.78, p=0$	$\rho_s = 0.73, p = 10^{-5}$	$\rho_s = -0.35, p = 0.04$	$\rho_s = 0.56, p = 10^{-3}$	$\rho_s = 0.55, p = 0.003$
$T^\circ$ , soil 51 cm							
$\sigma_{vv}^0$	$\rho_s = 0.32, p=0.05$	$\rho_s = 0.26, p=0.08$	$\rho_s = 0.74, p=10^{-5}$	$\rho_s = 0.68, p = 10^{-4}$	$\rho_s = -0.38, p = 0.03$	$\rho_s = 0.3, p = 0.07$	$\rho_s = 0.54, p = 0.003$

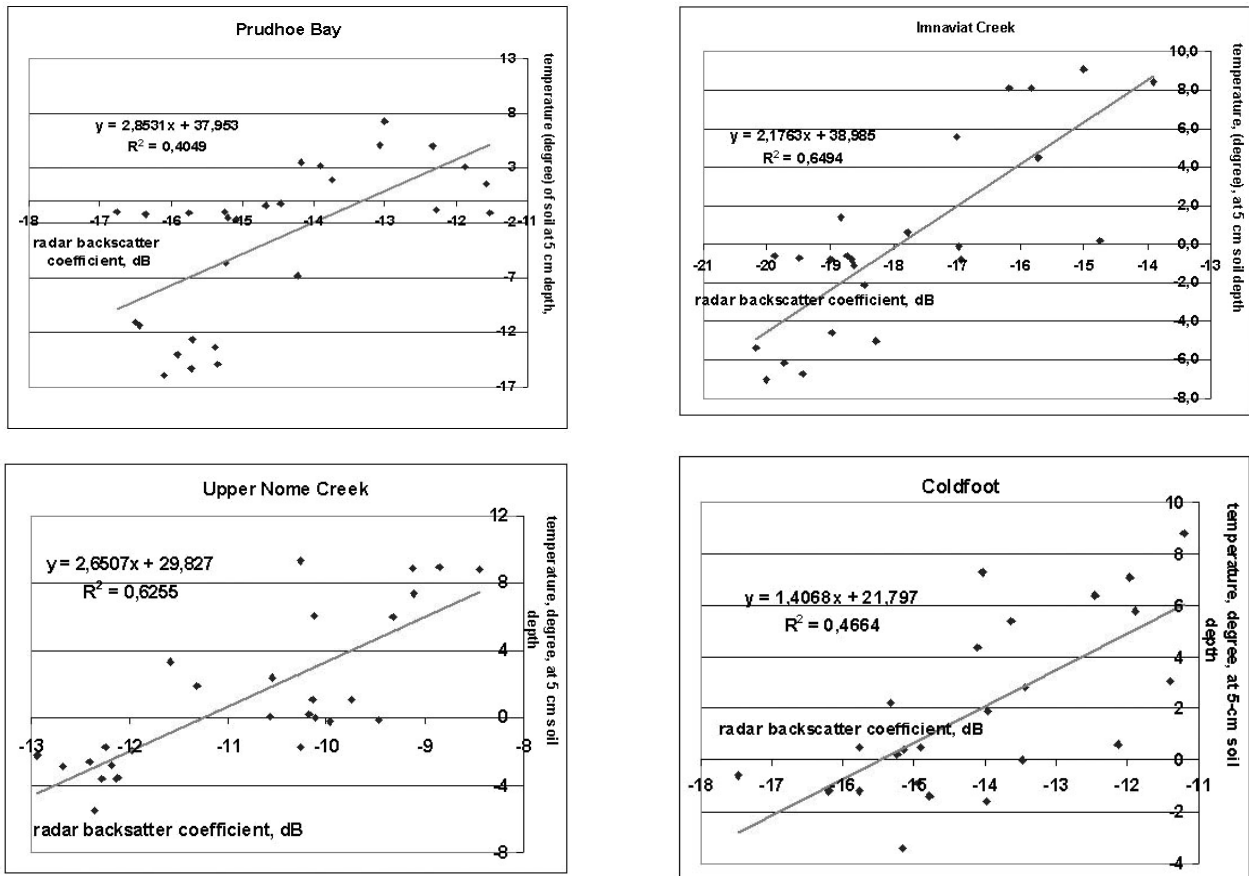


Fig. 8. Regression relations between  $\sigma^0$  (dB) VV polarization and soil temperature at a depth of 5 cm.

Let us compare the  $\sigma_{thr}^0$  values obtained from the regression (Table 5) with those obtained without the use of ground information (Table 3). The difference value is less than 1 dB with high correlation (Prudhoe Bay, Imnaviat Creek, Upper Nome Creek) and more than 1 dB, with an average correlation (Coldfoot).

It should be noted that the work [12] considered the correlation of S1 radar data with ground measurements of soil temperature for stations in Germany and France, where soil temperatures are only positive. And it is shown that the correlation varies from high to weak, and depends on the granulometric composition of the soil,

soil roughness. For frozen soils, this trend continues, namely, the value of determination coefficient  $R^2$  is greater for stations with a high percentage of sand in the soil. So, the value of  $R^2 = 0.65$  obtained for the Imnaviat Creek with 73% sand content in the soil, and  $R^2 \approx 0.4$  for stations with 34% sand content in the soil (Prudhoe Bay, Coldfoot).

### 6. CONCLUSION

The paper deals with the distinction between thawed and frozen soils in the upper 5 cm layer for seven Alaska ground stations with a latitude from 65° N to 70° N according to S1 radar data for the period 2016-2017. Determining the status of the FS was carried

Table 5.

The  $\sigma_{thr}^0$  value from regression.

Наземная станция	Prudhoe Bay	Imnaviat Creek	Coldfoot	Upper Nome Creek
$\sigma_{thr}^0$ [dB]	-13.3	-17.94	-15.5	-11.25

out in two ways: 1) using radar data with finding the threshold values of the backscatter coefficient  $\sigma_{thr}^0$ , when the temperature in the 5-cm topsoil layer falls below 0°C, and 2) the joint use of radar data and ground-based measurements of soil temperature. In the latter case, the correlation between  $\sigma^0$  and soil temperature at different depths from 5 cm to 51 cm is determined. It is shown that the Spearman correlation coefficient is the highest between  $\sigma^0$  and soil temperature at a depth of 5 cm. In the case of high and moderate correlation, regression models are constructed for the relationship between  $\sigma^0$  and soil temperature at a depth of 5 cm for the stations Prudhoe Bay, Imnaviat Creek, Upper Nome Creek and Coldfoot with determination coefficients in the case of linear regression, respectively, 0.4, 0.64, 0.62 and 0.46. It is shown that DC increases with the increase of the percentage content of sand in the soil. The found threshold values  $\sigma_{thr}^0$  polarization VV allowed to construct local maps of frozen and thawed soils. A comparison of the  $\sigma_{thr}^0$  obtained by the two methods showed the proximity of the values, but the difference between the values increases as the correlation between radar and ground data decreases. The difference value is less than 1 dB with high correlation (Prudhoe Bay, Imnaviat Creek Upper Nome Creek) and more than 1 dB, with an average correlation (Coldfoot). Linear regression with  $R^2 = 0.97$  is obtained for the connection  $\sigma_{thr}^0$  VV polarization with site latitude.

## REFERENCES

1. Khaldoune J, Van Bochove E, Bernier M, Nolin MC. An approach for mapping frozen soil of agricultural land under snow cover using RADARSAT-1 and RADARSAT-2. *Proc. of IGARSS'2008. Boston Mass.*, 2008, Vol.III 382-385.
2. Khaldoune J, Van Bochove E, Bernier M, Nolin MC. Mapping agricultural frozen soil on the watershed scale using remote sensing data. *Appl. Environment. Soil Sci.*, 2011, Article ID 193237:1-16, doi: 10.1155/2011.193237.
3. Hallikainen MT, Ulaby FT, Dobson MC, El-Rayes MA, Wu LK. Microwave dielectric behavior of wet soil-part 1: empirical models and experimental observations. *IEEE Trans. GRS*, 1985, 23(1):25-34.
4. Way JB, Zimmermann R, Rignot E, McDonald K, Oren R. Winter and spring thaw as observed with imaging radar at BOREAS. *J. Geoph. Res.*, 1997, 102(24): 29673-29684.
5. Ulaby FT, Moore RK, Fung AK. *Microwave Remote Sensing: Active and Passive: Vol. 1. Fundamentals and Radiometry*. Artech House, Dedham, Mass, USA, 1982.
6. <https://ismn.geo.tuwien.ac.at/>.
7. <https://sentinel.esa.int/web/sentinel/toolboxes/sentinel-1>.
8. Mironov VL, Muzalevsky KV. Spaceborne radar monitoring of soil freezing/thawing processes in the arctic tundra. *Russian Physics Journal*, 2013, 55(8). (Russian Original No. 8, August, 2012).
9. Kim Y, Kimball JS, McDonald KC, Glassy J. Developing a global data record of daily landscape freeze/thaw status using satellite passive microwave remote sensing. *IEEE Trans. GRS*, 2011, 49(3): 949-960.
10. Rautiainen K, Parkkinen T, Lemmetyinen J, Schwank M, Wiesmann A, Ikonen J, Derksen Ch, Davydov S, Davydova A,

- Boike J, Langer M, Drusch M, Pulliainen J. SMOS prototype algorithm for detecting autumn soil freezing. *Remote Sensing of Environment*, 2016, 180:346-360.
11. Mironov VL, Muzalevskij KV. Kosmicheskij radiolokacionnyj monitoring processov zamerzaniya i ottaivaniya pochvy arkticheskoy tundry [Space radar monitoring of the processes of freezing and thawing of the soil in the Arctic tundra]. *Izvestiya vuzov. Fizika*, 2012, 55(8):40-43 (in Russ.).
12. Rodionova NV. Svyaz' radarnyh dannyh Sentinel 1 s nazemnymi izmereniyami temperatury pochvy [Sentinel 1 data correlation with ground measurements of soil temperature]. *Sovremennye problemy distancionnogo zondirovaniya Zemli iz kosmosa*, 2017, 14(5):135-148 (in Russ.).

# POTENTIAL OF PHASE MEASUREMENTS IN RADAR INTERFEROMETRY FOR THE OBSERVATION OF EMERGENCY SITUATIONS BUREYA LANDSLIDE CASE

Alexander I. Zakharov, Liudmila N. Zakharova

Kotelnikov Institute of Radioengineering and Electronics of RAS, Fryazino branch, <http://fire.relarn.ru>  
Fryazino 141190, Moscow Region, Russian Federation

[aizakhar@ire.rssi.ru](mailto:aizakhar@ire.rssi.ru), [zakharova@ire.rssi.ru](mailto:zakharova@ire.rssi.ru)

*Abstract.* The results of the European spaceborne Sentinel-1 synthetic aperture radar differential interferometry data processing for the Bureya landslide area aimed at detection and assessment the consequences of catastrophic event in December 2018 are presented. More than 20 scenes, obtained in SAR observations from relative orbits 134 and 61 for the period from December 2018 to March 2019 provided high temporal stability of signal backscatter from landslide slopes, were used. Analysis of phase measurements on interferograms with small spatial baselines and on differential interferograms (in the case of a large baseline) allows us reach the conclusion about temporal stability of the surface of the landslide circus during the entire period covered by the Sentinel-1 SAR observations. No noticeable (more than a few millimeters) small-scale displacements of the slopes in the end of January 2019 due to blasting operations in the riverbed cofferdam were revealed. We estimated landslide scales also. The volume of the ground that slid down the slope was not less than 18.5 million m<sup>3</sup>, the maximal vertical displacement of the scattering surface after the landslide compared with SRTM digital elevation model reached 140-150 m, the landslide area in the vertical projection is 22.8 ha. Thus, Sentinel-1 radar data demonstrated the its potential to monitor the stability of landslide slopes by means of radar interferometry technique and high-accuracy of the measurements of probable small-scale surface displacements provided the conduction of the radar observations in the winter time period.

*Keywords:* landslide, synthetic aperture radar (SAR), SAR interferometry, surface displacement measurement, digital elevation model

UDC 621.396.96

*Bibliography* - 16 references

*Received* 19.03.2019, *accepted* 17.04.2019

*RENSIT*, 2019, 11(1):31-38

DOI: 10.17725/rensit.2019.11.031

## CONTENTS

1. INTRODUCTION (31)
  2. BASICS OF THE METHOD (32)
  3. DATA FOR ANALYSIS (34)
  4. PROCESSING RESULTS AND DISCUSSION (34)
  5. CONCLUSION (37)
- LITERATURE (37)

## 1. INTRODUCTION

A catastrophic landslide on the Bureya River in December 2018 blocked its channel, creating a threat of flooding of nearby settlements, as well as the destruction of residential and industrial infrastructure located along the river downstream, due to a natural dam being projected for spring. Judging by the data of the multispectral sensor on the Japanese geostationary satellite Himawari-8,

the landslide came down on December 11, 2018 [1, 2]. The first ideas about the scale of a catastrophic natural phenomenon were obtained using an optical image from the satellite Sentinel-2 of December 12, which clearly shows the changes in the landscape: the location and the geometric dimensions of the landslide. The ground-based measurements carried out in January 2019 showed that the length of the landslide is 800 m, the volume of the descended soil was estimated at an approximate value of 24 million cubic meters. To restore the watercourse in the river in the layer of landslide rock in the period from January 22 to February 1, military experts conducted a series of explosions that formed the channel, which reduced the water level in the river above the dam. All-weather methods of radar surface observation,

including methods of radar interferometry, allow us to significantly expand our understanding of the scale and dynamics of the development of such natural phenomena.

Radar interferometry as a method for monitoring landslide processes has been widely used since the end of the last century thanks to the appearance of widely available data from foreign space synthesized aperture radar (PCA) X, C, L wavelengths [3]. Numerous examples of the application of this method show the possibility of detecting and measuring small-scale displacements of the reflecting surface of a landslide body with an accuracy of several millimeters, estimating its area, and long-term evolution of the landslide process [4-7]. The loss of coherence of reflected signals due to changing reflection conditions in comparatively short-wavelength XRD wavelengths, including in areas with developed vegetation cover, stimulated the development of classical methods of differential radar interferometry, which resulted in the creation of a method of constant reflectors method STAMPS [12], SQUEESAR [13], the method of small baselines (Small BASEline, SBAS) [14], and others. The essential requirements of the method of constant reflectors and similar ones are Xia need for long series of observations and the use of statistical analysis techniques to identify reliable reflectors. In this paper, due to the limited set of available radar images of the landslide territory, the classical method of differential radar interferometry will be used.

## 2. BASES OF THE METHOD

The method of radar interferometry is based on the use of information about the phase difference of the echo signals recorded by the radar system from the selected terrain area from two close points in space for which the condition of reciprocal coherence of the received echo signals is satisfied. At the same time, the phase difference of the received signals depends on the difference of the distances to the target and carries information about the surface relief, and in the two-pass version also about the change in the distances to the target during the time between surveys [15, 16].

The illustration of the geometry of the relief survey are shown in Fig. 1. The relief differences,

the height of the orbits of the satellites, and the distance between them for clarity, are not to scale, the geoid reference surface in the survey area is approximated by a plane. Point A1 is the first point of the survey, A2 is the second point of the survey, which may be, for example, on a different trajectory of the same apparatus, made some time later. Denote by H the height of the apparatus above the surface at the first point of the survey. The distance between the shooting points d1 is the base of the interferometer, which is oriented at an angle  $\alpha_i$  to the horizon. The radar signal from point A1 arrives at a point on surface P located at a distance r1 at an angle  $\alpha$  to the nadir direction and the local vertical.

The interferogram is the phase difference of the signals  $\Delta\varphi = \varphi_1 - \varphi_2$ , obtained as a result of the element-wise complex multiplication of the signals U1 and U2\*, taken at the points of space A1 and A2 from the same surface element:

$$U_1 U_2^* = u_1 u_2 \exp(j(\phi_1 - \phi_2)) = u_1 u_2 \exp\left(\frac{-j4\pi\Delta r}{\lambda}\right)$$

where u1 and u2 are the amplitudes of the signals,  $\Delta r$  is the difference of distances from the survey points to the selected surface element,  $\lambda$  is the wavelength.

The phase difference  $\Delta\varphi$  on the interferogram formed as a result of joint processing of a pair of radar images contains, in the first approximation, information about the relief (the so-called topographic phase  $\Delta\varphi_t$ ), small-scale dynamics (displacements) of the reflecting surface  $\Delta\varphi_d$ , phase fluctuations on the signal propagation path  $\Delta\varphi_a$ , thermal noise of the equipment and processing noise  $\Delta\varphi_N$ , etc. Restricting ourselves to the first two components, we write down [15, 16]:

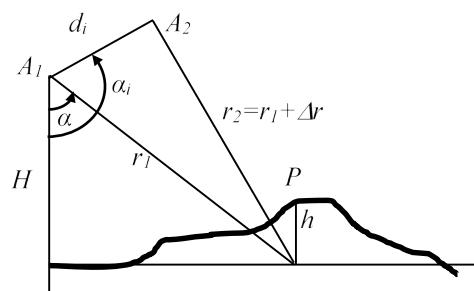


Fig. 1. The geometry of the interferometric survey of the surface topography.

$$\Delta\varphi_{12} = \Delta\varphi_t + \Delta\varphi_d = -\frac{4\pi d_p \Delta h}{\lambda r \sin \alpha} - \frac{4\pi \delta r_d}{\lambda}, \quad (1)$$

where the perpendicular component of the interferometric base is equal to

$$d_p = \text{disin}(\alpha_i - \alpha).$$

Note that the sensitivity of the interferometric phase difference to variations in the relief heights  $\Delta h$  increases with increasing base  $d_p$ , with decreasing wavelength  $0.5\lambda$ , viewing angle  $\alpha$  and slant distance to the surface  $r$ . For the Sentinel-1 radar, the wavelength  $\lambda = 5.6$  cm, the slant range from the radar to the surface of the landslide is 820 km. Small-scale displacement of the surface during the time between surveys is not marked in the figure due to its small size compared with the scale of the shooting geometry. Due to this displacement, for example, by the value  $\delta r_d = 0.5\lambda$  in (1), the phase difference on the interferogram changes by  $2\pi$ . An important numerical indicator of the sensitivity of  $\Delta\varphi_t$  to the relief is the ambiguity height  $h_a$ : such a difference in the height of the relief between two points on the ground, at which the values of the phase difference on the interferogram in the corresponding image elements differ by  $2\pi$ :

$$h_a = \lambda r (2d_p)^{-1} \sin \alpha.$$

To correctly interpret the phase information on the interferogram, it is necessary to take into account that with a positive value of  $d_p$ , according to (1), with increasing true surface height relative to the digital elevation model used in processing, the phase difference on the interferogram decreases. With a negative  $d_p$ , it grows. The effect of small-scale radial displacement of the surface during the time between surveys is such that when the surface subsides in a later survey, according to (1), the phase difference increases. It is necessary to note the impossibility of simultaneous measurements of the relief and small-scale radial displacements of the surface during the time between surveys. When solving the problem of analyzing the dynamics of the underlying surface, the output is the use of a digital elevation model (DTM) to compensate for the effect of the relief, or the choice of a pair of images with a very small base  $d_p$ , when the first component in (1) can be neglected.

The relative accuracy of measurements of heights within the frame of the survey is determined

by the coherence of the reflected signals at the survey points A1 and A2 in fig. 1. The degree of coherence of the echo signals of the two complex radar images U1 and U2 can be measured directly from radar data, it is determined by the following expression:

$$\gamma = \frac{E\{U_1 \cdot U_2^*\}}{\sqrt{E\{|U_1|^2\} E\{|U_2|^2\}}}, \quad (2)$$

where  $E\{\bullet\}$  is the operation of taking the expectation of some spatial ensemble of samples with the center in the current element of the image.

The main factors affecting the level of  $\gamma$  include primarily the decorrelation of  $\gamma_N$  caused by the thermal noise of the measuring system, the spatial decorrelation of  $\gamma_{sp}$  reflected signals caused by changes in reception conditions at various points in space, the temporary decorrelation of the conditions of reflection of signals  $\gamma_{td}$  due to separation of measurements in time and volume decorrelation when shooting layered covers with volumetric scattering  $\gamma_v$ . Restricting ourselves to the effects mentioned and assuming their independence, we write

$$\gamma = \gamma_N \gamma_{sp} \gamma_{td} \gamma_v. \quad (3)$$

Interferometric coherence characterizes the measurement errors of the phase difference and, accordingly, the relative interpixel accuracy of measuring the heights of the surface and the movements of the underlying surface [15, 16].

### 3. DATA FOR ANALYSIS

We used data from the European synthesized aperture radar Sentinel 1, which conducted the survey in IW (Interferometric Wide mode) mode. The standard frame width in this mode, consisting of 3 partial lanes, is 240 km. The landslide zone falls within the Sentinel-1 frame when observed from conventional paths 61 and 134. On the first path, the angle of incidence of the signal wave to the surface is  $32^\circ$  (partial band No. 1 of the SCANSAR Sentinel-1 mode), on the second -  $42^\circ$  (third partial strip). The repetition period is 12 days, so from the moment of the landslide collapse in early December of last year to mid-March 2019, at least 10 shooting sessions were conducted on each of the tracks suitable for interferometric processing. Tables 1 and 2 show the shooting dates for the formed pairs of shooting sessions, the dimensions of the perpendicular component of the interferometric base and the

ambiguity heights. The main combinations of images were pairs of images taken at intervals of 12 days. Processing combinations of images with a large interval between shots showed that this leads to a sharp decrease in the coherence of the reflected signals due to temporal de-correlation  $\gamma_{td}$  (see formula (3)) and, as a result, loss of informativeness of phase measurements.

We used data from the SLC (Single Look Complex) format. The distance between the pixels of the image by the slant range in this format is 2.3 m, between the lines 14.1 m. During the interferometric processing, averaging of data (4 pixels) by distance was applied to reduce the noise level. With this averaging, the pixel dimensions of the image in azimuth and ground range are about the same.

### 3. DATA FOR ANALYSIS

We used data from the European synthesized aperture radar Sentinel 1, which conducted the survey in IW (Interferometric Wide mode) mode. The standard frame width in this mode, consisting of 3 partial lanes, is 240 km. The landslide zone falls within the Sentinel-1 frame when observed from conventional paths 61 and 134. On the first path, the angle of incidence of the signal wave to the surface is  $32^\circ$  (partial band No. 1 of the SCANSAR Sentinel-1 mode), on the second -  $42^\circ$  (third partial strip). The repetition period is 12 days, so from the moment of the landslide collapse in early December of last year to mid-March 2019, at least 10 shooting sessions were conducted on each of the tracks suitable for interferometric processing. Tables 1 and 2 show the shooting dates for the formed pairs of shooting sessions, the dimensions of the perpendicular component of the interferometric base and the ambiguity heights. The main combinations of images were pairs of

Таблица 1.

Параметры интерферометрической съемки Sentinel-1 с условной трассы 134.

№ пары	Даты съемки, ггггммдд	$d_{p'}$ , м	$h_{a'}$ , м
1	20181128-20181210	61	251
2	20181210-20181222	83	185
3	20181222-20190103	-69	221
4	20190103-20190115	-90	170
5	20190115-20190127	40	381
6	20190127-20190208	50	308
7	20190208-20190220	39	395
8	20190220-20190304	-12	1304

Таблица 2.

Параметры интерферометрической съемки Sentinel-1 с условной трассы 61.

№ пары	Даты съемки, ггггммдд	$d_{p'}$ , м	$h_{a'}$ , м
1	20181123-20181205	34	520
2	20181205-20181217	-151	118
3	20181217-20181229	8	2222
4	20181229-20190110	51	351
5	20190110-20190122	16	1096
6	20190122-20190203	81	220
7	20190203-20190215	-149	120
8	20190215-20190227	9	1957
9	20190227-20190311	-30	594

images taken at intervals of 12 days. Processing combinations of images with a large interval between shots showed that this leads to a sharp decrease in the coherence of the reflected signals due to temporal de-correlation  $\gamma_{td}$  (see formula (3)) and, as a result, loss of informativeness of phase measurements.

We used data from the SLC (Single Look Complex) format. The distance between the pixels of the image by the slant range in this format is 2.3 m, between the lines 14.1 m. During the interferometric processing, averaging of data (4 pixels) by distance was applied to reduce the noise level. With this averaging, the pixel dimensions of the image in azimuth and ground range are about the same.

### 4. PROCESSING AND DISCUSSION RESULTS

Interferometric coherence is an important factor determining the level of noise on the interferogram, the accuracy of measurements of the relief and movements of the underlying surface. The quality of interferometric measurements of C-band radars is significantly affected by the temporal decorrelation of the reflected signals. The smaller the interval between surveys and the biomass of vegetation in the survey area, the higher the coherence. The season in which measurements are taken is also important: in winter, coherence, as a rule, increases due to the greater stability of the signal reflection conditions by frozen soil and vegetation. Graph of changes in the level of coherence of reflections on the surface of the landslide for pairs of sessions from the table. 1 is shown in Fig. 2

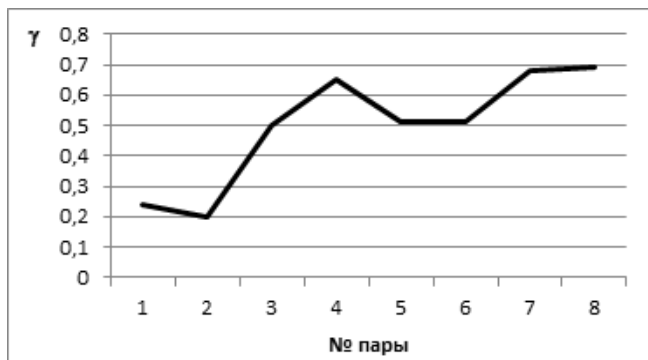


Рис. 2. Когерентность отраженных оползнем сигналов для пар сеансов из таблицы 1.

The first reading of the graph with a low  $\gamma$  level is explained by the high variability of the signal reflection conditions with unfrozen underlying covers. The next, even lower, coherence level for the pair 20181210-20181222 is explained by the completely changed micro-relief of the landslide surface after the ground has disappeared. Starting from the third pair (after December 22, 2018), the frozen soil and vegetation in the survey area become a very stable reflective environment, which makes it possible to evaluate the modified relief form in the landslide zone and judge the subsequent small-scale soil movements in case of their occurrence.

The detail on the interferogram that is characteristic of a landslide area under the condition of large values of  $d_p$  and, consequently, a good sensitivity of the phase measurements to the relief are the clearly distinguishable oval structures in Fig. 3b (a pair of sessions with a positive projection of the base  $d_p$ ) and 3c (a pair of sessions with a negative  $d_p$ ).

The relief in the place of the landslide circus does not correspond to the digital model: a recess

appeared on the slope of the hill. Because of the relief underestimated in this way, in the first case the phase grows from the edges of the circus to its conditional center (the brightness of the phase image increases in accordance with the adopted encoding, Fig. 3b). In the second case, since the base of the interferometer has the opposite sign, the phase difference decreases, the brightness decreases. A similar picture is valid for all pairs of sessions from Tables 1 and 2 up to mid-March 2019, with the exception of pairs of sessions with small interferometric bases, which allows us to make an assumption about the dominance of the relief in these time intervals, since surface subsidence going in the same direction relative to the radar, lead to a monotonous increase in the phase difference, according to (1).

It should also be noted that in both interferograms of fig. 3 phase jump line by  $2\pi$ , clearly visible in the right side of the oval circus, is absent in its left side. This is due to the effect of distortion of radar images: during side shooting, the slopes facing the antenna are compressed. In fig. 3 radar emits a signal on the right. Thus, the edge of the landslide circus furthest from the antenna is compressed on the amplitude image into a bright narrow band (Fig. 3a), and it is not possible to track the phase progress on the interferogram; the averaging of 4 pixels over the range mentioned earlier, as well as the filtering of the interferogram lead to the final form of the open ring shown in Fig. 3b and 3c.

When solving the problem of detecting the dynamics of the relief during the time of shooting, one of the methods to reduce the effect of uncompensated relief on the interferogram is a careful selection of the base of the interferometer:

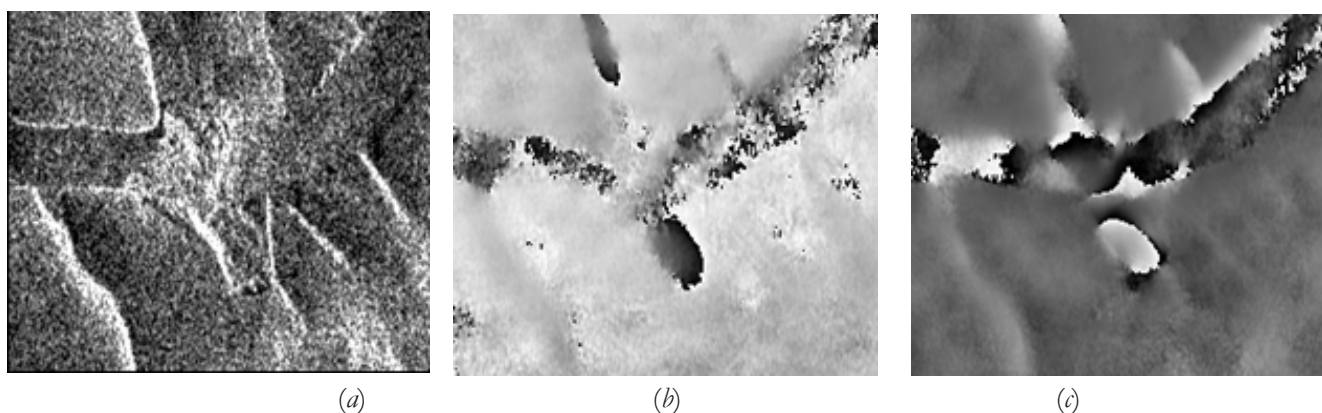


Рис. 3. Амплитудное изображение (a), интерферограмма с положительной  $d_p$  (b) и интерферограмма с отрицательной  $d_p$  (c).

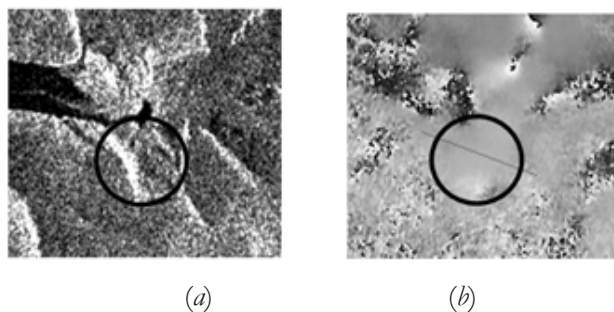


Рис. 4. Амплитудное изображение (a) и интерферограмма (b) для пары сеансов с малой базой.

considering pairs of images only with small bases, which allows to neglect the  $\Delta\varphi_t$  component in (1). In our case, this is a pair of table 8. 1 and pairs 3, 5, 8 table. 2. With a small, about 15 m, length of the base and an ambiguity height corresponding to it of about 1000 m (see, for example, a pair of 5 table 2), an error in the height of the relief  $\Delta h = 100$  m in (1) will lead to the same change phase on the interferogram, which occurs when a small-scale radial displacement of the surface by  $\lambda / 20$ , or only 2.8 mm.

A typical interferogram for such pairs (a pair of sessions February 15-27, 2019) is shown in Fig. 4.

On the profile of the phase difference Fig. 5, crossing the landslide in the transverse direction (the position of the profile line is shown in Fig. 4b), there are no noticeable phase changes, except for minor fluctuations within 0.5 radians. The possible displacement of the surface corresponding to this phase change does not exceed 2 mm. Similar results were obtained when using pairs of images on December 17–29, 2018 (8 m base) and December 10–22, 2019 (16 m base), which suggests that there was no small-scale surface dynamics at the end of the landslide. December, mid-January and late February.

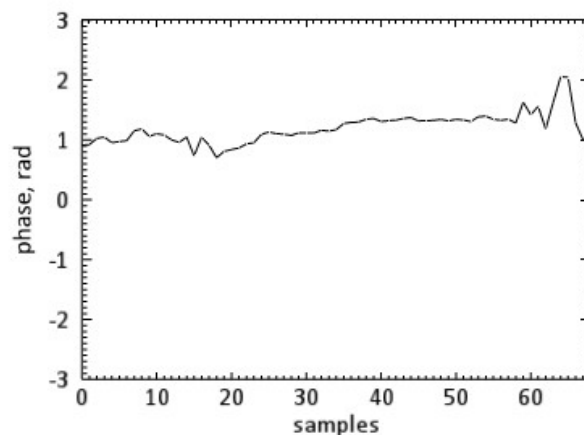


Рис. 5. Значения разности фаз вдоль профиля на рис. 4b.

The period of active blasting from January 22 to February 1, 2019 is covered with pairs of images with relatively large interferometer bases, and therefore the phase on the interferograms of pairs 5 and 6 from table 1, as well as pair 6 from table 2, was subtracted from the phase  $\Delta\varphi_t$ . This component was estimated according to the pairs of sessions, taken under the conditions of a known stable landslide surface.

In fig. 6 shows an example of subtracting the topographic phase of a pair of sessions 20190208-20190220 from a pair 20190115-20190127. Judging by the resulting phase (Fig. 6c), there are no manifestations of small-scale dynamism of the landslide surface during blasting operations at the end of January. Similar results were obtained for couples 20190122-20190203, 20190127-20190208.

To estimate the amount of ground deposited by a landslide, let's take a pair of number 4 from the table. 1, covering the period from 3 to 15 January 2019, before the start of active blasting. Since the digital terrain model SRTM, built long before the landslide, was used to construct the interferogram

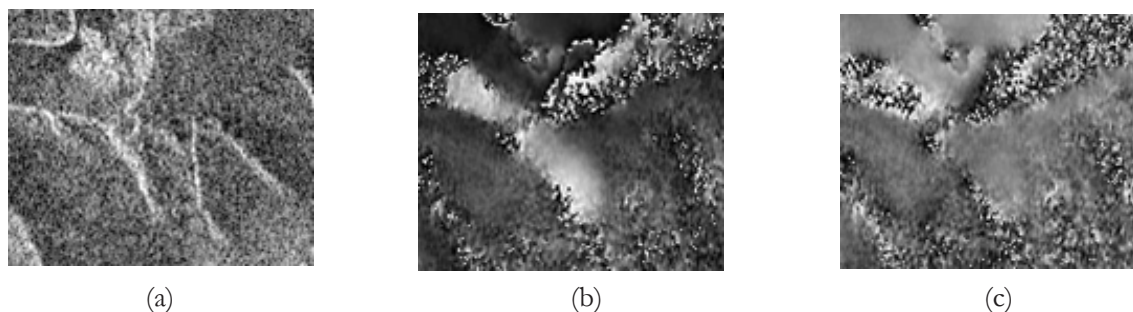


Рис. 6. Амплитудное изображение (a), интерферограмма до коррекции топографической фазы (b) и скорректированная интерферограмма (c).

for correcting the topographic phase, the relief modified at this location as a result of the landslide collapse is clearly seen on the interferogram (Fig. 3c). The place of the landslide on the interferogram is noticeable here due to the bright oval spot at the bottom of the figure. Integrating the phase difference within the landslide allowed us to estimate the amount of rock mass carried out. According to our estimates, taking into account the ambiguity height of 119 m for the interferometric pair used and the pixel area on the interferogram of 187 m<sup>2</sup>, the volume of the ground spread by the landslide was 18.5 million m<sup>3</sup>. The maximum vertical displacement of the reflecting surface relative to the SRTM terrain model after a landslide has reached 140-150 m, the landslide area in the vertical projection is 22.8 hectares.

**5. CONCLUSION**

The methods of radar interferometry are an effective tool for measuring the parameters of the terrestrial surface and identifying the small-scale dynamics of the underlying covers. The scale of the landslide phenomenon and the volume of rocky ground taken from the landslide slope on the Bureya River are estimated. It turned out that the volume of soil removed by a landslide in December 2018 amounted to 18.5 million m<sup>3</sup>, the landslide area in the vertical projection is 22.8 ha. The maximum vertical displacement of the reflecting surface relative to the SRTM terrain model after a landslide has reached 150 m. Despite the generally low quality of classical interferometric measurements by radars of such a relatively short wavelength range as on Sentinel-1, especially in areas with developed vegetation cover, it was possible to apply the methods classical radar interferometry due to the presence of images taken during the cold season, which provided a high temporal coherence nnyh signals.

**REFERENCES**

1. DC FGBU NIC "PLANET". Space monitoring of the situation on the Bureya River 2018-12-24. [https://www.dvrcpod.ru/News.php?id\\_new=2821](https://www.dvrcpod.ru/News.php?id_new=2821).
2. Kramareva LS, Lupyan EA, Amelchenko YuA, Burtsev MA, Krashennnikova YuS, Sukhanova VV, Shamilova YuA. Observation of the collapse zone of the fells near the Bureya River

- on December 11, 2018. Sovr. problems Earth remote sensing from space, 2018, 15 (7): 266-271.
3. Colesanti C, Wasowski J. Investigating landslides with space-borne Synthetic Aperture Radar (SAR) interferometry. *Engineering Geology*, 2006, 88: 173-199.
4. Fruneau B, Achache J, Delacourt C. Observation and Modeling of the Saint-Etienne-de-Tinée Landslide Using SAR Interferometry. *Tectonophysics* 1996, 265: 181-190.
5. Rott H, Scheuchl B, Siegel A, Grasemann B. SAR interferometry: a case study above the alts, Austria. *Geophys. Res. Lett.*, 1999, 26: 1629-1632.
6. Rott H, Mayer C, Siegel A. Alpine areas. Proc. International Conference on Synthetic Aperture Radar (EUSAR 2000), Munich, Germany, 2000.
7. Kimura H, Yamaguchi Y. Detection of landslide areas using satellite radar interferometry. *Photogrammetric Engineering and Remote Sensing*, 2000, 66: 337-344.
8. Ferretti A, Prati C, Rocca F. Permanent scatterers in SAR interferometry. Proc. Geoscience and Remote Sensing Symposium (IGARSS 1999), Hamburg (Germany), 28 June–2 July 1999, vol. 3, pp. 1528-1530.
9. Ferretti A, Prati C, Rocca F. Nonlinear Subscription Rate for Permanent Scatterers in Differential SAR Interferometry. *IEEE Trans. Geosci. Remote Sens.*, 2000, 38 (5): 2202-2212.
10. Colesanti C, Ferretti A, Prati C, Rocca F. Monitoring landslides and tectonic motion with the Permanent Scatterers technique. *Engineering Geology*, 2003, 68: 3-14.
11. Colesanti C, Ferretti A, Novali F, Prati C, Rocca F. Sort. *IEEE Trans. Geosci. Remote Sens.*, 2003, 41: 1685-1700.
12. Ferretti A, Fumagalli A, Novali F, Prati C, Rocca F, Rucci A. A new algorithm for processing interferometric data-stacks: SqueeSAR. *IEEE Trans. Geosci. Remote Sens.*, 2011, 49 (9): 3460-3470.
13. Hooper A, Zebker H, Segall P, Kampes B. Using InSAR persistent scatterers. *Geophys. Res. Lett.*, 2004, 31 (23).
14. Berardino P, Fornaro G, Lanari R, and Sansosti E. SAR interferograms. *IEEE Trans. Geosci.*

- Remote Sens. 2002, 40 (11): 2375–2383.
15. Rosen PA, Hensley S, Joughin IR, Li FK, Madsen SN, Rodriguez E, and Goldstein RM. Synthetic aperture radar interferometry. Proc. IEEE, 2000, 88 (3): 333-392.
  16. Zakharov A.I., Yakovlev O.I., Smirnov V.M. Satellite monitoring of the Earth: Radar surface sensing. M., URSS, 2015, 248 p.

## MICROWAVE SCATTERING IN DRY LAYERED SNOW

Valery A. Golunov

Kotelnikov Institute of Radioengineering and Electronics of RAS, Fryazino branch, <http://fire.relarn.ru>  
Fryazino 141190, Moscow Region, Russian Federation

[golsnow@mail.ru](mailto:golsnow@mail.ru)

*Abstract.* The problem of the applicability of the two-stream Kubelka-Munk theory to the description of the radiative characteristics of snow cover is discussed. It is shown that since the microwave thermal radiation of snow is received by radiometers with a spatially coherent input, this is equivalent to the irradiation of scattering media by a spatially coherent and, as a rule, narrowly directed source, and the scattered radiation is received by an infinitely long areal receiver. The problem of the applicability of the known formulas for calculating the reflection and transmission coefficients of multilayer snow cover is considered, since the conditions for the applicability of these formulas and the Kubelka-Munk theory coincide. Moreover, the considered formulas do not take into account the reflection of flows at the boundaries between the layers. In the snow cover, the reflecting boundaries are caused by a jump in the refractive index due to the difference in the values of the bulk density of snow in adjacent layers. Measured at frequencies of 22.2, 31, 37.5 and 94 GHz, the values of the reflection and transmission coefficients of single-layer and multi-layer snow were compared with their calculated values. It is shown that, firstly, the measured dependences of the reflection and transmission coefficients on the thickness of single-layer snow are satisfactorily approximated by the corresponding formulas of the Kubelka-Munk theory. Secondly, the discrepancies between the calculated and measured values of the above factors for two-, three- and four-layer snow practically do not go beyond the limits of coarse measurement error. The experimentally observed negligibly small effect of the boundaries is interpreted by the fact that the calculations use the values of the reflection and transmission coefficients measured for each of the folded layers. These values already contain contributions from the reflections of scattered fluxes on the interlayer boundaries, of which the outer boundaries of the first and last layer are most important in the snow stack. The feasibility of creating a database of microwave radiation characteristics of a uniform (single-layer) dry snow cover with a wide set of parameters of its structure based on experimental data and a two-stream Kubelka-Munk model is shown. In this case, it becomes possible to simply and accurately predict the brightness characteristics of the layered snow cover.

*Keywords:* microwave emission, volume scattering, two-stream model, layered snow cover, experiment

UDC 535.36; 621.396.11

*Bibliography* - 27 references

Received 19.04.2019, accepted 24.04.2019

RENSIT, 2019, 11(1):39-48

DOI: 10.17725/rensit.2019.11.039

### CONTENTS

1. INTRODUCTION (39)
  2. RADIOMETRIC SETUP AND MEASUREMENT TECHNIQUES (41)
  3. THE BASIC RELATIONS OF THE KUBELKA-MUNK THEORY FOR SINGLE-LAYER SCATTERING MEDIA (41)
  4. REFLECTANCE AND TRANSMITTANCE OF LAYERED SNOW (42)
  5. SNOW WITH THE UPPER CRUST (44)
  6. SNOW IS SITUATED AT SURFACE OF A STRONGLY SCATTERING LAYER (45)
  7. DISCUSSION OF THE RESEARCH RESULTS (46)
  8. CONCLUSION (47)
- REFERENCES (47)

### 1. INTRODUCTION

The relevance of research on the global characteristics of snow cover, such as the extent and spatial distribution of water equivalent and thickness of cover, is due to the fact that snow cover is an important part of the cryosphere, which has a profound effect on global climate change and energy balance. One of the ways to study snow cover is a method of microwave passive remote sensing from space. The radiophysical basis of the method is the spectral dependence of the intensity

of thermal radiation of dry snow cover on its density and thickness. This dependence is due to the effect of volume scattering of microwave radiation on ice particles of snow cover. To date, there are many algorithms for recovering the parameters of snow cover when sounding from space, which, however, do not provide the necessary accuracy of recovery. The main reasons are, on the one hand, the extremely wide range of possible values of the snow structure parameters and the layering of snow cover, on the other hand, the limited applicability conditions of the developed rigorous theoretical methods to describing the effects of volumetric scattering of microwave radiation in snow cover.

To date, there are many algorithms for restoring the parameters of snow cover when sounding from space, which, however, do not provide the necessary accuracy of restoring. The main reasons are, on the one hand, the extremely wide range of possible values of the snow structure parameters and the layering of snow cover, on the other hand, the limited applicability conditions of the developed rigorous theoretical methods to describing the effects of volume scattering of microwave radiation in snow cover.

The developed algorithms for the restoring the parameters of snow cover are based exclusively on models that use different approximations of radiative transfer in scattering media. The topic of volume scattering is inextricably linked with the development of optics. Probably, there is not a single natural environment in which volumetric scatterers would not be present, in connection with which the term “turbid” media existed at one time [1, 2].

The fundamentals of radiative transfer theory were created in the middle of the last century by Ambartsumian, Sobolev and Chandrasekhar [3-5]. By the end of the 1950s, as follows from the well-known review of Rosenberg [1], in connection with the rapid development of optical spectroscopy methods on scattering media, almost 1000 papers were published. In the microwave range, the development of research on the effects of volume scattering is associated with the technology development at the centimeter and

millimeter wavelengths, when a strong influence of precipitation and clouds on radar signals and communication channels was discovered. But the strongest, one can say, extreme scattering was found precisely in the dry snow cover on millimeter waves [6].

At first glance, the most efficient method for calculating the intensity of snow cover radiation is the radiative transfer equation method [1, 7]. However, for its application, it is necessary to accurately calculate the phase function, which is possible only with the help of rigorous theoretical methods, which are valid, as a rule, only for weakly scattering media.

In this regard, both in optics and in the microwave range, the two-stream Kubelka-Munk theory [8, 9] is widely used. Numerous studies have shown that this theory is in good agreement with the experimental results obtained with diffuse illumination of scattering media [1, 9]. Strict implementation of the conditions of applicability of the two-stream Kubelka-Munk theory is possible, for example, when using a special stand with integrating mirror spheres [10].

With a passive location, the thermal radiation of a scattering object and the radiation of the surrounding space that illuminates it can be approximately considered as corresponding to the conditions of applicability of the Kubelka-Munk theory. However, microwave thermal radiation is received by radiometers, which usually have a single-mode waveguide input. This means that such radiometers are spatial-coherent receivers. Consequently, in radiometric measurements of reflectance and transmittance of a scattering layer, we can assume that, in accordance with the reciprocity principle, a layer is illuminated with a spatially coherent beam (collimated at best), and the scattered radiation is received by an infinite size sensitive plate. Thus, with microwave radiometric measurements, the conditions of applicability of the Kubelka-Munk theory are violated. Various approaches are known to combine the attenuation of coherent intensity with the Kubelka-Munk theory [9–12]. Since a strict solution of this problem is possible only by solving a radiative transfer equation, all the options

## RADIOLOCATION

associated with the use of the Kubelka-Munk theory are approximate. Their main disadvantage is inaccurate values of the absorption and scattering coefficients, which were retrieved from the results of measurements of the reflectance and transmittance of the scattering layer [1, 10]. This disadvantage is important if the main purpose of the measurement is precisely in the restoration of these quantities, for example, in the spectral analysis of powder media [1]. To solve the problems of passive remote sensing of snow cover, it is sufficient that the model describes with required accuracy the experimentally obtained dependences of the reflectance and transmittance on the layer thickness with empirical values of the absorption and scattering coefficients.

To date, similar models of snow emission in the microwave range have been developed [13–15], but their successful practical application requires more detailed experimental confirmation and further development.

One of the solvable problems of models based on the Kubelka-Munk theory is to take into account the influence of the boundaries of the layered medium [16]. When a plane wave propagates in scattering media, it is known [16] that forward and back scattered radiation flows are formed. The intensity of their reflection from the interface of the media is determined simultaneously by the scattering indicatrices, the dielectric properties of the media and the roughness of the interface. For a layered snowpack, all flows repeatedly reflected by boundaries and layers can be taken into account using approximate models with certain assumptions. In the framework of the Kubelka-Munk theory, formulas are derived for calculating the reflectance and transmittance of a multilayer scattering medium [17, 18], which do not take into account the boundaries and are just like the Kubelka-Munk theory under diffuse illumination.

The goal of this paper is to experimentally evaluate the applicability of the Kubelka-Munk theory for calculating reflectance and transmittance of thermal radiation from a layered snow cover. The novelty of this study lies in the fact that the original method and radiometric setup [19, 20] are used, allowing to measure the above factors for both

individual layers of snow and their combination. So far, such measurements have not been carried out.

## 2. RADIOMETRIC SETUP AND MEASUREMENT TECHNIQUES

A detailed description of the used technique and radiometric setup is given in [20]. Here we note that measurements of reflectance and transmittance of the snow layer (and artificial snow-like media) were carried out in a laboratory room. Snow samples were loaded into metal cylinders with a diameter of 0.2m and a height of from 0.01 to 1m. The bases of the cylinders were covered with foam plates with a thickness of 0.005 m, and the side surfaces had insulating shells. For collimation of the receiving beam, a dielectric lens with a diameter of 0.2 m and a focal length of 0.4 m was used. During measurements, the samples were mounted close to the lens. On the other side of the lens there was a metal closed chamber. At the base of the chamber a black body cooled by liquid nitrogen was placed. Such black body was necessary for creating a “cold” brightness illumination of the samples. This paper presents the results of measurements at frequencies of 22.2, 31, 37.5, 60 and 94 GHz. A systematic calibration of radiometers with the installation of standards close to the lens and the developed algorithm for relative measurements provided a reliable account of changes in the brightness background and the brightness temperature of the reference black bodies..

## 3. THE BASIC RELATIONS OF THE KUBELKA-MUNK THEORY FOR SINGLE-LAYER SCATTERING MEDIA

The brightness temperature of the upward thermal radiation of the snow cover formed on the ground surface, neglecting the effect of their interface can be written as:

$$T(h) = [1 - R(h) - t(h)]T_{sn} + t(h)T_{gr} + R(h)T_a^*, \quad (1)$$

where  $R$  and  $t$  are reflectance and transmittance of a snow layer with thickness  $h$ ,  $T_{sn}$  and  $T_{gr}$  are thermodynamic temperatures of snow and ground,  $T_a^*$  is the brightness temperature of the illuminating radiation of the environment. In accordance with the Kubelka-Munk theory, the

reflectance and transmittance are determined by the following relations:

$$R_{KM}(h) = \frac{R_0[1 - \exp(-2\alpha_{KM}h)]}{1 - R_0^2 \exp(-2\alpha_{KM}h)}, \quad (2)$$

$$t_{KM}(h) = \frac{(1 - R_0^2) \exp(-\alpha_{KM}h)}{1 - R_0^2 \exp(-2\alpha_{KM}h)}, \quad (3)$$

where  $R_0 = 1 + \frac{K}{S} - \sqrt{\frac{K^2}{S^2} + 2\frac{K}{S}}$  – reflectance of semi-infinite layer,  $\alpha_{KM} = \sqrt{K(K+2S)}$ ,  $K$  and  $S$  – absorption and backscattering coefficients respectively.

Processing the experimental data obtained earlier for sufficient homogeneous snow [21–23] showed that relations (2) and (3) very well approximate the measured dependences of the reflectance  $R(h)$  and transmittance  $t(h)$ . Fig. 1a,b show the data of  $R(h)$  and  $t(h)$  used hereinafter, measured at 22.2 GHz (Fig. 1a) and 37.5 GHz (Fig. 1b) for samples snow taken from different layers of non-uniform snow cover.

As follows from the presented data, due to the inhomogeneous structure of snow, a certain scatter of the experimental values of the transmittance and reflectance is observed. In this regard, for each frequency, two families of approximation dependences shown in Fig. 1a,b in the form of solid and dashed lines were determined by simulation with Kubelka-Munk functions (2), (3).

The fitting values of the model coefficients are given in Table 1.

Table 1.

The fitting values of the Kubelka-Munk coefficients for data shown in Fig. 1a,b.

Model coefficients	Frequency, GHz			
	22.2		37.5	
	index of line		index of line	
	1,4	2,3	1,4	2,3
K, 1/cm	0.0073	0.004	0.015	0.012
S, 1/cm	0.0064	0.0033	0.0115	0.0063
$\alpha$ , 1/cm	0.00121	0.0065	0.0239	0.0172
$R_0$	0.248	0.239	0.228	0.178

A comparison of experimental data with approximation curves shows that in the samples under studied there are two types of snow with different structures, one of which is dominant.

Thus, the analysis of the data shown in Fig. 1, confirms that the Kubelka-Munk theory is proper approximation for dependences of the transmittance and reflectance of a snow layer on its thickness in the microwave range.

#### 4. REFLECTANCE AND TRANSMITTANCE OF LAYERED SNOW

To calculate the reflectance and transmittance under diffuse illumination of a scattering medium consisting of  $n$  layers, the following formulas were obtained in [17, 18]:

$$R_{1,2,3,\dots,n} = R_1 + \frac{t_1^2 R_{2,3,\dots,n}}{1 - R_1 R_{2,3,\dots,n}}, \quad (4)$$

$$t_{1,2,3,\dots,n} = \frac{t_1 t_{2,3,\dots,n}}{1 - R_1 R_{2,3,\dots,n}}, \quad (5)$$

where  $R_1$  и  $t_1$  – reflectance and transmittance of the first layer, and  $R_{2,3,\dots,n}$  и  $t_{2,3,\dots,n}$  – of the next

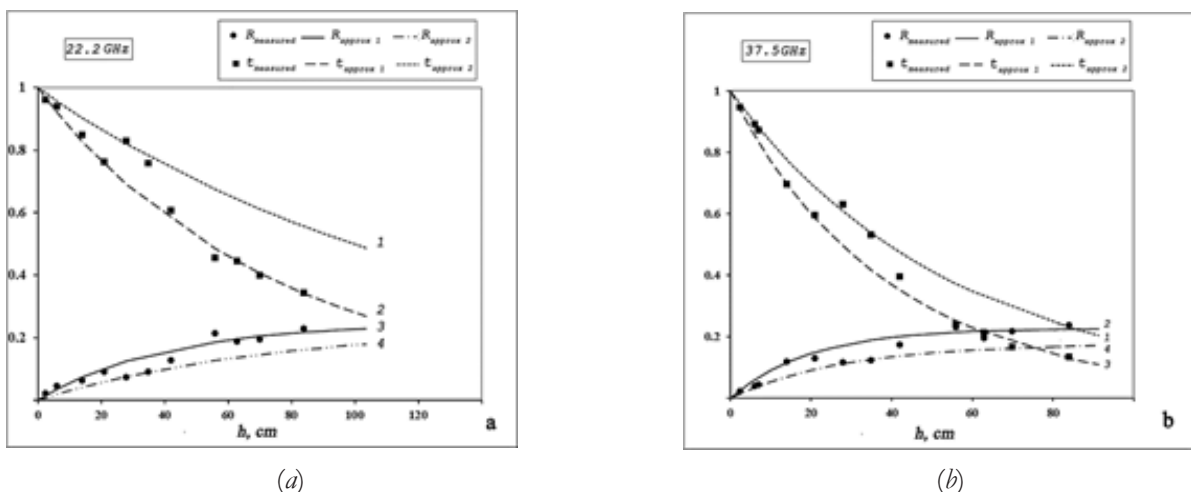


Fig. 1. Experimental and approximation dependences of transmittance and reflectance of snow at frequencies of 22.2 GHz (a) and 37.5 GHz (b).

( $n-1$ ) layers. Coefficients  $R_{2,3...n-1}$ ,  $t_{2,3...n-1}$  and  $R_{i,i+1...n-1}$ ,  $t_{i,i+1...n-1}$ , where  $i = 3, 4, \dots, n-1$ , are calculated in the same way.

Formulas (4), (5) were obtained in [17, 18] for such homogeneous layers, the reflectance and transmittance of which do not depend on the choice of the illuminated surface. In addition, as noted in [1], these formulas are strictly fulfilled only if the angular structure of the field remains constant throughout the entire thickness of the layers and at their boundaries. Therefore, in all other cases, these formulas are approximate. The objective of the experimental study, therefore, is to assess the possibility of using formulas (4) and (5) for calculating the reflectance and transmittance of a layered snow cover under narrowly targeted reception of its thermal radiation.

To study the reflection and transmission of layered snow, snow samples were used at various thicknesses (from 0.2 to 1 m) and snow bulk density (0.2...0.48). The use of samples with a thickness of up to 1m made it possible to ensure sufficiently large differences in the reflectance and transmittance of the add layers at frequencies of 22...37.5 GHz.

The results of measurements of the reflectance and transmittance of two, three and four-layer snow at frequencies of 22.2, 31 and 37.5 GHz are shown in Fig. 2a and 2b.

The experimental data are plotted on the abscissa, and the calculated ones – on the

ordinate. The dashed-dotted lines correspond to the function  $y = x$ , and the dotted lines correspond to the functions  $y = x + 0.03$  in Fig. 2a, and  $y = x + 0.04$  - in Fig. 2b. It can be seen that the vast majority of data are between the dashed lines. The absolute measurement error for a layered medium is roughly estimated on the basis of the fluctuation sensitivity of radiometers as not worse than 0.04, which satisfactorily corresponds to the intervals between the dotted lines. However, as follows from the analyzed graphs, there is a slight positive shift in the calculated values of reflectance and transmittance relative to the measured ones. It can be assumed that the source of the displacement of the calculated data is the effect of the boundary between the layers, due to the difference in their bulk density and, more significantly, the foam plates at the bases of the measuring cylinders. Each plate has a thickness of 5 mm; therefore, a non-scattering and nonabsorbent layer with 10 mm thickness appears between the layers when they are closed. From a general consideration of radiative transfer, it follows that any reflection at the boundaries of the scattering layer leads to a decrease in its transmittance and reflectance. Therefore, since in the formulas (4), (5) used, the reflection effects on the boundaries are not taken into account, the calculated values of the transmittance and

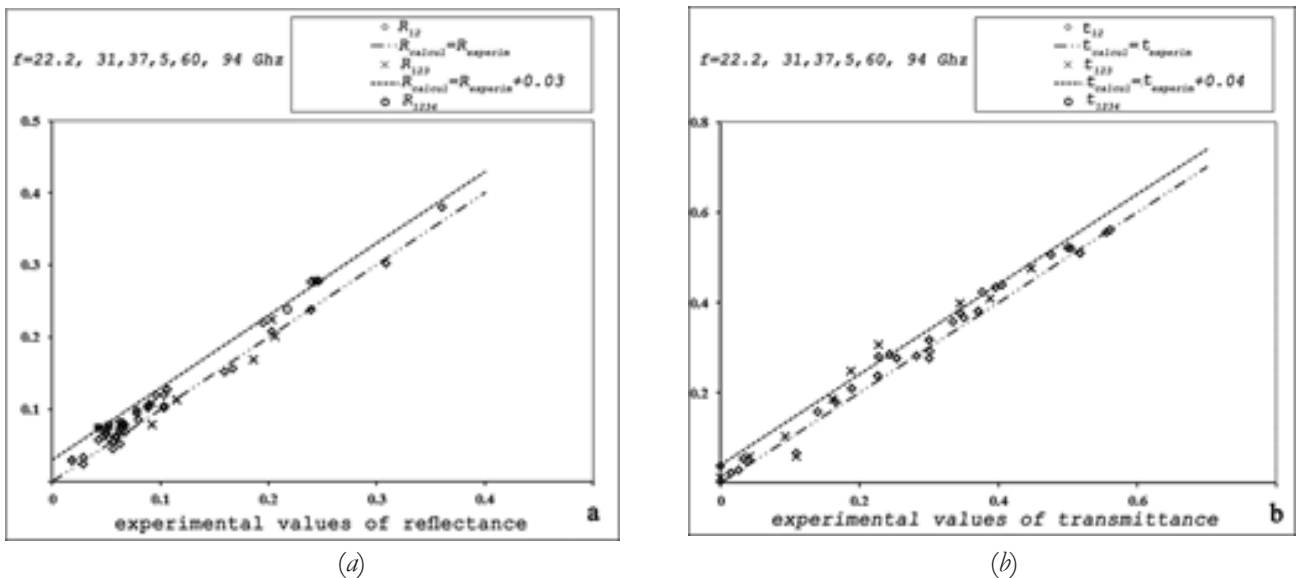


Fig. 2. Calculated and experimental values of reflectance (a) and transmittance (b) of layered snow.

reflectance turned out to be higher than the measured ones.

**5. SNOW WITH THE UPPER CRUST**

Let us consider a typical case, when as a result of a snow melting and subsequent refreezing, crusts form at the surface of the snowpack. They differ from the adjacent layer by higher values of bulk density and, as a rule, by a coarse-grained structure of snow. The thickness of the crusts may be different.

Fig. 3a,b show graphs of the dependences of the transmittance and reflectance on the thickness of the crust, snow layer and snow layer with the upper crust for radiation with a frequency of 37.5 GHz. Values of bulk density of the crust and snow and the fitting values of the Kubelka-Munk coefficients used for approximation to its experimental data are reported in Table 2.

From Table 2 it follows that absorption and scattering coefficients for the crust are 2-3 times higher than for the subcortical snow. In this case the difference is mainly due to coarse-grained structure of the crust, because, as shown in [24], at values of bulk density of granular snow of 0.2...0.4, the scattering intensity is almost constant.

The results of calculations and measurements of the reflectance and transmittance at the frequencies of 37.5 GHz of a two-layer medium formed by the crust and snow are reported in Table 3.

As a result of the analysis of tabular data, the difference between the calculated and measured

Table 2.

Bulk density and fitting Kubelka-Munk coefficients for the crust and snow

structure	$\rho_v$	$K, \text{cm}^{-1}$	$S, \text{cm}^{-1}$	$\alpha_{KM}, \text{cm}^{-1}$	$R_0$
crust	0.32...0.37	0.017	0.024	0.0332	0.323
snow	0.28...0.3	0.01	0.0075	0.0158	0.225

values of transmittance for crusts with the snow layer thickness of 0.76 m is found to exceed the gross error. To interpret this effect, we use the reflectance and transmittance data measured at 94 GHz, shown in Fig. 4. At this frequency, the scattering in the snow is so much stronger than at frequencies below 37 GHz that the thickness of the reflecting layer is an order of magnitude less.

For this reason, at a frequency of 94 GHz, irregularities are found in the structure of samples in their near-surface layer. So, from Fig. 4 it follows that the snow sample with a thickness of 0.76 m had the lowest reflectance in comparison with other samples. This means that snow in this sample, at least in the upper layer with a thickness of up to 0.3 m, had a finer grained structure. If all the snow in the sample had such a fine structure, it would appear at lower frequencies through noticeable deviations of the measured data from the approximation curves in Fig. 3. However, as can be seen in Fig. 3, the deviations indicated are negligible. Consequently, in the snow sample with a thickness of 0.76 m there is a local inhomogeneity of the structure, as a result of which an additional error occurs when calculating the transmittance using formula (4).

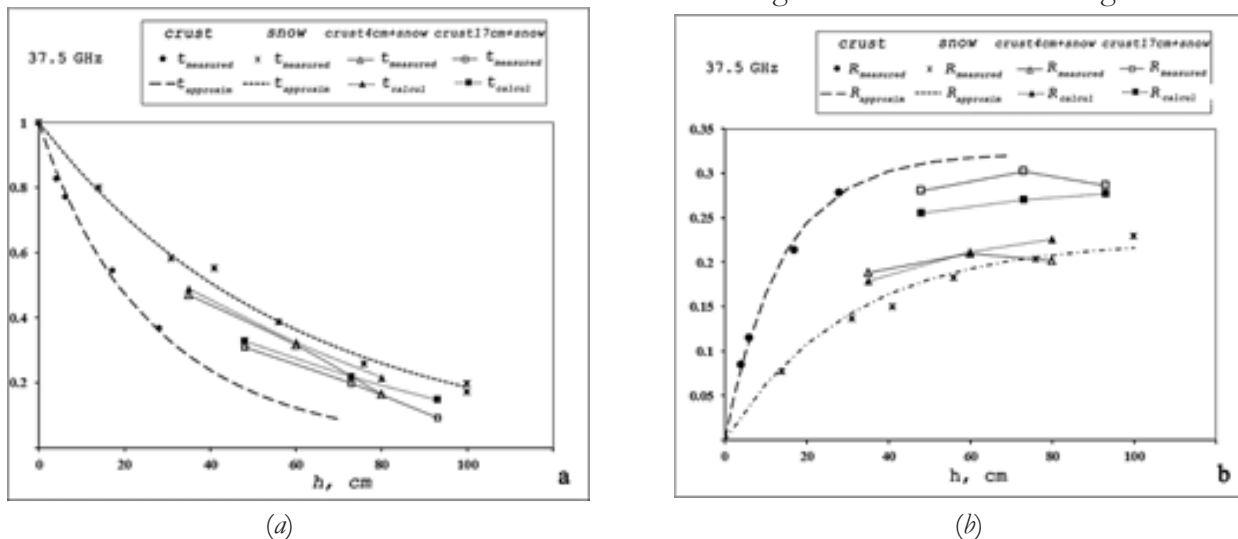


Fig. 3. Plots of transmittance (a) and reflectance (b) for crusts, snow and snow with upper crusts.

Table 3.

Calculated and measured values of the reflectance and transmittance of the crust with snow at the frequency of 37.5 GHz.

crust thickness, cm	crust with snow thickness, cm	thickness of snow layer, cm	$R_{calcul}$	$R_{measured}$	$t_{calcul}$	$t_{measured}$
4	35	31	0.18	0.19	0.49	0.47
	60	56	0.21	0.21	0.32	0.32
	80	76	0.23	0.20	0.22	0.16
17	48	31	0.26	0.28	0.33	0.31
	73	56	0.27	0.30	0.22	0.2
	93	76	0.28	0.29	0.15	0.09

Table 4.

Calculated and measured values of the reflectance and transmittance at the frequency of 31 GHz for the crust with snow.

crust thickness, cm	snow layer thickness, cm	$R_{calcul}$	$R_{measured}$	$t_{calcul}$	$t_{measured}$
6	56	0.16	0.17	0.44	0.44
	76	0.18	0.16	0.38	0.32
	100	0.22	0.22	0.28	0.27
17	56	0.22	0.23	0.36	0.35
	76	0.23	0.22	0.31	0.25
	100	0.25	0.26	0.23	0.22

Confirmation of this fact is the data obtained for the frequency of 31 GHz and are given in Table 4. And in this case, as can be seen from Table 4, the largest error in the calculated data of the transmittance was obtained for a snow sample with a thickness of 0.76 m.

Thus, when calculating the reflectance and transmittance by formulas (3) and (4), indeed, additional errors may occur due to the heterogeneity of the folded layers [18].

### 6. SNOW IS SITUATED AT SURFACE OF A STRONGLY SCATTERING LAYER

Let us consider another typical case when strongly scattering coarse snow or depth hoar forms due to metamorphism at the base of the snowpack. In the formulation of the next experiment, emphasis was placed not only on the strong difference in the scattering properties of the folding layers, but also on the strong difference in their refractive indices to enhance the influence of the boundary. To estimate the refractive index  $n_{sn}$  of dry snow, a number of formulas [25] have been proposed,

leading, as the analysis has shown, to close quantitative results. One of them has a simple form for the interval  $\rho V < 0.4$ :

$$n_c = 1 + 83\rho V. \tag{6}$$

In accordance with (6), when the bulk density of snow changes in its characteristic interval  $\rho V = 0.2...0.4$ , the refractive index  $n_{sn} = 1.166...1.332$ . Consequently, the refractive index of the interface between two layers of snow with their bulk densities of 0.2 and 0.4 will be  $n = 1.14$ . If the difference in the density of snow in the adjacent layers decreases, the refractive index of the boundary will be even lower. Thus, the above quantitative estimates show that the boundary between the layers of snow is so soft that there is an assumption of its negligible influence on the scattering.

In this regard, during the experiment, a layer of snow was placed on the surface of a layer of marble crumb with a bulk density of 0.6. The real part of the complex dielectric constant of marble is approximately twice as much as that of ice [26], therefore the boundary between snow and marble chips is tougher than between layers of snow.

Graphs of the calculated and experimental dependences of the reflectance and transmittance for a layer of snow situated at the surface of a layer of marble crumb with a thickness of 0.01 m and a layer of snow without a substrate are shown in Fig. 5. Measurements were performed at frequencies of 22.2 and 37.5 GHz using snow, the characteristics of which were given above in Table 1 and in Fig. 1.

From Fig. 5 it can be seen that the scattering properties of snow and marble crumb differ significantly, as a result of which the reflectance and

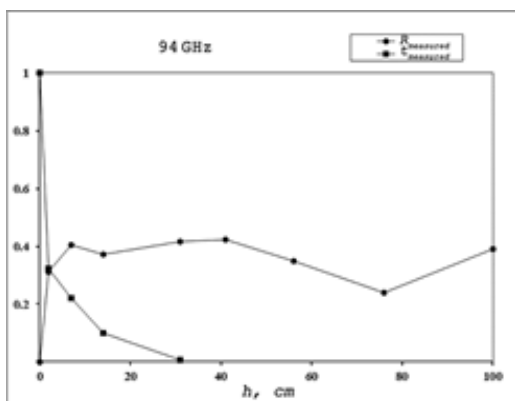
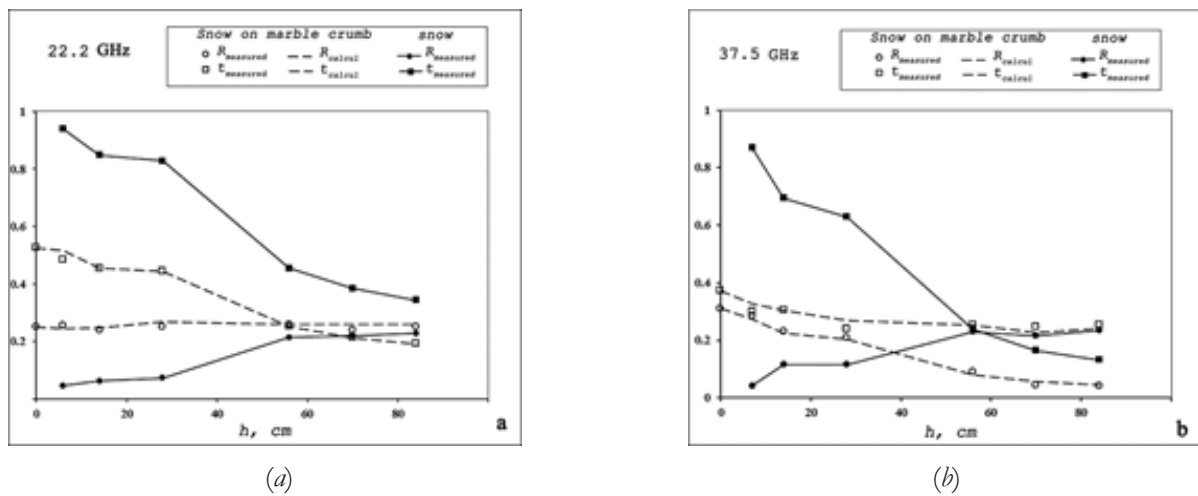


Fig. 4. The experimental values of the reflectance and transmittance of snow at a frequency of 94 GHz;



**Fig. 5.** The reflectance and transmittance at frequencies of 22.2 GHz (a) and 37.5 GHz (b) for the snow layer without a substrate and with marble crumb as substrate.

transmittance of snow change significantly when the substrate is replaced.

From the analysis of the data presented, it also follows that the calculated and measured values of the reflectance and transmittance of snow lying on the marble crumb are in satisfactory agreement with each other. The maximum discrepancies between them are observed for the reflectance at a frequency of 37.5 GHz, but do not exceed 0.03, which is consistent with the scatterplots in Fig. 2a,b.

## 7. DISCUSSION OF THE RESEARCH RESULTS

From the results of the study it follows that the influence of the boundaries of the folding snow layers is negligible. Such a conclusion, at first glance, contradicts both simple physical representations, as well as rigorous theory. Indeed, the influence of the boundaries is manifested in the fact that, when reflected at the boundaries, the fluxes of forward and backscattered radiation are attenuated, and the thermal losses increase with their multiple reflection within the layers. As a result, the reflectance and transmittance decrease the stronger, the more rigid the boundaries. In accordance with these concepts, it is extremely necessary to use formulas that take into account the influence of boundaries when calculating the resulting reflectance and transmittance of layered media.

However, this approach is valid only in theoretical terms when solving the direct problem of calculating emission from a scattering medium.

In the conducted study, the results of direct measurements of the reflectance and transmittance of individual layers of snow are used, and the values of these coefficients already contain contributions from the influence of boundaries. When layers are added, the outer boundaries of the first and last layers remain unchanged, and the influence of the inner boundaries is weakened due to a decrease in their relative refractive indices and due to absorption of reflected radiation by intermediate layers.

Approximate methods for solving the direct problem of calculating the radiation of snowpack have been proposed in [13-15]. The most thoroughly developed model is the model MMLS (Microwave Emission Model of Layered Snowpacks) [13]. This model treats snow as a set of horizontal layers. Each layer is characterized by thickness, particle correlation radius, density, liquid water content and temperature. Borders between layers are assumed to be flat. The proposed algorithm for taking into account multiple re-reflections by boundaries and re-scattering between layers is based on a six-stream model of radiative transfer, which in the case of single-layer snow is reduced to the two-stream Kubelka-Munk theory. To calculate the final result – the emissivity of a layered snowpack – a variety of approximate formulas and empirical parameters are used. Unfortunately, due to the limited amount of empirical data obtained for single-layer snow with different structures, the models developed, as shown, for example, in [27], cannot yet accurately

reproduce the brightness temperature of a real snowpack.

## 8. CONCLUSION

As a result of the study, it was shown that, first, the measured dependences of the reflectance and transmittance on the thickness of single-layer snow are satisfactorily approximated by the corresponding Kubelka-Munk theory formulas. Secondly, the discrepancies between the calculated according to Kubelka formulas and the measured values of reflectance and transmittance of two-, three- and four-layered snow practically do not go beyond the limits of coarse measurement error.

The results obtained in this work and in previous works with the participation of the author [21–23] suggest that in order to predict the intensity of dry snow cover radiation, it is enough to create a bank of experimental values of the absorption and scattering coefficients for a sufficiently wide range snow structure parameters using the two-stream Kubelka-Munk theory.

## REFERENCES

1. Shifrin KS. *Rasseyaniye sveta v mutnoy srede* [Light scattering in a turbid environment]. Moscow-Leningrad, Gostekhizdat Publ., 1951, 288 p.
2. Rosenberg GW. Absorbtsionnaya spektroskopiya dispergirovannykh veshchestv [Absorption spectroscopy of dispersed substances]. *UFN*, 1959, 69(1):57-104 (in Russ.).
3. Ambartsumian VA. Novyy sposob rascheta rasseyaniya sveta v mutnoy srede [A new way to calculate light scattering in a turbid environment]. *Izv. Academy of Sciences of the USSR, ser. geogr. and geophysics.*, 1942, 3:97-103 (in Russ.).
4. Chandrasekar S. *Radiative transfer*. Dover Public., 1960, 393 p.
5. Sobolev BB. *Perenos luchistoy energii v atmosferakh zvezd i planet* [Light Scattering in the Atmospheres of the Planets]. Moscow, Gostekhizdat Publ., 1956, 391 p.
6. Zinchenko NS., Usikov AJ. Otrazhenie radiovoln millimetrovogo diapazona ot sloya snega [The reflection of the radio waves of millimeter range from the snow layer]. *Izv. vuzov. Radiofizika*, 1960, 3(4):614-618.
7. Barabanenkov YuN. Mnogokratnoe rasseyaniye voln na ansamble chastits i teoriya perenosa izlucheniya [Multiple scattering of waves by ensemble of particles and the theory of radiation transport]. *UFN*, 1975, 117 (1):49-78 (in Russ.).
8. Kubelka P, Munk F. Ein beitrag zur optic der farbansstriche. *Z. Tech. Phys.*, 1931, 11a:593-601.
9. Isimaru A. *Wave propagation and scattering in random media: Single scattering and transport theory*. New York, Academic Press, 1978, 280 p.
10. Roy A, Ramasubramaniam R., Gaonkar HA. Empirical relationship between Kubelka–Munk and radiative transfer coefficients for extracting optical parameters of tissues in diffusive and nondiffusive regimes. *J. of Biomedical Optics*, 2012, 17 (11):115006.1-115006.6.
11. Mudgett PS, Richards LW. Multiple scattering calculations for technology. *J. Appl. optics.*, 1971, 10 (7):1485-1502.
12. Thennadil SN. Relationship between the Kubelka–Munk scattering and radiative transfer coefficients. *J. Opt. Soc. Am. A*, 2008, 25 (7):1480-1485.
13. Wiesman A, Mätzler C. Microwave emission model of layered snowpacks. *Rem. Sens. of Environ.*, 1999, 70 (3):307-316.
14. Pulliainen JT, Grandell J, Hallikainen MT. HUT snow emission model and its applicability to snow water equivalent retrieval. *IEEE Trans. on Geosci. Remote Sens.*, 1999, GE-37 (3):1378-1390.
15. Löwe H, Picard G. Microwave scattering coefficient of snow in the MEMLS and DMRT-ML revisited: the relevance of sticky hard spheres and tomography-based estimates of stickiness. *The Cryosphere*, 2015, 9:2101-2117.
16. Orchard SE. Reflection and transmission of light by diffusing suspensions. *J. Optic. Soc. Am.*, 1969, 59(12):1584-1597.
17. Kubelka P. New contributions to the optics of intensely light-scattering materials. Part I. *J. Opt. Soc. Am.*, 1948, 38(5):448-457.
18. Kubelka P. New contributions to the optics of intensely light-scattering materials. Part II. *J. Opt. Soc. Am.*, 1954, 44 (4):330-335.

19. Golunov VA, Barabanenkov YuN. Radiometric methods of measurement of the total reflectivity, the total transmissivity and the coherent transmissivity of a weakly absorbing random discrete medium layer in the millimeter wavelengths range. *Proc. Progress In Electromagnetics Research Symp. (PIERS-2012)*, Moscow, Russia, August 19-23, 2012, p.1415.
20. Golunov VA. Laboratornaya metodika eksperimentalnogo issledovaniya zakonomernostey mikrovolnovogo teplovogo izlycheniya sukhogo snezhnogo pokrova [Laboratory method of experimental study of the regularities of microwave thermal radiation of dry snow cover]. *Zhurnal radioelektroniki [online journal]*, 2018, 10. Availabel: <http://jre.cplire.ru/jre/oct18/15/text.pdf> (in Russ.).
21. Golunov VA, Kuz'min AV, Skulachev DP, Khokhlov GI. Experimental results on the frequency dependence of attenuation, scattering, and absorption of millimeter waves in a dry snow cover. *J. of Communications Technology and Electronics*, 2017, 62(9): 951–959.
22. Golunov VA, Khokhlov GI. Pokazatel stepeni chastotnoy zavisimosti intensivnosti obratnogo rasseyaniya mikrovolnovogo izlucheniya v sukhom snege i iskusstvennykh snegopodobnykh sredakh [The exponent of the frequency dependence of microwave backscattering from dry snow and artificial snow-like media]. *Zhurnal radioelektroniki [online journal]*, 2017, 9. Availabel: <http://jre.cplire.ru/jre/sep17/6/text.pdf> (in Russ.).
23. Golunov VA, Marechek SV, Khokhlov GI. Osobennosti rasseyaniya mikrovolnovogo izlucheniya v sukhom pushistom snege [Features of the microwave radiation scattering in dry fluffy snow]. *Zhurnal radioelektroniki [online journal]*, 2018, 6. Availabel: <http://jre.cplire.ru/jre/jun18/2/text.pdf> (in Russ.).
24. Golunov VA. Coherent attenuation of electromagnetic waves by weakly absorbing dense random discrete (snow-like) media. *J. Communications Technology and Electronics*, 2015, 60(1):31-37.
25. Golunov VA, Korotkov VA, Sukhonin EB. Effekty rasseyaniya pri izluchenii millimetrovykh voln atmosferoy i snezhnym pokrovom [Scattering effects under the millimeter wave emission from atmosphere and snow cover]. *VINITI Publ. Ser. Itogi Nauki i Tekhn. Radiotekhnika*, Moscow, 1990, 41:68-136.
26. Shuvaev AN., Genze YeS. Dielektricheskaya i elektricheskaya pronitsaemost gruntov naryshennoy struktury [The dielectric and electrical permeability of the soil of the damaged structure]. *Vestnik TGASU*, 2011, 1:200-206 (in Russ.).
27. Tedesco M, Kim EJ. Intercomparison of electromagnetic models for passive microwave remote sensing of snow. *IEEE Trans. Geosci. Remote Sens.*, 2006, 44(10):2654-2666.

## SEASONAL VARIATIONS OF VEGETATION COVER SCATTERING PROPERTIES

Liudmila N. Zakharova, Alexander I. Zakharov

Kotelnikov Institute of Radioengineering and Electronics of RAS, Fryazino branch, <http://fire.relarn.ru>  
Fryazino 141190, Moscow Region, Russian Federation

[zakharova@ire.rssi.ru](mailto:zakharova@ire.rssi.ru), [aizakhar@ire.rssi.ru](mailto:aizakhar@ire.rssi.ru)

*Abstract.* In our paper Transbaikalian test sites were used to demonstrate the dependence of the vegetation covers radiophysical properties from environmental conditions, and air temperature first of all. The data of Japanese spaceborne polarimetric radar PALSAR acquired at various combinations of signal polarization on receive/transmit over several years were used to measure scattering properties of underlying covers at 8 test sites and to estimate input of various scattering mechanisms in radar signal backscatter. It was discovered that at low negative temperatures in winter the normalized radar cross-section level of vegetation covers decreases rapidly for all the signal polarization combinations. The greatest fall, up to 12 dB, is observed at cross polarization, and it is about 7-8 dB for copolarized signals. Polarimetric decomposition of scattering matrix shows the specificity of the scattering mechanisms temporal behavior depending on the air temperature. If surface scattering with low entropy is typical for vegetation-free soils all the year around, the dipole scattering mechanism of forests in summer is almost completely replaced by the class of surface scattering with moderate entropy in winter. Such a specificity of annual behavior of the sounding media scattering properties may affect the efficiency of automated methods of the underlying covers classification and an accuracy of their biophysical characteristics measurements.

*Keywords:* synthetic aperture radar, normalized radar cross-section, polarimetric decompositions, vegetation classification

UDC 528.8.044.2, 537.871.5

*Bibliography* - 13 references

Received 02.04.2019, accepted 17.04.2019

*RENSIT*, 2019, 11(1):49-56

DOI: 10.17725/rensit.2019.11.049

### CONTENTS

INTRODUCTION (49)

TEST SITES (50)

THE VALUES OF THE AREA OF SCATTERING WITH DIFFERENT COMBINATIONS OF POLARIZATION ON THE RADIATION/RECEPTION (50)

POLARIMETRIC CLASSIFICATIONS AND THEIR DYNAMICS DURING THE YEAR (52)

CONCLUSION (55)

LITERATURE (55)

### 1. INTRODUCTION

Space radar imagery of the Earth provides unique information about the state of the planet, its biological diversity, natural resources and the environmental situation in the survey area. Vegetation covers, one of the most important elements of the biosphere, are given special attention when choosing the parameters of a space synthetic aperture radar (PCA) at the

stage of making a decision on the creation of this device, and also later on when planning and conducting radar measurements. The generally accepted potential for radar observations is the classification of vegetation types, the height and age of trees, the volume of plant biomass, the boundaries of forests and their condition.

A traditionally used parameter in solving thematic problems of mapping forest cover is such a radiophysical scattering parameter, as the specific effective area of backscattering of the surface (WEPR). The connection of the EPR with direct land measurements of forest characteristics using regression analysis gives good results and is most effective for coniferous forests [1, 2]. Increasing measurement channels increases the efficiency of solving forest mapping problems. These are the use of time series of observations

[3, 4], multi-frequency measurements [5-7], interferometric [8] and polarimetric [9] surveys, as well as their combinations, for example, polarimetric interferometry [10, 11]. Polarimetric imaging turns out to be especially informative due to the use of polarimetric decomposition methods [12, 13], which make it possible to isolate the contribution of different scattering mechanisms in the reflected signal. Radiophysical properties of vegetation cover significantly depend on the conditions of measurement, such as weather, environmental temperature. In [4], variations in the reflective properties of forests were studied at different polarizations of the probe signal.

The purpose of this work is to study variations in the reflective properties of the forests of Transbaikalia, first of all, the mechanisms of their dispersion depending on the season of the year.

## 2. TEST PLOTS

Test plots are located in the Selenga river delta in the territory of Transbaikalia. To assess the dynamics of the values of the specific effective area of scattering, 8 relatively homogeneous surface areas of a small area from 0.3 to 1 km<sup>2</sup> were selected (Table). Three of them are located in the forest area: two are flat (in Fig. 1 denoted by 1 - mostly coniferous near the village of Dubinino and 2 - mixed near the village of Istomin), and also section 3 on the forested ridge of the Khamar-Daban ridge (the most common - Fir, cedar). Two more sites are located between the arms of the Selenga delta: 4 interspersed with bushes and 5 covered only with grassy vegetation, and, moreover, two agricultural fields 6 and 7, as

well as a meadow site 8 in the area of the former irrigation system.

The measurements were carried out on 13 polarimetric sessions received by the PALSAR L-band radar in 2006–2008, in different months of the year and under different weather conditions.

## 3. VEHICLES OF WEPR AT DIFFERENT POLARIZATION COMBINATIONS FOR RADIATION / RECEPTION

In the transition to negative temperatures, the value of EPRS forests in the L-range can be reduced by up to 3 dB compared with the warmer period [4]. This circumstance is associated with a change in the value of the dielectric constant of the surface under different weather conditions. For this series of radar images, a comparison was made of the average values of WEPR of three forest areas, the results of which are shown in Fig. one.

For all three combinations of polarizations on radiation and reception on all forest test sites, there are two distinct minima that correspond to frosty dates of November 30, 2006 and November 16, 2007. The fallout of the EPRS is most pronounced in cross-polarization, where the oscillation magnitude reaches 12 dB, whereas in the graphs for consistent polarizations the maximum oscillation does not exceed 7-8 dB.

It should also be noted that for forest in the mountains, the EPRS values are almost always less than on the lowlands, this is especially noticeable for horizontal polarization. On coordinated polarizations, the UEPD schedule for a mountain forest area, moreover, is a monotonous decline from June-July to November, unlike the graphs for lowland

Таблица

Тестовые участки

№	Расположение и обозначение	Площадь, км <sup>2</sup>	Растительность
1	вблизи с. Дубинино (лес Д)	1	хвойный лес (сосна, ель)
2	вблизи с. Истомино (лес И)	1	смешанный лес (береза, осина, сосна, ель)
3	в горах (Хамар-Дабан)	1	хвойный лес (пихта)
4	в дельте Селенги (Дельта1)	0.6	кустарник фрагментарно
5	в дельте Селенги (Дельта2)	0.3	травянистая
6	вблизи с. Дубинино (поле Д)	0.5	поле
7	вблизи с. Истомино (поле И)	0.8	поле
8	вблизи с. Истомино (луг)	1	луг

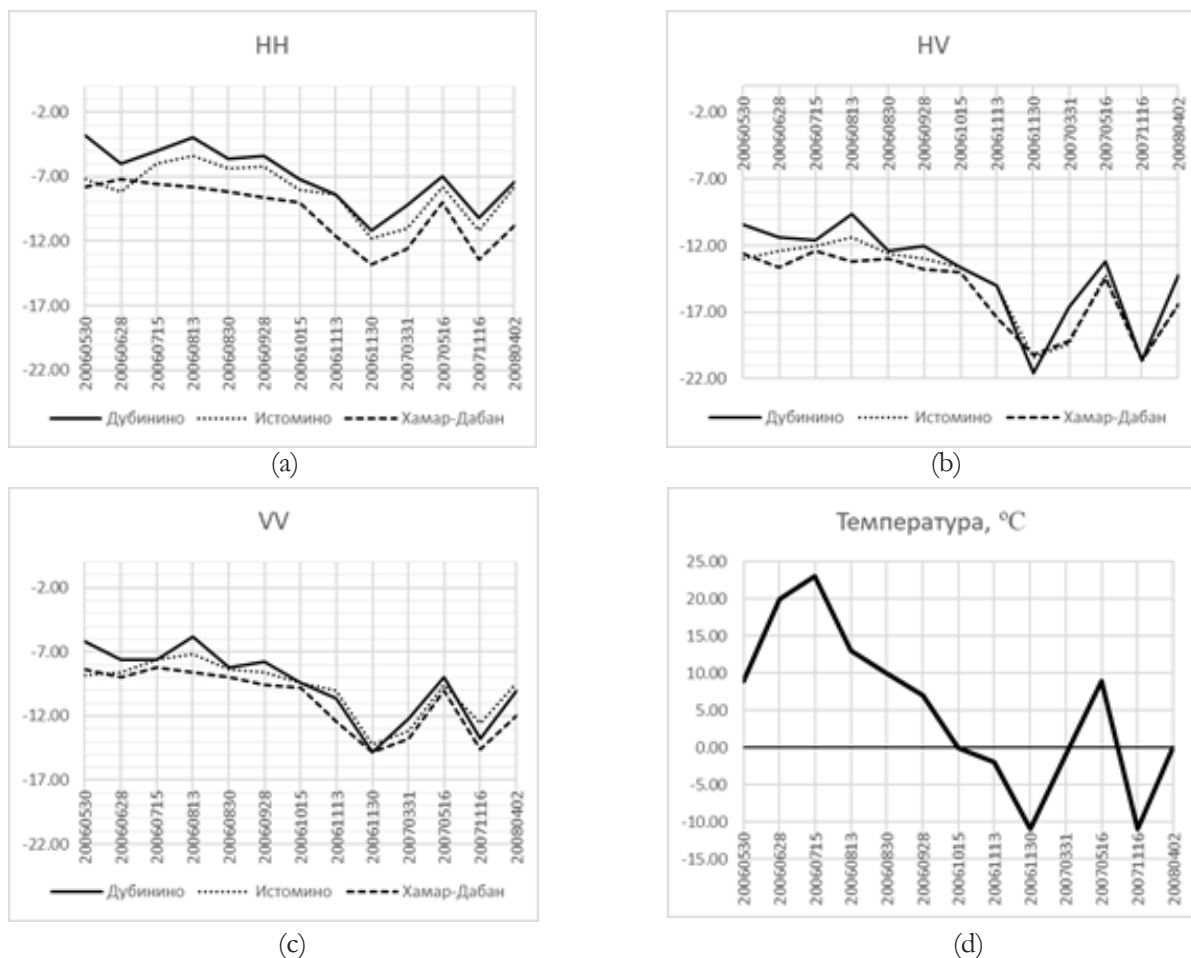


Рис. 1. Средняя УЭПР (дБ) лесных участков для разных сочетаний поляризации на излучении/приеме (a – HH, b – HV, c – VV) и температура воздуха в дни съемки (d).

forests, which are a series of local minima and maxima. The reaction to the transition of temperature through zero is more pronounced for mountain forests: whereas lowland forests show between October 15 and November 13, 2006 (temperatures of 0 ° C and –2 ° C, respectively) the EPRS decrease by only 0.4–1.4 dB, forest on the mountain slope reacts with a decline of 2.6 ° C on the agreed polarizations and 3.4°C on the cross.

The Pearson correlation coefficient in CEE in dB with the temperature graph on the survey days is quite large: the minimum value is 0.78 (Istominsk forest, HH polarization), the maximum value is 0.91 (forest in the mountains, HH polarization). Air temperature affects the reflective properties of trees indirectly, changing the moisture content of wood and, consequently, the dielectric constant. In addition to frost on the day of shooting, the nature of the weather on previous days is important: it determines the degree of drying, cooling and

possible freezing of the bark of the trees and their internal layers. In the L-band, a part of the signal is also reflected from the soil, penetrating under the vegetation cover, so it is advisable to discuss the dynamics of the UEPR of areas not covered by forest, in order to analyze the soil contribution to the backscatter coefficient on forests later.

Another observation that can be made on the basis of the time series of UEPR forest according to fig. 1 - for VV polarization, the differences between all three graphs are minimal.

The first, than even at a cursory glance, the graphs for forests (Fig. 1) and open surfaces (Fig. 2) differ - a more noticeable scatter of values on each date: the UEPR of forest areas differ by no more than 4 dB, while the difference between open areas up to 14 dB. In addition, the minimums on frosty dates are not distinguished so brightly: the summer-winter fluctuations of 5-7 dB are clearly visible on the last four dates on all graphs where the summer and winter

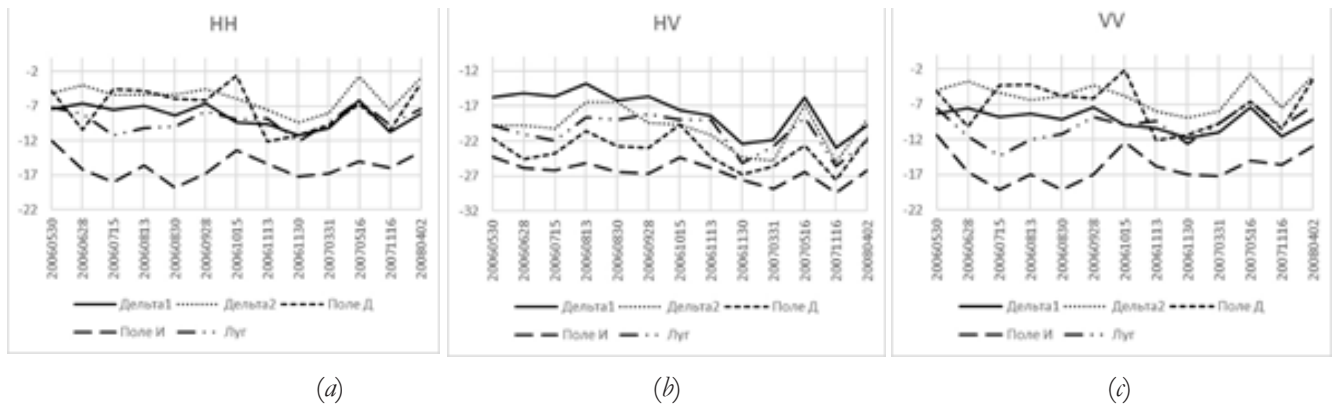


Рис. 2. Средняя УЭПР (дБ) участков, свободных от леса поляризации: (а) HH, (б) HV, (с) VV.

dates occur alternately, but the decrease in VEPR between a relatively frosty day November 30, 2016 ( $-11^{\circ}\text{C}$ ) and adjacent moderately cold days with air temperatures of  $-2^{\circ}\text{C}$  and  $0^{\circ}\text{C}$  are not visible for all sites. In general, the correlation with the temperature graph is much smaller: with the exception of the Delta-1 section, which is partially covered with shrubs, the Pearson coefficient takes values from 0.2 to 0.6, and is negative for some sections on the agreed polarizations. In the Delta-1 section, the correlation is 0.8–0.86 - almost within the same limits as in the forest areas (0.78–0.92).

The most chaotic of all five treeless areas are two fields. The reason for this is that the backscattering coefficient for these areas responds not so much to the weather, but to the work on the cultivation and harvesting carried out in the fields. Three uncultivated plots are less susceptible to drastic changes in the level of UEPR and generally behave more consistently with each other. The gradual reduction of the EPR from August to November 2006, pronounced on all forest plots, on treeless plots is completely absent

on both agreed polarizations, but to a certain extent it manifests itself on the cross. The largest difference between the backscattering coefficients of the three uncultivated areas appears on the vertical polarization (up to 10 dB, Fig. 2c), as opposed to forests, where the variability on this polarization is, on the contrary, the smallest (not exceeding 2.8 dB, Fig. 1c).

#### 4. POLARIMETRIC CLASSIFICATIONS AND THEIR DYNAMICS DURING THE YEAR

Measurement of the complete scattering matrix makes it possible to estimate the contributions of various signal scattering mechanisms by the underlying surface. In fig. Figure 3 shows the contribution values (in percent) for three mechanisms: the surface, volume, and double-reflection mechanisms, calculated using the signal decomposition method proposed by Freeman [13]. The total power of the scattering matrix

$$S = \begin{bmatrix} S_{HH} & S_{HV} \\ S_{VH} & S_{VV} \end{bmatrix},$$



Рис. 3. Вклады механизмов рассеяния для лесного участка (а), открытого участка с присутствием кустарника (б), участка на поле (с).

calculated by the formula

$P = |SHH| + 2|SHV| + 2|SVV|$ ,  
 in this method is decomposed into three components

$$P = P_s + P_v + P_d,$$

where the indices s, v and d denote the mechanisms of surface scattering, volume, and double reflection, respectively.

Volumetric scattering at a site in the Dubininsky forest (Fig. 3a) dominates almost everywhere, except for frost dates. Graphs for the two other forests look similar in the same way: everywhere except for frost days, the contribution of volume scattering is maximum (30–47%), followed by surface scattering, and the third most important scattering mechanism is double repetition. In this case, the latter should not be neglected, its contribution is 15-20% of the total power. On frosty dates, surface scattering comes to the fore, its contribution exceeds 50% due to a decrease in the contribution of the other two mechanisms.

In open areas, the surface scattering mechanism prevails on all survey dates (Fig. 3b and 3c). The share of double reflections is reduced compared to forest areas (3-16% in the Delta-1 section, where shrub vegetation is found, and 1-6% in the field). The proportion of volume scattering is intermediate between surface scattering deposits and on open surfaces for all shooting dates. At the same time, in the section with the presence of a shrub (Delta-1), the contribution of volume scattering is comparable to the contribution of surface scattering (24-42% and 40-69%, respectively), and in the field the contribution of volume scattering is almost five times less than the contribution of the surface mechanism (8-22% and 70-90%).

An alternative method for the classification of polarimetric data by scattering mechanisms is the method of polarimetric decomposition of Sh.R. Kluda and E. Pote [12], based on a spectral analysis of the coherence matrix. This method estimates the scatter of the weighted eigenvalues  $p_i$  of the coherence matrix, denoted by the entropy H:

$$H = -\sum_{i=1}^3 p_i \log_3 p_i, \quad p_i = \frac{\lambda_i}{\lambda_1 + \lambda_2 + \lambda_3}.$$

The second important parameter in this method is the angle  $\alpha$ , calculated as the weighted average of the angles  $\alpha_1, \alpha_2$  and  $\alpha_3$ , obtained by parameterizing the first coordinate of the eigenvectors of the coherence matrix in the form of  $\cos\alpha_i$ . Weights are chosen equal to  $p_i$ :

$$\alpha = \sum_{i=1}^3 p_i \alpha_i.$$

Unlike the previous method, which for a certain area on the surface determines the contribution share of the three mechanisms, the Cloud-Pete method reveals the main scattering mechanism, which can be one of eight types. Types are allocated in accordance with the values of the parametric angle  $\alpha$  and the entropy H of the eigenvalues of the coherence matrix. The values of  $\alpha$  from 0 ° to 40 ° - 42 ° correspond to the surface type of scattering, from 40 ° - 42 ° to 50 ° - 55 ° - to dipole scattering, above 55 ° - to two-fold rereflection. Surface scattering is divided into two types, with high and moderate entropy, which on the ground, as a rule, reflects the level of small-scale roughness of the reflecting surface. Dipole scattering, corresponding to Freeman's volume scattering, is divided into three types (with low, moderate, and high entropy). Similarly, the mechanism of double scattering is divided into three types according to the level of entropy.

In fig. 4 shows the dynamics of the angle  $\alpha$  for all days of surveys and all eight sections. The horizontal dotted lines indicate the levels of 40 ° and 55 °. The graphs of the three forest areas designated, as before, by the names of Dubinino, Istomino and Khamar-Daban, are located between these two levels, with

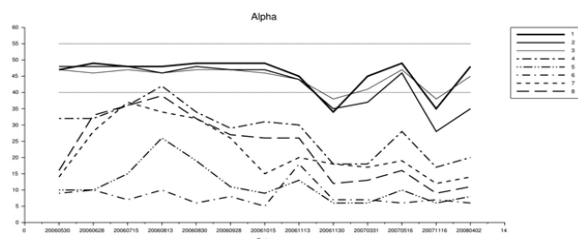


Рис. 4. Значения угла  $\alpha$  для восьми тестовых участков.

the exception of two frost dates and (for the Istomin forest) days with near-zero temperature on March 31, 2007 and April 2, 2008. Plots of forest-free plots are located entirely in the surface scattering zone, with the exception of one point: date 20060813, Delta-1 section, which has a certain amount of shrubbery and which, for this reason and under the previously considered classification methods, was close to the transitional variant between forest and field.

The entropy values are shown in Fig. 5. Forest areas have the highest entropy, which, however, for any date does not exceed the threshold value of 0.9, delimiting the types of surface scattering with moderate and high entropy. On frosty dates, the forest entropy decreases, remaining within the range of moderate values (between 0.5 and 0.9). In the range below 0.5 (low entropy) there are two graphs entirely: for the Delta-2 and Pole D. sections. Almost entirely in the zone of moderate entropy is the schedule for the Delta-1 section, the entropy on it falls below the value of 0.5 only on frost dates, in the first half of spring (March 2007 and April 2008). The values of entropy at the end of spring for this site (May 2006 and May 2007) are close to summer values. The remaining treeless plots have low entropy in the spring and winter dates and moderate in the summer and autumn. It should be noted that the values of the two parameters  $H$  and  $\alpha$  in this method of polarimetric classification for the L-range correlate to a significant degree with each other in the case of shooting natural coverings, for which the effect of double reflection is the least significant of all scattering mechanisms.

The combination of the values of  $H$  and  $\alpha$  allows each element of the image to be assigned to one of eight classes. Since fig. 4 and 5, we

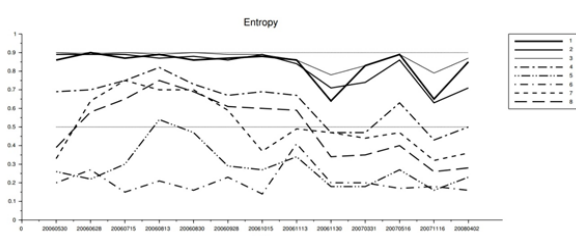


Рис. 5. Значения энтропии для восьми тестовых участков.

see that some graphs cross the threshold lines, which means that on dates with different weather conditions the classifier will work differently. An example of classification cards is shown in Fig. 6. On the left is the result of the polarimetric classification of data obtained on June 28, 2006 (air temperature + 20 ° C), on the right for data obtained on November 16, 2007 (air temperature -11 ° C). The test areas are highlighted by rectangular contours: a white contour on the forest (in the graphs of Fig. 1, 3-5 marked "Dubinino", "Les D"), a black contour in the field (in the graphs of Fig. 2-5 marked "field D").

Fragments of the field on both maps of the classification of fig. 6 belong to the same class - low entropy surface scattering. In contrast, a forest fragment with a predominantly dipole type of scattering on the summer frame (light background, crossed by slightly darker roads, with occasional patches of white dots marking a double reflection), in winter almost completely goes into another class: the main color becomes gray, to surface scattering with moderate entropy. As can be seen in fig. 6, with the whole forest, except for rare point blotches, the same thing happens as with the selected fragment: the almost complete disappearance of the dipole type of scattering and the complete - double rereflection. Treeless territories occupying the left parts of both images in Fig. 6, in the winter, they switch to the class of surface scattering

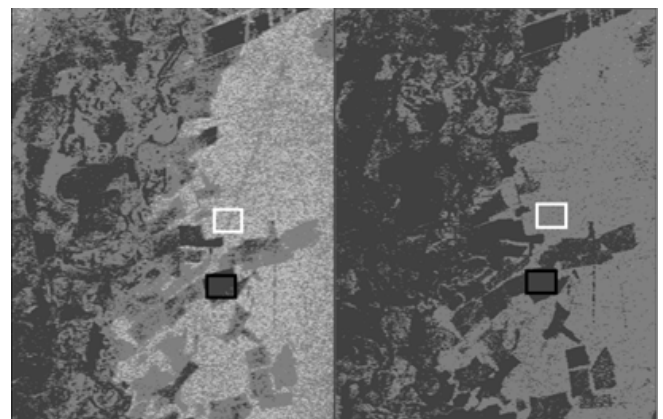


Рис. 6. Результаты летней (а) и зимней (б) классификации окрестностей Дубининского леса по методу Клауда-Потье. Белый цвет: двойное переотражение, светло-серый: дипольное рассеяние, серый: поверхностное рассеяние с умеренной энтропией, темно-серый: поверхностное рассеяние с низкой энтропией.

with the lowest entropy (the darkest shade of gray).

Thus, the classification according to the Cloud-Pete method on each date separately does not allow the forest massif to be contoured correctly (in the summer frame, in addition to the forest itself, a fragment of the river delta with shrub vegetation in the upper left corner of Figure 6a falls into In winter, besides the forest, a large number of open spaces belong to the same type of surface scattering with moderate entropy as the forest - Fig. 6b). However, the combination of two classification cards in warm and frosty weather gives the desired result: treeless surfaces - those on both classification cards are surface scattering, forest - in summer, a dipole type or double reflection, in winter - a dipole type of scattering or surface with moderate entropy.

## 5. CONCLUSION

The radiophysical properties of such natural land coverings as boreal forests depend substantially on the conditions of the measurements, primarily on the air temperature. In the cold season, UEPR of plant cover decreases sharply when working with PCA on all combinations of signal polarizations at the reception and transmission. The most dramatic fall in the UEPR is in cross polarization, where the oscillation magnitude reaches 12 dB, whereas in the graphs for consistent polarizations the maximum change does not exceed 7–8 dB. The use of data decomposition methods of polarimetric surveys carried out in different seasons of the year, allows us to identify differences in the behavior of the mechanisms of dispersion of open soils and vegetation. If open soil is characterized by low entropy surface scattering throughout the year, then the forest mainly has a dipole type of scattering recorded in summer, on winter surveys it almost completely changes to another class: the surface scattering class with moderate entropy. These features of changes in the radiophysical properties of probed media during the year affect the efficiency of automated methods for

the classification of the underlying covers and the accuracy of measuring their structural and biophysical characteristics. At the same time, a joint analysis of data obtained in the cold and warm seasons improves the quality of the classification of the types of underlying covers.

## REFERENCES

1. Le Toan T, Beaudoin A, Riou J, and Guyon D. Relating forest biomass data. *IEEE Trans. on Geosci. and Remote Sensing*, 1992, 30 (2): 403-411.
2. Dobson MC, Ulaby FT, Le Toan T, Beaudoin A, Kasischke ES, Christensen N. Dependence of the radar backscatter on coniferous forest biomass. *IEEE Trans. on Geosci. and Remote Sensing*, 1992, 30 (2): 412-415.
3. Kurvonen L, Pulliainen J, and Hallikainen M. Retrieval of Biomass in Boreal Forests from Multitemporal ERS-1 and JERS-1 SAR Images. *IEEE Trans. on Geosci. and Remote Sensing*, 1999, 37 (1): 198-205.
4. Kwok R, Rignot EJM., Way J, Freeman A, and Holt J. Polarization Signals of Frozen & Thawed Forests of Varying Environmental State. *IEEE Trans. on Geosci. and Remote Sensing*, 1994, 32 (2): 371-381.
5. Ranson KJ, Sun G. Northern forest mapping biomass of a forest using multifrequency SAR data. *IEEE Trans. on Geosci. and Remote Sensing*, 1994, 32 (2): 388-396.
6. Pulliainen JT, Heiska K, Hyyppä J, Hallikainen MT. Backscattering properties of boreal forests at the C- and X-bands. *IEEE Trans. on Geosci. and Remote Sensing*, 1994, 32 (5): 1041-1050.
7. Armand NA, Zakharov AI, Kucheryavenkova IL. The study of the reflective characteristics of forests in the Moscow region according to the SIR-C XRD data. *Radio Engineering*, 1998, 9: 27-31.
8. Pulliainen JM, Hallikainen M.M. *Remote Sensing of Environment*, 2003, 85 (4): 397-409.
9. Wollersheim M, Collins MJ, Leckie D. Estimating boreal forest radar. *Intl J. of Remote Sensing*, 2011, 32 (9): 2481-2505.

10. Cloude SR, Papathanassiou KP. Polarimetric SAR Interferometry. *IEEE Trans. on Geosci. and Remote Sensing*, 1998, 36 (5): 1551-1565.
11. Mette T, Papathanassiou KP, Hajnsek I, Zimmermann R. Forest Biomass Estimation using Polarimetric SAR Interferometry. *Proc. of intl. Geosci. And Remote Sensing Symp. (Toronto, Canada, June 24-28, 2002)*, pp. 3859-3862.
12. Cloude SR and Pottier E. An Entropy Based Classification Scheme for Land Applications of Polarimetric SAR. *IEEE Trans. on Geosci. and Remote Sensing*, 1997, 35 (1): 68-78.
13. Freeman A and Durden SL. A Three-Component Scattering Model for Polarimetric SAR Data, *IEEE Trans. on Geosci. and Remote Sensing*, 1998, 36 (3): 963-973.

## THE SCINTILLATION MODELS FOR SIGNAL PROPAGATION THROUGH SATELLITE IONOSPHERIC CHANNELS

Lev E. Nazarov, Dmitry V. Antonov, Vitaly V. Batanov, Andrey S. Zudilin, Vladimir M. Smirnov

Kotelnikov Institute of Radioengineering and Electronics of RAS, Fryazino Branch, <http://fire.relarn.ru>  
Fryazino 141190, Moscow Region, Russian Federation

[levnaz2018@mail.ru](mailto:levnaz2018@mail.ru), [dmitry.vl.antonov@gmail.com](mailto:dmitry.vl.antonov@gmail.com), [bvitaly@inbox.ru](mailto:bvitaly@inbox.ru), [zudilinas@hotmail.ru](mailto:zudilinas@hotmail.ru), [vsmirnov@sunclass.ire.rssi.ru](mailto:vsmirnov@sunclass.ire.rssi.ru)

*Abstract.* The results of analysis for signals propagating through the ionosphere satellite communication channels with temporal and spatial electron density irregularities in the ionosphere plasma are presented in the article. These electron density irregularities most commonly occur in low-latitude, auroral, and polar regions and refer to the random signal amplitude and phase fluctuations. Occurrence of scintillation is difficult to predict and model due to the variability of its numerous influencing factors, which include solar activities, inter-planetary magnetic field activities, local electric field and conductivity, convection processes, wave interactions. Satellite ionospheric radio waves in P-, L- frequency bands are vulnerable to scintillations that can severely impact the acquisition and tracking process in receivers, causing a degradation in navigation and in information systems (as example, Kospas-Sarsat system) solution accuracy, integrity, and continuity. The widely-used indice to measure ionospheric scintillation activity is the scintillation index for amplitude scintillation (the standard deviation of the received signal power normalized to the average signal power). The values of scintillation index (0.27...0.49) for Cospas-Sarsat channel (406.0-406.1 MHz) are evaluated in the article. The empirical model for probability density for signal amplitude as m-law Nakagami based on these values of scintillation index is used to evaluate error-performance degradation concerning to propagation through free space. The computer simulations for evaluation of these error-performance degradations are performed - the degradation of signal/noise is about 6.8 dB for bit-error 0.001.

*Keywords:* satellite ionosphere channels, signals, signal scintillations, error-performances, signals, phase shift keying signals, Kospas-Sarsat

UDC 621.391.01

*Bibliography* - 21 references

*RENSIT*, 2019, 11(1):57-64

Received 16.04.2019, accepted 21.04.2019

DOI: 10.17725/rensit.2019.11.057

### CONTENTS

1. INTRODUCTION (57)
  2. PROBLEM STATEMENT (58)
  3. SIGNAL SCINTILLATION MODELS (59)
  4. CALCULATION RESULTS (59)
  5. CONCLUSION (62)
- REFERENCES (63)

### 1. INTRODUCTION

Scintillations (fading) of signals during propagation through satellite ionospheric transmission lines are caused by random temporal and spatial fluctuations of

the electron density of ionospheric inhomogeneities [1–5].

Solving problems of signal propagation through such randomly inhomogeneous media implies establishing a connection between the statistical characteristics of the electron density field and the characteristics of the signals at the input of receiving devices [2-4, 6, 7]. A fairly wide range of works [2, 4, 8, 9] is devoted to the creation and development of private models of signal scintillation. Using these models, it is possible

to calculate the statistical characteristics of signal power variations (for example, average power, statistical power moments) and, as a result, estimate the probability characteristics when receiving signals and compare them with the probability characteristics of receiving signals when propagating in free space [10, 11]. Based on this comparison, the corresponding energy losses are estimated, which must be taken into account in the energy budgets of radio lines.

The results of experimental and theoretical studies using these models show the dependence of energy losses due to scintillation on the central frequency, on the spatial distribution of transmitting and receiving devices, solar activity, daily time [3, 4]. Radio lines of the L-frequency range, actively used by satellite systems of global navigation (Glonass, GPS, Gallileo, etc.) [12-17], have been studied in sufficient detail. The problem of the generalization, development and addition of these results for the p-frequency radio links, which are also actively used by satellite systems for transmitting information, is relevant. An example is the international satellite search and rescue system Cospas-Sarsat, operating in the frequency range 406.0 ... 406.1 MHz [18].

**2. PROBLEM STATEMENT**

In **Fig. 1** is a diagram explaining the propagation of  $s(t)$  signals over a satellite ionospheric radio link. Studies show that the main contribution to the scintillation of signals is determined by the inhomogeneities of the electron density of the ionospheric layer F, having dimensions  $l$ , comparable to the dimensions of the first Fresnel zone ( $\lambda$  is the wavelength of the signals) [1, 4, 15]. For the location of the onboard transmitter

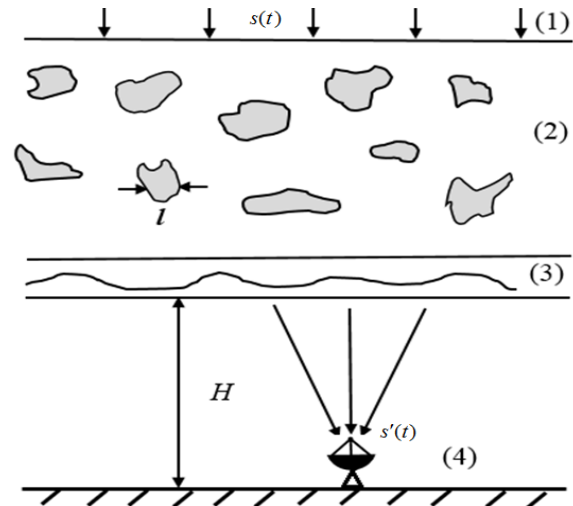


**Рис. 1.** Распространение сигналов по спутниковой ионосферной радиолинии: 1 - плоская волна; 2 - ионосферный слой неоднородностями; 3 - фазовый фронт; 4 - наземный приемный пункт.

at an altitude of  $H_0 \gg H$  ( $H = 350-400$  km - the height of the ionospheric layer F), which is a valid condition for satellite global navigation systems ( $H_0 \approx 19,200$  km), the incident signals  $s(t)$  refer to the far radiation zone and rely flat waves. In models [1, 4], the effect of ionospheric inhomogeneities is given by the action of a thin screen with a field of random phase distribution. The amplitude  $A$  of the resulting signal  $s'(t)$  at the input of the ground receiving point is a random variable and is determined by applying diffraction methods taking into account a random field [1, 3].

For the basic model of channel noise in the form of additive white Gaussian noise  $n(t)$  (ABGN), the rule of optimal reception of digital signals that implements the statistical maximum likelihood criterion is based on the calculation of the cross-correlation of the input implementation  $s'(t) + n(t)$  with the original signal  $s(t)$  [10]. In this case, the probability of erroneous reception of the  $P_b$  bit in the coherent reception of signals with two-phase and four-phase keying

(FM2 signals, FM4 signals) without error-correcting coding is determined by the relation [10]

$$P_b(E_b / N_0) = 1 - F(\sqrt{2E_b / N_0}). \quad (1)$$

Here,  $E_b$  is the signal energy per information bit;  $N_0$  is the ABGSh spectral density (one-sided);

$$F(x) = \frac{1}{\sqrt{2\pi}} \int_{-\infty}^x \exp(-t^2 / 2) dt.$$

Assuming the amplitude  $A$  of the signal  $s'(t)$  is random stationary in a broad sense of magnitude with the distribution density  $p(A)$ , the average error probability taking into account scintillation can be calculated using the expression [10]

$$P_b = \int_0^{\infty} P_b(E_b A^2 / N_0) p(A) dA. \quad (2)$$

The essence of the task is to provide descriptions of the scintillation models of the amplitudes of signals as a random process during propagation through heterogeneous satellite ionospheric radio links, to give the results of calculating the error probability for signals with phase shift keying taking into account the scintillation models and to give these signals for the P-frequency range of relation to distribution in free space.

**3. MODELS OF SIGNAL SCINTILLATION**

The considered scintillations of signals and their statistical characteristics are determined by a number of parameters — the center frequency  $f_0$ , the spatial distribution of the transmitting and receiving devices, solar activity, the speed of the ionospheric irregularities, the daily time, etc. [3, 4].

When creating and developing signals scintillation models taking into account these factors, two approaches are used - based on the use of analytical methods for describing the propagation of signals with ionospheric

irregularities and on the use of empirical relationships regarding the distribution density  $p(A)$  [1, 5].

In the approach based on analytical methods for describing the propagation of signals, the presence of ionospheric irregularities with small spatial variations in electron density with a scale comparable to the wavelength  $\lambda$  [1, 4] is considered. Its temporal variations with a  $1 / f_0$  scale are also considered to be small. In this case, the component of the electric field  $E$ , falling vertically on the ionospheric layer ( $x$ -axis) during propagation, is a solution of the wave equation [3, 19, 20]

$$\frac{d^2 E(x, t)}{dx^2} + k^2 \varepsilon(x, t) E(x, t) = 0. \quad (3)$$

Here  $k = 2\pi / \lambda$  is the wave number for free space,  $\varepsilon(x, t)$  is the dielectric constant of the medium.

Further, it is assumed that the main variations in the dielectric constant  $\delta\varepsilon(x, t) \approx 4\pi re N_e / k^2$  occur in a limited volume with linear dimensions  $l$  (Fig. 1), comparable to the dimensions of the first Fresnel zone  $r_0$  ( $re$  is the electron radius). Under this condition, equation (3) is transformed into a parabolic equation [1, 3]

$$-j2k \frac{\partial U}{\partial x} + \nabla_1^2 U + k^2 \varepsilon(x, t) U = 0. \quad (4)$$

Here

$$u = U \exp(-jkx), \quad \nabla_1^2 = \frac{\partial^2}{\partial y^2} - \frac{\partial^2}{\partial z^2}.$$

Equation (4) is stochastic, its solution determines the relationship between the random variables  $U$  and  $\varepsilon(x, t)$  and establishes their statistical characteristics (for example, statistical moments, including the fourth moment of the amplitude of the signal  $s'(t)$ , used to estimate the range of fading signals).

Equation (4) is stochastic, its solution determines the relationship between the random variables  $U$  and  $\varepsilon(x, t)$  and establishes their statistical characteristics (for example, statistical moments, including the fourth moment of the amplitude of the signal  $s'(t)$ , used to estimate the range of fading signals).

Equation (4) is non-linear, the problem of finding its solution in the form of closed analytical expressions remains open. Its approximate solutions of Born and Rytov are known as the sum of terms depending on the small parameter  $\varepsilon'(x, t) \ll 1$ , where  $\varepsilon(x, t) = 1 + \varepsilon'(x, t)$  [1, 6, 7]. For the approximation  $\varepsilon'(x, t) = 0$ , the solution (4) in the form of  $U_0(x, t)$  determines the propagation of signals in free space. The use of the term depending on  $\varepsilon'(x, t)$  gives the Born approximation  $U'(x, t)$  (Debye-Born scattering) corresponding to single scattering under the condition  $U'/U_0 \ll 1$  [7]. For  $U'/U_0 \approx 1$ , solution (4) is equivalent to solving the problem with multiple scattering [7].

The Rytov approximation (small perturbation method) is based on the use of the relation  $\psi = \ln(A)$ , the function is a solution of the equation [1, 6, 7].

$$-2k \frac{\partial \psi}{\partial x} + \nabla_1^2 \psi + (\nabla_1 \psi)^2 + k^2 \varepsilon = 0. \quad (5)$$

The solution (5) in the Rytov's approximation determines the linear relationship between the random functions and the relationship of the statistical moments of the function  $\ln(A)$  to the amplitude of the signal  $s'(t)$  and the fluctuations of the electron density. At the same time, it is noted that the considered analytical approaches using approximate solutions of equation (4) do not provide sufficiently accurate results in the general

case of the  $U'/U_0$  ratio with respect to experimental measurements [1].

More accurate scintillation models from the class under consideration are based on the inclusion of a thin phase screen at the height  $H$  of the ionosphere layer  $F$  (Fig. 1) - ionospheric irregularities disturb the screen's field, using its resultant  $s'(t)$  signals using diffraction theory methods [1, 4]. Modifications of this approach include several screens with uncorrelated phase fields [1].

Scintillation models of signals from the second class associate the parameters of empirical distribution densities  $p(A)$  of the amplitude of the signal  $s'(t)$  with the scintillation index  $S_4 = (\langle I^2 \rangle - \langle I \rangle^2) / \langle I \rangle^2$ , the values of which define an important characteristic for applications - the fading range of Pf signals [5, 9]. Here  $I = A^2(t)$  is the signal power;  $\langle \rangle$  is the averaging operation over an ensemble of signals, or over time, assuming that the random process  $A(t)$  is ergodic.

The fading range of the amplitude of the Pf signals (dB) at the input of the receiving device is determined by the approximate relationship [5]. A more accurate relationship between Pf and  $S_4$  can be determined using empirical models of the distribution density  $p(A)$ , the parameters of which can be set using the analytical models considered above (4), (5) or using experimental studies of radio lines.

According to the values of the  $S_4$  index, fading is classified: weak to  $S_4 < 0.3$ ; average  $0.3 < S_4 < 0.6$ ; strong  $S_4 > 0.6$  [5]. An increase in  $S_4$  values is accompanied by an increase in energy loss with respect to propagation in free space.

For scintillations, the density  $p(A)$  can be represented by well-known distribution laws: the log-normal distribution [2], the m-distribution by Nakagami [5],

the Rayleigh-Rice distribution, the  $-\alpha-\mu$  distribution [9].

Most often, the amplitude density  $p(A)$  of signals during propagation along the ionospheric radio link is described by the Nakagami distribution [4, 5]

$$p(A) = \frac{2}{\Gamma(m)} \left(\frac{m}{\sigma^2}\right)^m A^{2m-1} \exp\left(-\frac{mA^2}{\sigma^2}\right). \quad (6)$$

Here  $\sigma^2$  is the fluctuation component of the signal power  $s'(t)$ ;  $m \geq 1/2$  is a parameter specified by the relation  $\Omega = \langle A^2 \rangle$  [21]. The parameters  $S4$  and  $m$  are related by the relation  $m = 1 / S4$  [5].

The distribution by Nakagami is approximated by the Rayleigh-Rice distribution [21]

$$p(A) = \frac{A}{\sigma^2} \exp\left(-\frac{A^2 + A_0^2}{2\sigma^2}\right) I_0\left(\frac{AA_0}{\sigma^2}\right). \quad (7)$$

Here,  $A_0$  is the average amplitude of the signal component;  $I_0(x)$  is a modified Bessel function of the first kind of zero order [21].

The Rayleigh-Rice distribution is characterized by the Rice coefficient [21]. Parameters  $S4$ ,  $m$  and the Rice coefficient  $c$  subject to the following relations

In accordance with the experimental data for the normal mid-latitude ionosphere and for the radio link with the center frequency  $f_0 = 400$  MHz, the flicker index  $S4$  does not

exceed 0.3 ... 0.5, i.e. fading can be attributed to the class of weak-medium fading, for polar regions the values of  $S4$  can reach 1 [5] and in this case fading can be attributed to the class of strong fading.

Below are the results of estimating the  $S4$  index based on experimental measurements of the amplitudes of the signals of the Cospas-Sarsat satellite system (center frequency  $f_0 = 406$  MHz) and the probability characteristics for receiving signals calculated using relation (2) and model descriptions of the amplitude distribution density  $p(A)$  (6), (7) with parameters corresponding to the estimates of  $S4$ .

#### 4. RESULTS OF CALCULATIONS

The Cospas-Sarsat international satellite system is designed to determine the location of emergency beacons operating in the P-frequency range 406.0 ... 406.1 MHz (uplink) and in the L-frequency range (downlink) [18]. Information messages of second-generation beacons are transmitted over a radio link using digital FM4 signals with an offset [10], a signal duration of 1 second with a nominal on-time interval of 30 seconds, and a sync sequence of 160 ms [18]. Relay beacon signals are located

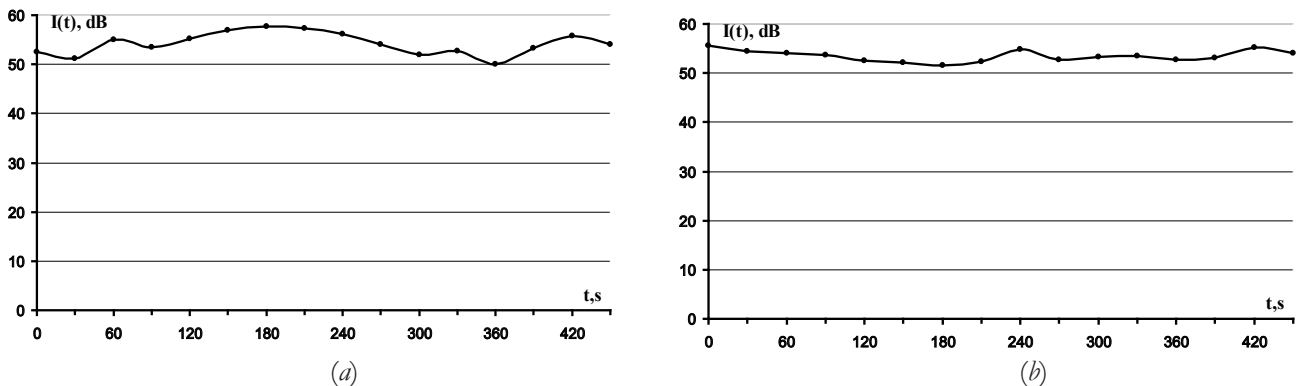


Рис. 2. Фрагменты зависимости мощности сигналов  $I(t)$  от времени, полученные путем обработки сигналов радиобуев спутниковой поиско-спасательной системы Коспас-Сарсат второго поколения (дневное время, июль 2018 г.): (а) навигационный спутник GPS; (б) навигационный спутник Galileo.

on global navigation satellites (Glonass, GPS, Galileo [17]).

In **Fig. 2** shows fragments of the dependence of the power of the I (t) signals on time, calculated by processing at FIRE them. V.A. Kotelnikov of the RAS of the received signals of the second generation beacons in the form of records in digital format, obtained using the technical means of the receiving station from the GPS mid-orbit navigation satellites (Fig. 2a), Galileo (Fig. 2b) for daytime. Beacon producing countries - France, USA, beacons operate in test mode [18].

The peculiarity of the considered radio link is the joint influence of ionospheric irregularities on the propagation of signals in the P- (uplink) and L- (downlink) frequency ranges.

During processing, point estimates I (t) were calculated for the discrete beacon turn-on time by correlation processing of input realizations with a synchronization sequence.

As a result of processing signals from the Cospas-Sarsat satellite system (time period March-October 2018), a possible range of S4 scintillation index values was determined for the frequency range under study  $S4 = 0.27 \dots 0.49$ , the approximate fading range of signals amplitude  $Pf = 5.25 \dots 11.20$  db. The corresponding values of the Nakagami distribution parameter (6) are in the range of  $m = 2.04 \dots 3.70$ , the corresponding range of values of the Rice coefficient of the Rayleigh-Rice distribution (7)  $c = 4.1 \dots 7.4$ .

In **Fig. 3** shows the probabilities of  $P_b$  error in the coherent reception of FM4 signals calculated using relations (1), (2) for the scintillation model defined by the Rayleigh-Rice amplitude distribution density (7) with the given estimates of the Rice parameter  $c$ .

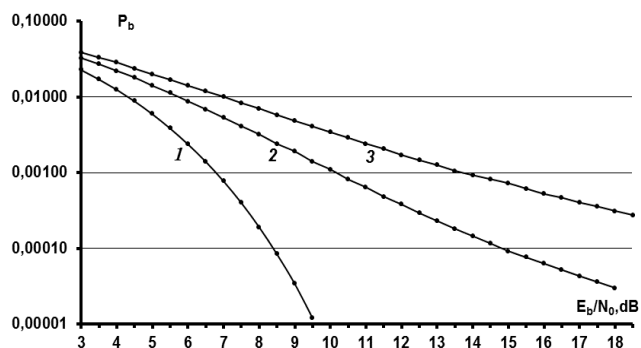


**Рис. 3.** Вероятности ошибки при когерентном приеме ФМ4 сигналов для модели сцинтилляции, задаваемой плотностью распределения Релея-Райса: 1 - распространение в свободном пространстве; 2 - параметр Райса  $c = 7.4$ ; 3 - параметр Райса  $c = 4.1$ .

Curve 1 corresponds to propagation in free space — the probability of  $P_b = 10^{-3}$  is ensured with respect to  $E_b / N_0 = 6.7$  dB.

Curve 2 corresponds to the maximum value of the Rice parameter in the range of their estimates  $c = 7.4$ , the probability  $P_b = 10^{-3}$  is ensured at the ratio  $E_b / N_0 = 10.0$  dB, the energy loss relative to curve 1 reaches 3.3 dB.

Curve 3 corresponds to the minimum value of the Rice parameter in the range of their estimates  $c = 4.1$ . It can be seen that the probability of  $10^{-3}$  is ensured with respect to  $E_b / N_0 = 13.5$  dB, which corresponds to the energy loss with respect to curve 1 to 6.8 dB.

Energy losses increase with decreasing  $P_b$  error values.

## 5. CONCLUSION

The descriptions of the models of scintillation (fading) of signals due to random temporal and spatial fluctuations of the electron density of ionospheric inhomogeneities are given. These models fall into two general classes - based on the application of analytical methods for describing signal propagation using the theory of stochastic equations and on the basis of empirical models regarding

the density distribution of signal amplitudes at the input of receivers using a scintillation index (fourth-order statistical moment of signal amplitudes).

The results of the numerical estimation of the scintillation index for the mid-latitude radio line of the Cospas-Sarsat satellite information system are given. A feature of this radio link is the joint influence of ionospheric irregularities on the propagation of signals in the P- (uplink) and L- (downlink) frequency ranges. As a result of signal processing of the Cospas-Sarsat system, a possible range of scintillation index values of 0.27 ... 0.49 was determined. Using the empirical scintillation model, we calculated the probability characteristics of receiving signals with phase shift keying distributed over the radio link under consideration with a given scintillation index range, and determined the required power margin of up to 6.8 dB for the error probability 0.001 with respect to spreading in free space. This must be taken into account when calculating the energy budget of a given radio link.

The study of the statistical characteristics of the studied radio link, in particular, the determination of the time and frequency band of coherence, as well as the specification of the range of the energy reserve, taking into account the noise-resistant coding methods, constitute the direction of prospective studies.

**REFERENCES**

1. Crane RK. Ionospheric Scintillation. Proceeding of IEEE, 1977, 2: 180-199.
2. Kolosov MA, Armand NA, Yakovlev OI. The propagation of radio waves in space communications. M., Communication, 1969, 156 p.

3. Yakovlev OI, Yakubov VP, Uryadov VP, Pavelev AG. The propagation of radio waves. M., LENAND, 2009, 496 c.
4. Rino CL. Remote Sensing. John Wiley & Sons, Hoboken, New Jersey, 2011, 244 p.
5. Satellite services and systems. Recommendation ITU-R P.531-11. Electronic Publication, Geneva, 2012, 24 p.
6. Rytov SM, Kravtsov YuA, Tatar VI. Introduction to statistical radiophysics. T. 2. Random fields. M., Science, 1978, 464 c.
7. Isimaru A. Propagation and scattering of waves in random environments. T. 2. M., Mir, 1981, 280 p.
8. Priyadarshi S. Review of Ionospheric Scintillation Models. Surveys in Geophysics, 2015. 36 (2): 295-324.
9. Moraes AO, Vani BC, Costa E, Sousasantos J, Abdu MA, Rodrigues F, Gladek YC, Oliveira BA, Monico JF. Ionospheric Scintillation Fading Coefficients for GPS L1, L2, and L5 Frequencies. Radio Science, 2018, 53: 1165-1174.
10. Sklyar B. Digital communication. Theoretical foundations and practical application. M., Ed. Williams House, 2003, 1104 p.
11. Nazarov LE, Batanov VV. Probabilistic characteristics of the detection of radio pulses during the propagation of satellite communication systems over the ionospheric transmission lines. Technology and Electronics, 2017, 62 (9): 866-874.
12. Humphreys TE, Psiaki ML, Kintner PM. Modeling the effects of ionospheric scintillation on GPS carrier phase tracking. IEEE Transactions on Aerospace and Electronic Systems, 2010, 46 (4): 1624-1637.

13. Ghafoori F, Skone S. Impact of equatorial ionospheric irregularities on GNSS receivers using real and synthetic scintillation signals. *Radio Science*, 2015, 50: 294-317.
14. Jiao Y, Morton Y, Taylor S, Pelgrum W. Characterization of high-latitude ionospheric scintillation of GPS signals. *Radio Science*, 2013, 48 (6): 698-708.
15. Jiao Y, Xu D, Morton Y, Rino CL. Equatorial scintillation amplitude fading characteristics across the GPS frequency bands. *Navigation*, 2016, 63 (3): 267-281.
16. Hofmann-Wellenhof B, Lichtenegger H, Collins J. *Global Positioning System. Theory and Practice*. Springer-Verlag, New York, 1994, 392 p.
17. GLONASS: principles of construction, functioning. M.: Radio engineering. 2010, 798 s.
18. Specification for second-generation COSPAS-SARSAT 406 MHz distress beacons. C / S T.018. Issue 1, 2016.
19. Kutuza BG, Moshkov AV, Pozhidaev VN. Combined method that eliminates the influence of the ionosphere when processing signals of P-range airborne radars with synthetic aperture. *Radio engineering and electronics*, 2015, 60 (9): 889-895.
20. Bova YI, Kryukovsky AS, Lukin DS. Propagation of frequency-modulated radiation of electromagnetic waves in the Earth's ionosphere, taking into account absorption and an external magnetic field. *Radio engineering and electronics*, 2019, 64 (1): 3-14.
21. Tikhonov VI. *Statistical radio engineering*. Moscow, Soviet Radio, 1966, 678 p.

# THE INVESTIGATION OF IONOSPHERIC CHANNEL INFLUENCES FOR PHASED SHIFT KEYING DIGITAL SIGNALS

Lev E. Nazarov, Vitaly V. Batanov

Kotelnikov Institute of Radioengineering and Electronics of RAS, Fryazino Branch, <http://fire.relarn.ru>  
Fryazino 141190, Moscow Region, Russian Federation

[nazarov@ire.rssi.ru](mailto:nazarov@ire.rssi.ru), [batanov@mail.ru](mailto:batanov@mail.ru).

*Abstract.* The results of analysis for signals propagating through the ionospheric satellite communication channels are presented in the article. As a measure of distortion estimates concerning to the free space propagating the signal/noise degradation and the detection error-performances are used. The descriptions of signal distortions due to ionospheric influence are based on the time-domain solution for ionospheric channel as linear stationary filter. The signal/noise and error-performance degradations for two-phased shift keying signals are evaluated. The computer simulations for evaluation of these error-performance degradations concerning signal/noise decreasing are performed - the degradation of signal/noise is about 2.5 dB for bit-error 0.00001.

*Keywords:* ionosphere, satellite ionospheric channel, error-performances, signals, phase shift keying signals

UDC 621.391.01

*Bibliography* - 15 references

RENSIT, 2019, 11(1):65-72

Received 26.03.2019, accepted 31.03.2019

DOI: 10.17725/rensit.2019.11.065

## CONTENTS

1. INTRODUCTION (65)
  2. PROBLEM STATEMENT (66)
  3. IONOSPHERE MODELS (67)
  4. DESCRIPTION OF DIGITAL SIGNAL DISTORTION (67)
  5. CALCULATION RESULTS (69)
  6. CONCLUSION (70)
- REFERENCES (71)

## 1. INTRODUCTION

The ionosphere is a heterogeneous dispersive propagation medium, which causes phase-frequency and amplitude-frequency distortions of digital signals during their propagation [1-4]. These distortions lead to intersymbol interference (ISI) in addition to additive channel thermal noise (AWGN) and energy losses during correlation signal processing, which is the basis of signal detection procedures during synchronization and demodulation of signals in digital

communication systems with respect to propagation in free space [5-7].

The problem of studying and quantifying the distortion of digital signals with phase shift keying with the spread of the spectrum during their propagation through ionospheric radio links for satellite communication systems and satellite navigation systems is a pressing problem [5-9]. Quantitative estimates of the distortion data are made on the basis of a comparative analysis of the probability characteristics when receiving distorted signals and undistorted signals and depend on the working frequency ranges [1, 4]. In this article, these estimates are given for the P-band radio links, which are extensively used in the development and creation of a number of satellite information systems with the expansion of the spectrum of signals for various purposes, for example, in developing the second-generation

Cospas-Sarsat international satellite search and rescue system (center frequency 406.1 MHz) [10].

## 2. PROBLEM STATEMENT

The basis of methods for analyzing the influence of the ionosphere on digital signal distortions is the solution of the wave equation during propagation along the  $z$  axis of a plane wave  $E(z, f)$  with a frequency  $f$  normally incident on a layer of inhomogeneous medium with a dielectric constant  $\varepsilon(z, f)$  [2, 6]

$$\frac{d^2 E(z, f)}{dz^2} + \frac{(2\pi)^2 f^2}{c^2} \varepsilon(z, f) E(z, f) = 0. \quad (1)$$

Here  $c$  is the speed of light in a vacuum.

Wave equation (1) determines the particular model of radio wave propagation in the direction of the Earth's magnetic field considered below. In this case, only the polarization plane of the radio waves rotates during propagation [3, 4]. An alternative model is the propagation of radio waves in a direction perpendicular to the direction of the Earth's magnetic field, which takes into account two-beam propagation (the occurrence of ordinary and extraordinary waves) and, in addition to the distortions under consideration, also fading signals (frequency-selective and non-selective frequency) [3]. This model assumes independent research.

A number of analytical solutions of equation (1) were obtained using simplifications with respect to  $\varepsilon(z, f)$ , assuming, in particular, the propagation medium is isotropic (the model of "cold" plasma), as well as flat-layered or spherically layered [2]. An important direction is the determination of approximate solutions of the wave equation (1) using these simplifications, in particular, the

approximation of geometric optics. A sufficient condition for the applicability of this approximation is the slowness of changes in the dielectric properties of the medium at wavelength  $\lambda$ , i.e. [2, 4]. In this case, the approximation of geometric optics to the solution of the wave equation without taking into account the reflection for the inhomogeneous ionosphere has the form [2]

$$E(z, t) = E(0, t) \exp\left(\frac{j2\pi f}{c} \int_0^z n(z, f) dz\right). \quad (2)$$

Here is the refractive index of the medium.

Relation (2) is valid for monochromatic waves. For digital signals with center frequency  $f_0$ , specified as [5]

$$E(0, t) = A(t) \exp(j2f_0 t) \quad (3)$$

and representing a spectrum of monochromatic waves, the task becomes more complicated. In this case, each spectral component during propagation acquires a partial phase shift and a partial change in amplitude, which causes the resulting distortion of signals at the input of the receiving device. In (3), the designation corresponds to the complex envelope of the signals defined by the signal "constellation" with the duration  $T$  of the constituent elements with phase or quadrature amplitude manipulation [5].

The essence of the task is to describe the distortions of signals during their propagation through satellite ionospheric radio links and to make an assessment of the influence of these distortions on the probabilistic characteristics when receiving signals.

## 3. MODELS OF THE IONOSPHERE

For frequencies  $f$  used in satellite communication systems ( $f > 30$  MHz [1]), the dielectric constant of the ionosphere  $\varepsilon(z, f)$  in the form of a heterogeneous spherically

symmetric medium is given by the relation [1, 3, 4]

$$\varepsilon(z, f) = 1 - f_p^2(z) / f^2. \quad (4)$$

Here is the natural frequency of the ionosphere (kHz); Ne (z) is the electron density of the ionosphere (el / cm<sup>3</sup>) at height z.

This model of the dielectric constant ε (z, f) (4) is real, the phenomena of reflection, scattering and absorption of radio waves are assumed to be small. This causes only phase-frequency distortion during signal propagation [10].

The electron density of the ionosphere Ne (z) depends on the altitude, latitude and longitude, on the time of day and solar activity. A number of papers [1–4, 11] are devoted to the development and development of its models. These models are used to solve particular problems of navigation, communication, radio wave propagation, etc. Below, the calculations use the well-known and simplest model (one-layer Chapman model) for Ne (z) [3]

$$N_e(z) = \sqrt{\gamma \exp[\exp(b(z - z_{\max,e})) + bz]}. \quad (5)$$

Here γ, b are the model parameters; z<sub>max, e</sub> is the height above the earth's surface, for which the maximum value of the electron density is reached. For daytime, the maximum value of Ne (z) = 106 el / cm<sup>3</sup> [3] (model parameters b = 0.01, γ = 5 · 10<sup>13</sup>, z<sub>max, e</sub> = 300 km), the corresponding value of the natural frequency of the ionosphere for z<sub>max, e</sub> is equal to f<sub>p</sub> = 9 MHz.

The use of model (5) makes it possible to determine approximate distortions of signals when variations of its parameters (in particular, when quantifying distortions for the most pronounced effect of the ionosphere in the daytime). To further refine the quantitative estimates of the distortions,

it is necessary to use more complex particular models of the ionosphere, for example, the IRI statistical models and its modifications [11].

**4. DESCRIPTIONS OF DISTORTIONS OF DIGITAL SIGNALS**

Methods for analyzing the distortions considered during the propagation of digital signals belong to two general classes [2, 6, 9]. The first class includes the methods of analyzing the distortions in the time domain using the impulse response h (z, τ) of the ionospheric line [12, 13, 14]. The second class includes methods for analyzing distortions in the frequency domain using the Fourier spectral transform apparatus for h (z, τ) [2, 6, 15].

The representation of the signal E (z, t) using the impulse response of the ionospheric line is given by the convolution ratio [13]

$$E(z, t) = \int_0^\infty E(0, \tau) h(z, t - \tau) d\tau. \quad (6)$$

Distortion analysis methods from the second class are based on the calculation of the inverse Fourier transform [2, 6]

$$E(z, t) = \int_{-\infty}^\infty g(f) \exp(j(\varphi(f, z) + 2\pi ft)) df. \quad (7)$$

Here g (f) is the signal spectrum; - phase of the spectral component for frequency f; - wave number.

The impulse response h (z, τ) in (6) for a stationary inhomogeneous ionosphere can be represented as an approximate analytical expression. One of such expressions is given in [13]

$$h(z, \tau') = \delta(\tau') - u(\tau') \frac{2\pi f_{p,eff}(z, f) \sqrt{z}}{\sqrt{2c\tau'}} J_1 \left( 4\pi f_{p,eff}(z, f) \sqrt{\frac{z\tau'}{2c}} \right). \quad (8)$$

Here  $\delta(\tau)$  is the delta function;  $\tau' = \tau - z/c$ ;  $u(\tau)$  is the unit jump function;  $J_n$  - Bessel function

nth order. For a heterogeneous ionosphere, its effective value of the natural frequency  $f_{p, eff}$  for  $f_0$  is defined as a solution to the equation

$$\int_0^z \sqrt{f_0^2 - f_p^2(x, f)} dx = z \sqrt{f_0^2 - f_{p, eff}^2} \quad (9)$$

When calculating (9) and the  $\varphi(f, z)$  phase in (7), the  $N_e(z)$  profile model (5) is used.

For the frequency range of satellite radio transmission lines, the condition  $f_0 \gg f_p(z, f)$  is fulfilled and the calculation of  $f_{p, eff}$  can be performed using the relation. The effective natural frequency  $f_{p, eff}$  is practically independent of the center frequency  $f_0$  and is functionally related to the total electronic content. This parameter is one of the main characteristics of the Earth's ionosphere [3, 4].

In [14] the second analytical expression is given relative to

$$h(z, \tau) = \delta(\tau - z/c) - u(\tau - z/c) \frac{2\pi f_{p, eff} z J_1(2\pi f_{p, eff} \sqrt{\tau^2 - (z/c)^2})}{c \sqrt{\tau^2 - (z/c)^2}} \quad (10)$$

For radio lines of satellite digital communication systems, the condition  $T \ll z/c$  is satisfied; in this case, the identity of expressions (8) and (10) was proved in [14].

Relations (8) and (10) correspond to the elevation angle  $\theta = 90^\circ$  of the receiving device on board the spacecraft with respect to the transmitting device on the earth's surface. For an arbitrary elevation angle in (10), the zenith slant range is used, calculated using the ratio

In **fig. 1** shows the form of the second term of the characteristic  $h(z, \tau)$  (10), excluding the delta function and the sign.

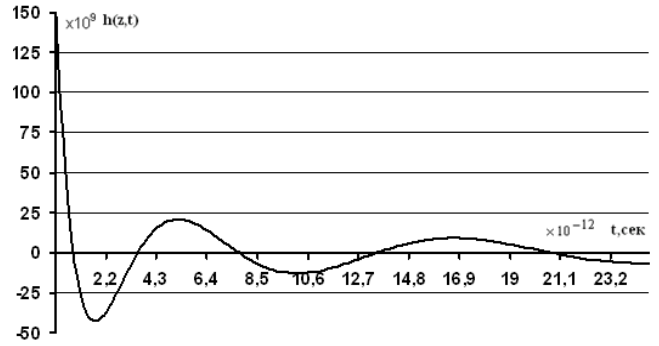


Рис. 1. Вид слагаемого импульсной характеристики  $h(z, \tau)$  (высота  $z = 400$  км,  $f_{p, eff} = 3.5$  МГц).

The curve is calculated for a height of  $z = 400$  km,  $f_{p, eff} = 3.5$  MHz,  $\theta = 90^\circ$ . It can be seen that the characteristic  $h(z, \tau)$  has a sufficiently large length, which determines the aftereffect of the distorted constituent elements and, as a consequence, the presence of ISI in the transmission of digital signals.

In **fig. 2** shows the form of the initial element of a digital signal with two-phase (FM2) manipulation with the envelope in the form of a meander (curve 1), the center frequency of the radio pulse is  $f_0 = 400$  MHz, the duration is  $T = 50$  ns. Curve 2 is calculated using relation (10) and corresponds to this element when propagating in the ionosphere, characterized by the effective value of the natural frequency  $f_{p, eff} = 3.5$  MHz, the height of the ionosphere above the earth's surface is  $z = 400$  km. It can be seen that the distorted element has the radio pulse repetition noted above. The difference in the time of appearance of the initial pulse  $E(0)$ ,

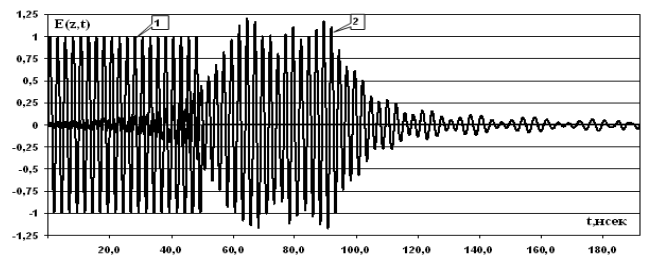


Рис. 2. Вид элемента цифрового сигнала ФМ2: кривая 1 - исходный элемент ( $f_0 = 400$  МГц,  $T = 50$  нс); кривая 2 - вид элемента при распространении в ионосфере ( $f_{p, eff} = 3.5$  МГц,  $z = 400$  км).

t) for the model of propagation in free space and the pulse  $E(z, t)$  at the output of the ionospheric radio link is due to the difference between the group velocity and the speed of light  $c > v_{gr}$ .

The distortions of the constituent elements  $E(z, t)$  cause the presence of energy losses  $\Delta E$  with respect to propagation in free space. These losses are due to a change in the envelope of the distorted signals with a variation in their power and the occurrence of interference by the ISI [12, 14].

The energy loss  $\Delta E$  is estimated on the basis of a comparative analysis of the probabilities of erroneous reception of the  $P_b$  information bits for signals without distortion and with distortions.

For the basic model of channel noise AMGSH, the optimal reception rule is based on the calculation of the cross-correlation of the input realization with the original signals, the probability of an incorrect  $P_b$  reception for the FM2 signals is determined by the relation [5]

$$P_b = 1 - F\sqrt{2E_b / N_0}. \quad (11)$$

Here,  $E_b$  is the energy of signals per information bit,  $N_0$  is the ABGSh spectral density (one-sided),

$$F(x) = \frac{1}{\sqrt{2\pi}} \int_{-\infty}^x \exp(-t^2 / 2) dt.$$

### 5. RESULTS OF CALCULATIONS

Below are the results of estimating the energy loss  $\Delta E$  when digital signals propagate with two-phase (“constellation” FM2) and four-phase (“constellation” FM4) manipulation on the ionospheric radio link with parameters of the daytime ionosphere model (5) - height  $z = 400$  km, central frequency  $f_0 = 400$  MHz. These signals are basic for the development of satellite information systems for various purposes [5, 8, 10]. Variable parameters - the

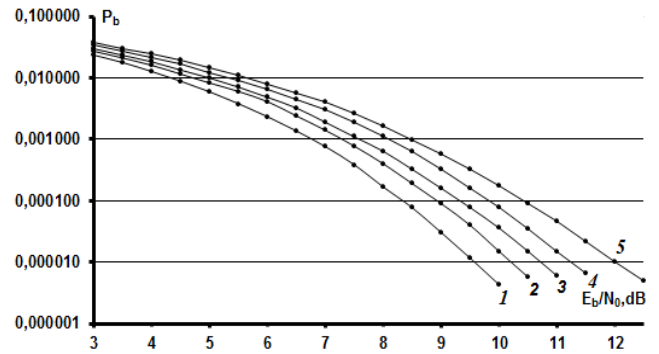


Рис. 3. Вероятности ошибочного приема сигналов ФМ2 при распространении по ионосферной линии,  $f_0 = 400$  МГц,  $z = 400$  км: 1 - распространение в свободном пространстве; 2 -  $\theta = 90^\circ$ ,  $T = 100$  нс,  $\Delta F = 20$  МГц; 3 -  $\theta = 10^\circ$ ,  $T = 100$  нс,  $\Delta F = 20$  МГц; 4 -  $\theta = 90^\circ$ ,  $T = 50$  нс,  $\Delta F = 40$  МГц; 5 -  $\theta = 10^\circ$ ,  $T = 50$  нс,  $\Delta F = 40$  МГц.

duration of the elements of the signals  $T$ , the frequency band of the signals  $\Delta F = 2 / T$ , the signal-to-noise ratio  $E_b / N_0$ ; elevation angle  $\theta$ .

The purpose of the simulation was to calculate approximate estimates of  $\Delta E$  for the most pronounced effect of the ionosphere in the daytime. These estimates must be taken into account when calculating the energy budget of the created P-frequency satellite radio links, an example is the second-generation Cospas-Sarsat satellite system being developed [10].

In Fig. 3 and Fig. 4 shows the dependences of the probabilities of  $P_b$  error on  $E_b / N_0$

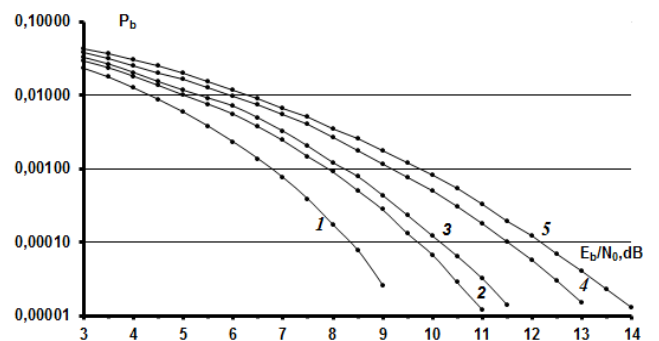


Рис. 4. Вероятности ошибочного приема сигналов ФМ4 при распространении по ионосферной линии,  $f_0 = 400$  МГц,  $z = 400$  км: 1 - распространение в свободном пространстве; 2 -  $\theta = 90^\circ$ ,  $T = 100$  нс,  $\Delta F = 20$  МГц; 3 -  $\theta = 10^\circ$ ,  $T = 100$  нс,  $\Delta F = 20$  МГц; 4 -  $\theta = 90^\circ$ ,  $T = 50$  нс,  $\Delta F = 40$  МГц; 5 -  $\theta = 10^\circ$ ,  $T = 50$  нс,  $\Delta F = 40$  МГц.

for the FM2 and FM4 signals, calculated by computer simulation of the reception algorithm based on correlation ratios.

In modeling the reception of signals, an interval estimate of the probability of Pb was made by calculating the frequency  $w = x / u$ . Here x is the number of erroneous decisions in a sequence of independent computational experiments of volume u, determined by the size of the confidence interval, the probability Pb, the confidence probability Pconf. For example, for  $P_b = 10^{-5}$ ,  $\alpha = 0.5P_b$  (confidence interval  $[0.5P_b, 1.5P_b]$ ) and  $P_{conf} = 0.95$ , the required number of experiments is  $u > 1540000$ .

Curve 1 in fig. 3 is calculated using relation (11) and corresponds to the propagation of FM2 signals in free space — the probability  $P_b = 10^{-5}$  is ensured at the ratio  $E_b/N_0 = 9.5$  dB. Curves 2, 3, 4, 5 are obtained by modeling and correspond to the propagation along the ionospheric radio link. Curves 2 and 3 correspond to the duration  $T = 100$  ns ( $\Delta F = 20$  MHz) and the elevation angles  $\theta = 90^\circ$  and  $\theta = 10^\circ$ . Curves 4 and 5 correspond to the duration  $T = 50$  ns ( $\Delta F = 40$  MHz) and elevation angles  $\theta = 90^\circ$  and  $\theta = 10^\circ$ .

The summary **Table** shows the corresponding energy loss estimates  $\Delta E$  for  $P_b = 10^{-5}$ . One can see a monotonous decrease in the probability of Pb to 0.000001 depending on  $E_b / N_0$ , which shows a rather small influence of AMI interference on the

probability characteristics in this case relative to the effect due to the energy variations of the elements of the digital signals. It is also seen that with a decrease in the duration T (an increase in the frequency band  $\Delta F$ ), an increase in  $\Delta E$  values is observed - at  $\theta = 0^\circ$ , we have  $\Delta E = 0.5$  dB for  $T = 100$  ns and  $\Delta E = 1.0$  dB for  $T = 50$  ns; at  $\theta = 10^\circ$ , we have  $\Delta E = 1.5$  dB for  $T = 100$  ns and 2.5 dB for  $T = 50$  ns.

In fig. 4 shows the probability curves for the signals FM4. Curve 1 is also calculated using relation (11) and corresponds to propagation in free space. Curves 2, 3, 4, 5, 6 are obtained by modeling and correspond to the propagation along the ionospheric radio link. Curves 2 and 3 correspond to the duration  $T = 100$  ns ( $\Delta F = 20$  MHz) and angles  $\theta = 90^\circ$  and  $\theta = 10^\circ$ . The summary table shows the corresponding estimates of the energy loss  $\Delta E$  for FM4 signals at  $P_b = 10^{-5}$ . It can be seen that with respect to the signals of the FM2, the energy losses increase - at  $P_b = 10^{-5}$ , the loss of  $\Delta E$  with respect to curve 1 reaches 1.5 and 2.0 dB. Curves 4 and 5 correspond to the duration  $T = 50$  ns ( $\Delta F = 40$  MHz) and angles  $\theta = 90^\circ$  and  $\theta = 10^\circ$ . In this case, the  $\Delta E$  losses also increase and reach 3.5 and 4.5 dB, which shows an increase in the influence of AMI interference and variations in the energy of digital signal elements on the probability characteristics of reception with respect to the FM2 signals.

6. CONCLUSION

Methods are given for describing digital signals as they propagate through the ionospheric radio links of satellite information transmission systems. Description methods are based on the use of a stationary ionospheric radio link model in the form

Таблица  
Оценки энергетических потерь  $\Delta E$  при распространении сигналов ФМ2 и ФМ4 по ионосферной радиолинии относительно распространения в свободном пространстве ( $P_b = 10^{-5}$ ).

Параметры		$T = 100$ нс	$T = 50$ нс
ФМ2	$\theta = 90^\circ, \Delta E_{\text{дБ}}$	0.5	1.0
	$\theta = 10^\circ, \Delta E_{\text{дБ}}$	1.5	2.5
ФМ4	$\theta = 90^\circ, \Delta E_{\text{дБ}}$	1.5	3.5
	$\theta = 10^\circ, \Delta E_{\text{дБ}}$	2.0	4.5

of a linear filter with an impulse response represented by analytical expressions.

The results of the quantitative estimation of the energy losses when receiving the distorted signals FM2 and FM4 when they propagate through radio links of the P-frequency range relative to the propagation in free space are given. By modeling, it was shown that the energy losses depend on the duration of the digital signal elements (frequency band of signals) and on the elevation angle and reach 2.5 dB and 4.5 dB, respectively, for FM2 signals and FM4 signals for the most pronounced effect of the ionosphere in the daytime, which must be taken into account when calculating energy budget of satellite radio links.

Estimation of energy losses using more complex models of the height profiles of the electron density of the ionosphere, taking into account, in particular, the two-beam propagation of signals with different “constellations”, represents a promising line of research.

**REFERENCES**

1. Kolosov MA., Armand NA, Yakovlev OI. The propagation of radio waves in space communications. M., Communication, 1969, 156 p.
2. Ginsburg OT. The propagation of electromagnetic waves in the plasma. Moscow, Science, 1967, 684 p.
3. Dolukhanov MP. The propagation of radio waves. M., State. Communications and Radio Publishing House, 1960, 336 p.
4. Yakovlev OI, Yakubov VP, Uryadov VP, Pavelev AG. The propagation of radio waves. M., LENAND, 2009, 496 c.
5. Sklyar B. Digital communication. Theoretical foundations and practical

- application. M., Publishing House “Williams”, 2003, 1104 p.
6. Armand ON. Distribution of broadband signals in dispersive environments. Radio engineering and electronics, 2003, 48 (9): 1045-1057.
7. Ivanov DV, Ivanov VA, Mikheeva NN, Ryabov NV, Ryabov MI. Distribution of shortwave spread spectrum signals in a medium with nonlinear dispersion. Radio engineering and electronics, 2015, 60 (11): 1167-1177.
8. Hofmann-Wellenhof B, Lichtenegger H, Collins J. Global Positioning System. Theory and Practice. Springer-Verlag, New York, 1994, 392 p.
9. Kutuza BG, Moshkov AV, Pozhidaev VN. Combined method that eliminates the influence of the ionosphere when processing signals of P-range airborne radars with synthetic aperture. Radio engineering and electronics, 2015, 60 (9): 889-895.
10. Specification for 2-generation COSPAS-SARSAT 406 MHz distress beacons. C / S T.018. Issue 1. 2016.
11. Bilitza D, McKinnell LA, Reinisch B, Fuller-Rowell T. The International Reference Ionosphere (IRI) today and in the future. Journal of Geodesy, 2011, 85: 909-920.
12. Nazarov LE, Batanov VV. Probabilistic characteristics of the detection of radio pulses during the propagation of satellite communication systems over the ionospheric transmission lines. Technology and Electronics, 2017, 62 (9): 866-874.
13. Dvorak SL, Dudley DG. Propagation of Ultrawideband Electromagnetic Pulses Through Dispersive Media.

- IEEE Transactions on Electromagnetic Compatibility, 1995, 37 (2): 192-200.
14. Nazarov LE, Batanov VV, Zudilin AS. Distortion of radio pulses during the propagation of satellite communication systems through the ionospheric lines. Journal of Radio Electronics, 2016, №2. Access mode: <http://jre.cplire.ru/jre/feb16/1/text.pdf>.
  15. Nazarov LE, Batanov VV. Analysis of distortions of radio pulses during the propagation of satellite communication systems over ionospheric transmission lines. Electromagnetic waves and electronic systems, 2016, 21 (5): 37-45.

# POLARIZATION-ANGULAR DEPENDENCES OF THE REFLECTION AND TRANSMISSION COEFFICIENTS OF FREE PLATES OF QUASI-ANISOTROPIC ICE IN THE L-RANGE

Mikhail G. Evtikhov, Galina V. Arzamastseva

Kotelnikov Institute of Radioengineering and Electronics of RAS, Fryazino Branch, <http://fire.relarn.ru>  
Fryazino 141190, Moscow Region, Russian Federation

[emg20022002@mail.ru](mailto:emg20022002@mail.ru), [arzamastseva@mail.ru](mailto:arzamastseva@mail.ru)

*Abstract.* The polarization-angular dependences of the reflection and transmission coefficients of free plane-parallel ice plates in the region of 0°C, when flat electromagnetic waves of s- and p-polarization fall on them and are recorded by an L-band radiometer 1.41 GHz are studied theoretically. It is shown that the observation of interference effects in ice plates in the L-range is limited to a plate thickness of 4.3 meters. This limitation is due to a radiometer bandwidth of 20 MHz. Ice is considered an isotropic or uniaxial crystal with an anisotropy coefficient of 15%. Three types of directions of the anisotropy axis are considered in the assumptions of the quasi-anisotropic medium model. The value of the Brewster angle is obtained, and it is shown that it does not depend on anisotropy. Reflective and anti-reflective effects are associated with a change in wavelength in the direction perpendicular to the surface of the plate. In turn, this length depends on the angle of incidence, polarization, and direction of the anisotropy axis. The possibility of forming interference regions of transparency for certain thicknesses is shown, the reflection coefficients for both polarizations are significantly reduced, and the transmittances increase. Interference areas of transparency can be formed both at the Brewster angle and at other angles. These effects are associated with interference phenomena and their enhanced effect of anisotropy.

*Keywords:* reflection, refraction, Fresnel equations, permittivity, millimeter waves, ice, resonance, multilayer plates.

UDC 0535.391.4, 53.082.53, 53.083.2

*Bibliography* - 30 references

Received 18.03.2019, accepted 05.04.2019

*RENSIT*, 2019, 11(1):73-84

DOI: 10.17725/rensit.2019.11.073

## CONTENTS

1. INTRODUCTION (73)
  2. SELECTION OF COORDINATE AXES AND ASSUMPTIONS OF THE MATHEMATICAL MODEL (74)
  3. CONDITIONS OF INTERFERENCE EFFECTS FOR FREE PLATES OF ICE AT VARIOUS ANGLES OF INCIDENCE (75)
  4. THE EFFECT OF ANISOTROPY ON THE WAVELENGTH (75)
  5. ENHANCING THE INFLUENCE OF X-ANISOTROPY BY INTERFERENCE EFFECTS (76)
  6. EXAMPLES OF AREAS OF TRANSPARENCY IN SINGLE-LAYER AND THREE-LAYER PLATES (76)
  7. MAXIMUM THICKNESS OF ICE PLATES OF OBSERVATION OF INTERFERENCE STRUCTURES IN THE L-BAND (76)
  8. CONCLUSION (77)
- APPENDIX (78)  
REFERENCES (78)

## 1. INTRODUCTION

Applications of the general theory of linear electromagnetic waves of anisotropic media [1, 2, 3] require the agreement of general methods based on linear algebra and more traditional approaches to solving diffraction problems. Solutions of many problems of optics [1, 4, 5], acoustics [6], ellipsometry [7], X-ray optics [8, 9] and remote sensing of the environment [10] are based on the use of Fresnel and Fresnel-Airy coefficients. However, in the Fresnel formulas, radiation is assumed to be monochromatic, and the media should be isotropic. The observed interference structures of microwave radiation depend on the bandwidth of the radiometer. Structures are considered theoretically in the case of normal incidence of radiation in

[11]. The class of quasi-anisotropic multilayer plates is considered in [12-14]. This class includes anisotropic media, where  $s$ - and  $p$ -polarized waves propagate independently. A generalization of Fresnel-Airy formulas to quasi-anisotropic media is considered in [14]. The combination of the methods from [11] and [14] makes it possible to theoretically investigate the effect of anisotropy on the reflection and transmission coefficients of electromagnetic radiation. This paper discusses free ice plates in the  $L$ -range.

The Fresnel-Airy coefficients, reflection and transmission coefficients are used in radiometric methods for calculating the brightness temperature of the controlled surface [10]. At frequencies of 1 GHz – 100 GHz, ice, snow, and other types of the earth's surface are studied for a long time [10, 15-22]. In the range above 2 GHz, the behavior of the Fresnel-Airy coefficients of ice plates is complicated by the non-monotonic dependence of the dielectric constant on frequency, as well as by the presence of microcracks [20]. It was reported about the observation of Ginzburg-Pekar waves in this range, near 0°C [24-25]. The complexity of physical phenomena in ice at high frequencies makes the  $L$ -band (1-2 GHz) promising for theoretical study. The wavelengths of the  $L$ -range are about 20 cm in vacuum and about 10 cm for ice; the Debye formula for the dielectric constant of ice remains valid in it, which simplifies adequate mathematical models. The results of this paper for the  $L$ -range should allow to separate the influence of anisotropy from more complex phenomena in other ranges. The presence of mass-produced domestic and foreign  $L$ -band radiometers [17, 22, 23] creates the prospect of practical applications of theoretical results.

The practical significance of studying the electric and acoustic anisotropy of ice is substantiated by the significant effect of

anisotropy on the wave processes in sea ice [26]. It is noted that the dielectric anisotropy and anisotropy of the elastic properties of ice may not coincide. In [27], [28], ice is considered as a uniaxial crystal and is characterized by the anisotropy coefficient. For ice-1, the anisotropy of the dielectric constant in the microwave range is approximately 15% [27]. Laboratory experiments to measure the anisotropy of the dielectric constant and specific absorption of arctic drift ice in the microwave range are described in [28], values from 2% to 15% for old ice were obtained, it was noted that the new ice layers are isotropic. Various variants of the direction of the anisotropy axis with respect to the direction of propagation of microwave radiation were considered.

Free plates are of interest for laboratory research, their consideration is a necessary stage in the development of new algorithms. Interference effects in free plates appear more clearly, and the calculation of transmittance is simpler.

In this paper, we restrict ourselves to the consideration of free plates.

The aim of the article is to theoretically consider the influence of ice anisotropy and non-monochromatic radiation on polarization-angle diagrams of reflection and transmission coefficients of  $L$ -band electromagnetic waves for free plane-parallel ice plates assuming that the medium is quasi-anisotropic.

## 2. SELECTION OF COORDINATE AXES AND ASSUMPTIONS OF THE MATHEMATICAL MODEL

In **Fig. 1**, we denote the wave number in parentheses, and the medium number in square brackets. The  $x$ -axis is orthogonal to the ice surface. The medium [1] and the medium [3] are air (vacuum). The medium [2] is isotropic or anisotropic ice. The axis of coordinates  $y$  is parallel to the projection of the wave vector of the wave in vacuum onto the interface

between the media. The axis of coordinates  $z$  is orthogonal to the plane of the figure and is directed to the reader, it lies in the plane of the surface of the plate. The incident wave is indicated by a number 0. The reflected wave has the number 1. The refracted wave in the medium 1 has the number 2, the reflected wave in the medium 2 has the number 3. The wave coming out of the plate has the number 4. When calculating the amplitudes of waves 3 and 4, their multiple reflections are taken into account according to the algorithms [15]. We consider the wave with elliptical polarization as two independently propagating linearly polarized waves with  $s$ - and  $p$ -polarizations. The electric field of a wave with  $s$ -polarization is directed along the  $z$  axis. It is convenient to define a wave with  $p$ -polarization (like  $s$ -polarization), as a wave whose magnetic field is directed along the axis [1]. As the magnitude of the amplitude of a wave with  $p$ -polarization, is used. This Such a definition is adequate in media with absorption. In the algorithms used in this work from [15], the angle of refraction is not fundamentally applicable. Instead of them, in accordance with the approach [1], complex wave vectors are considered. Therefore, it is possible to speak of the angle of refraction only formally, as of the real part of the corresponding complex value.

In quasi-anisotropic media, wave vectors (angles of refraction) and wave propagation speeds for  $s$ - and  $p$ -polarizations should

differ. Further, speaking of  $x$ -anisotropy, we will consider a uniaxial crystal, in which the anisotropy axis is directed along the  $x$ -axis, orthogonal to the surface of the ice plate. Similarly, we will speak of  $y$ - and  $z$ - anisotropy as cases when the anisotropy axis is parallel to the ice surface. We assume that there is no spatial dispersion and dispersion of the axes. Then waves with  $s$ - and  $p$ -polarizations can be identified with the concepts of “ordinary” and “extraordinary” waves adopted in the optics of anisotropic media (see **Appendix**).

Angles of wave propagation are measured relative to the normal to the plate surface. The article deals only with free plates in a vacuum. Further, the terms “angle of incidence”, “angle of observation” are used as equivalent. For a free plate, the angle of incidence is equal to the angle of reflection and equal to the angle of the direction of propagation of the wave leaving the plates, all angles being equal and real. The transmittance and reflection coefficients of the free plates are equal to the square of the modules of the Fresnel-Airy coefficients.  $|R_s|^2$ ,  $|T_s|^2$  – reflection and transmission coefficients for waves with  $s$ -polarization.  $|R_p|^2$  и  $|T_p|^2$  – for waves with  $p$ -polarization.

In the calculations, the value of the relative complex dielectric constant of ice near  $0^\circ C$  is equal to  $\epsilon = 3.18 + 0.0007i$  [16, 29, 30]. The value of the imaginary part varied within 15%, real  $-2\%$ , the changes did not significantly affect the results.

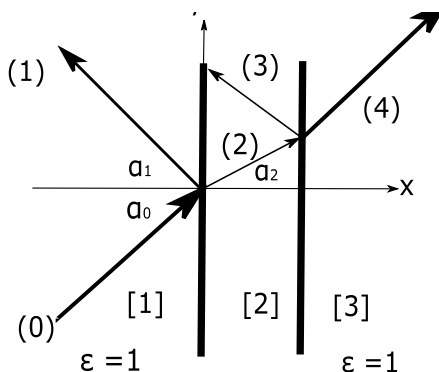


Fig.1. Wave vectors in the free plate.

### 3. CONDITIONS OF INTERFERENCE EFFECTS FOR FREE PLATES OF ICE AT VARIOUS ANGLES OF INCIDENCE

The wave vector can be decomposed into the ortes of the coordinate axes ( $e_x$ ,  $e_y$ ,  $e_z$ ) and can be represented through the wavelengths in the corresponding directions, noting some conventionality of such a term:

$$\mathbf{k} = \mathbf{k}_x + \mathbf{k}_y + \mathbf{k}_z = \frac{2\pi}{L_x} \mathbf{e}_x + \frac{2\pi}{L_y} \mathbf{e}_y + \frac{2\pi}{L_z} \mathbf{e}_z.$$

Denote by  $L_x$  the wavelength in the direction perpendicular to the surface of the plate. For free plates with a multiple of  $L_x/2$ , the reflection coefficient is significantly reduced. For plates with thickness  $L_x/4 + nL_x/2$ , ( $n$  is an integer), the reflection coefficient increases. (Note that the conditions of extremal reflection are reversed in the case of a monotonic change in the refractive indices in the layers [5]). At a frequency of 14.1 GHz, the wavelength in a vacuum is  $L_0 = 21.3$  cm. With normal incidence ( $\alpha = 0$ ), the wavelength of isotropic ice is 11.9 cm. In general

$$L_x = \frac{L_0}{\sqrt{\mu\epsilon - (\sin \alpha)^2}} = \frac{21.3}{\sqrt{3.18 - (\sin \alpha)^2}}.$$

As the angle  $\alpha$  increases, the measuring device records the waves with increasing wavelength  $L_x$ . Therefore, the conditions of extreme reflection are different at different angles. **Fig. 2** shows the theoretically calculated dependences for isotropic ice on the angle  $\alpha$  for  $L_x$ ,  $L_y$ , and the angle of refraction. For isotropic ice, the value of  $L_x$  varies from 11.9 cm to 14.4 cm at different angles and leads to interference effects in the plates.

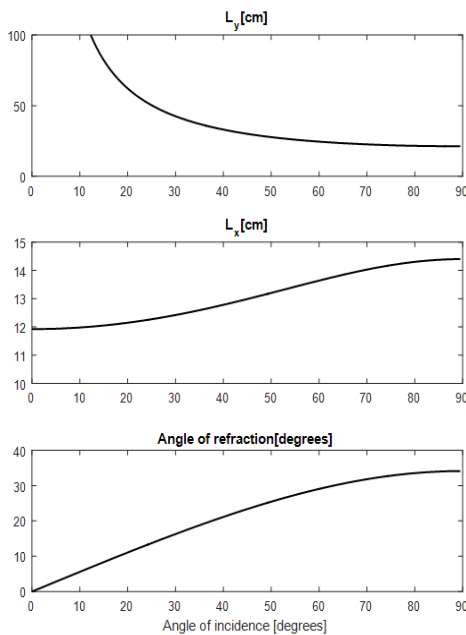


**Fig. 2.** The dependence of the wavelength  $L_y$ , the wavelength  $L_x$  and the angle of refraction from the angle of incidence.

#### 4. THE EFFECT OF ANISOTROPY ON THE WAVELENGTH $L_x$

**Appendix** shows modifications of Maxwell's equations in quasi-anisotropic media for plane linear harmonic (monochromatic) waves of  $s$ - and  $p$ -polarization. In the case of  $x$ -anisotropy, we denote  $L_x$  by  $L_{xx}$ . Let  $u_x = 0.15$  be the  $x$ -anisotropy coefficient. Accordingly, we denote  $L_{xy}$ ,  $u_y$  and  $L_{xz}$ ,  $u_z$  for the cases of  $y$ - and  $z$ -anisotropies. The relative dielectric constant and other coefficients are written as:

$$\epsilon_{11} = \epsilon(1 + u_x), \epsilon_{22} = \epsilon_{33} = \epsilon; \epsilon_{31} = \epsilon_{32} = \epsilon_{12} = 0; \mu = 1;$$

$$\frac{\omega}{c} = k_0 = \frac{2\pi}{L_0}, k_x = \frac{2\pi}{L_{x,x}}, k_y = k_0 \sin \alpha.$$

$x$ -anisotropy affects only  $p$ -polarized waves and does not affect  $s$ -polarized waves. The conditions for the existence of solutions for  $p$ -waves are converted to:

$$\epsilon^2(1 + u_x) - \epsilon(k_y/k_0)^2 - \epsilon(1 + u_x)(k_x/k_0)^2 = 0.$$

From here we get the wavelength  $L_{xx}$ . We represent it in terms of the length  $L_x$  for an isotropic medium and the correction for anisotropy proportional to  $u_x$ :

$$L_{x,x} = \frac{L_0}{\sqrt{\epsilon - \frac{(\sin \alpha)^2}{1 + u_x}}} \approx L_x - \frac{L_x^3 (\sin \alpha)^2}{2L_0^2} u_x. \quad (1)$$

As  $L_x$  should take the values shown in Fig. 2, depending on the angle of incidence. In the case of 15% anisotropy, this correction monotonously grows from zero to 0.6 cm when the angle of incidence varies from zero to 90°.

If the anisotropy axis is directed along the  $y$  axis, then the wavelength  $L_{x,y}$  is equal to:

$$L_{x,y} = \frac{L_0}{\sqrt{(\epsilon - (\sin \alpha)^2)(1 + u_y)}} \approx L_x - \frac{L_x}{2} u_y. \quad (2)$$

If the anisotropy axis is directed along the  $z$  axis, then the anisotropy does not affect the  $p$ -polarization. The condition for the existence of a solution for  $s$ -polarization takes the form  $\epsilon(1$

$+ u_z) - (k_y/k_0)^2 - (k_x/k_0)^2 = 0$ . The wavelength  $L_{x,z}$  is written as:

$$L_{x,z} = \frac{L_0}{\sqrt{\varepsilon(1+u_z) - (\sin \alpha)^2}} \approx L_x + \frac{\varepsilon L_x^3}{2L_0^2} u_z. \quad (3)$$

In all subsequent graphs, the anisotropic case is represented by solid curves, and the isotropic case is represented by curves consisting of points.

**5. ENHANCING THE INFLUENCE OF X-ANISOTROPY BY INTERFERENCE EFFECTS**

In accordance with the multiplier  $(\sin \alpha)^2$  in formula (1), anisotropy in the  $x$ -direction can occur only at sufficiently large angles of incidence and for sufficiently thick plates. For angles greater than  $80^\circ$ , the wavelength in an isotropic medium can be estimated as 14.3 cm. The correction for anisotropy of 15% is 0.6 cm (see section 3), the result is a value close to 15 cm. Therefore, at plate thicknesses of a factor of 7.5 cm, on the curves of the reflection and transmission coefficients, the effects of extreme reflection should be observed for the anisotropic case.

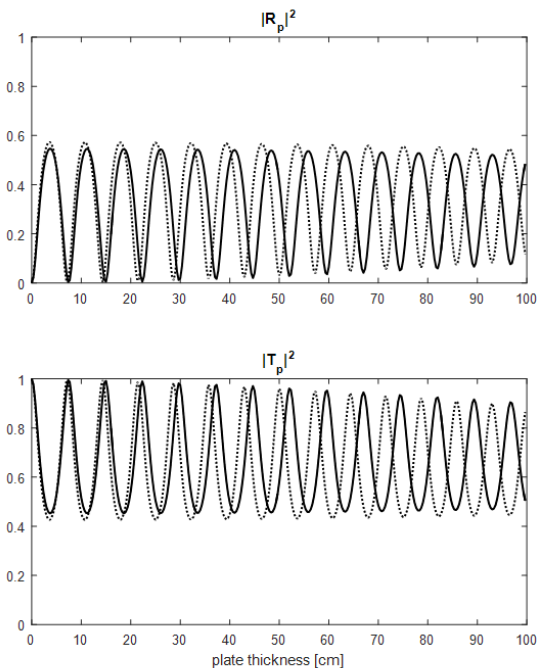


**Fig. 3.** The dependence of the reflection and transmission coefficients on the thickness of the free plate at an observation angle of  $80^\circ$ .

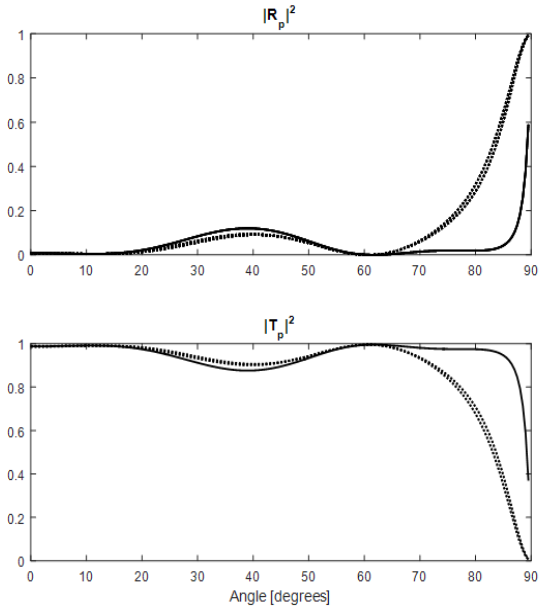


**Fig. 4.** The reflection and transmission coefficients of ice at a plate thickness of 30 cm.

**Fig. 3** shows the reflection and transmission coefficients at ice thicknesses from 0 cm to 100 cm for  $p$ -polarized waves incident at an angle of  $80^\circ$ . Due to the difference in the wavelength in the  $x$ -direction in an isotropic and anisotropic medium with an ice thickness of 85 cm, the oscillations are in antiphase.

**Fig. 4** shows the curves for  $p$ -polarization for a thickness of 30 cm. Size 30 cm is a multiple of 6 cm and 7.5 cm. At angles of  $0^\circ$ - $15^\circ$ , the reflection is small. In addition, for anisotropic plates, low reflection occurs at large angles ( $60^\circ$ - $80^\circ$ ).

Recall that the polarization-angle dependences are depicted in the figures in the anisotropic case by solid curves, and in the isotropic case - by curves consisting of points.

**6. EXAMPLES OF AREAS OF TRANSPARENCY IN SINGLE-LAYER AND THREE-LAYER PLATES.**

**Fig. 5** shows the dependence on the angle of incidence of the reflection coefficients and the transmission of a plate 50 cm thick. For isotropic ice, an area of transparency takes place at an angle of  $30^\circ$ . An elliptically polarized wave should pass without reflection and with low

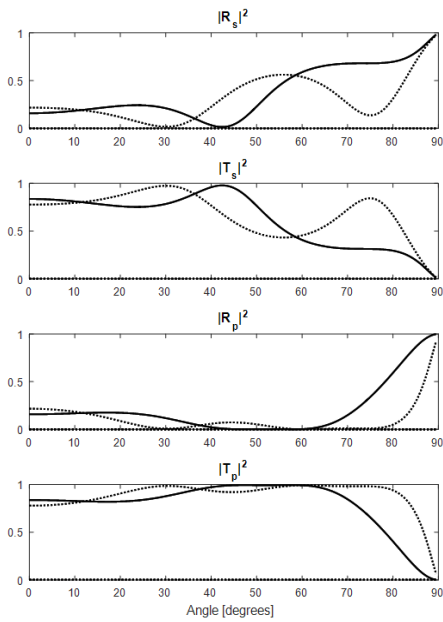


**Fig. 5.** The reflection and transmission coefficients of ice at a single-layer plate thickness of 50 cm  $z$ -anisotropy and  $y$ -anisotropy.

losses. The transparency region is destroyed due to the influence of  $y$ -anisotropy or  $z$ -anisotropy in 15%. The curves of the anisotropic case are shifted relative to the curves of the isotropic case: for  $s$ -polarization under the influence of  $z$ -anisotropy, or for  $p$ -polarization under the influence of  $y$ -anisotropy.

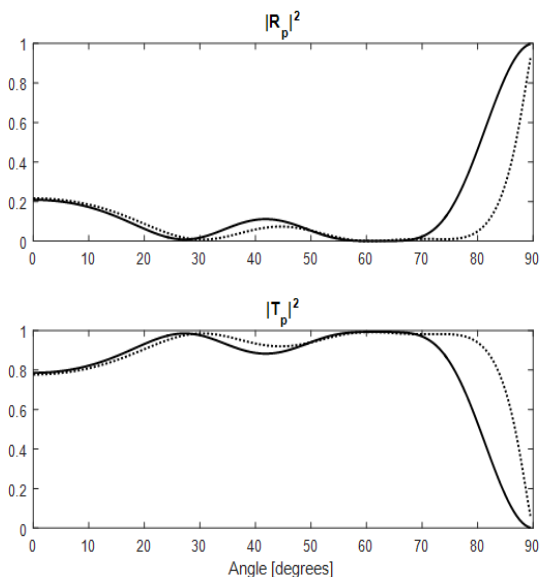


**Fig. 6.** The reflection and transmission coefficients of ice at a single-layer plate thickness of 50 cm  $x$ -anisotropy.

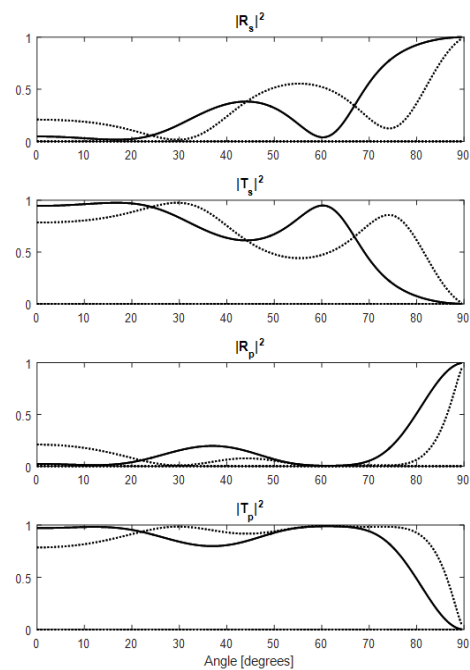


**Fig. 7.** The reflection and transmission coefficients of ice of a three-layer plate with different anisotropies.

**Fig. 6** illustrates the effect of anisotropy in the  $x$  direction for a plate with the same thickness of 50 cm as in the previous figure. But the anisotropy axis is 15% orthogonal to the plate surface ( $x$ -anisotropy). In the region of  $30^\circ$  the blue line shifts within a few degrees. Transparency region is not destroyed.

**Fig. 7** shows the reflection and transmission coefficients for the case when the plate with a total thickness of 50 cm (as in the previous case) is divided into 3 sublayers of the same thickness. In the first sublayer, there is a 15%  $x$ -anisotropy, in the second,  $y$ -anisotropy, in the third,  $z$ -anisotropy. Isotropic and anisotropic ice curves differ at all angles. The region of low reflection of the  $s$ -polarization is shifted to the Brewster angle and the transparency region is formed there. As a result of the combined influence of all types of anisotropy, another area of increased transparency is formed at angles of incidence of  $0^\circ$ - $20^\circ$ .

**7. MAXIMUM THICKNESS OF ICE PLATES OF OBSERVATION OF INTERFERENCE STRUCTURES IN THE L-BAND**

In Fig. 8, the reflection and transmission coefficient curves for plates with a thickness of 98, 99, 100, 101, 102 cm are shown in the same figure. These thicknesses differ from the average by no more than 2%, but the oscillations of the curves differ significantly and merge into a wide strip. For plates of ice about a meter thick, these oscillations should complicate radiometric measurements.

Fig. 3 shows the variations of the reflection and transmission coefficients at an angle of incidence of 80°. There is a slow decrease in the amplitude of oscillations. It is due not to the absorption of waves, but to interference effects arising from the finite width of the radiometer's passband [11]. The maximum thickness of the plate can be estimated by the formula

$$d = \frac{\lambda f}{2\Delta f} = 423\text{cm},$$

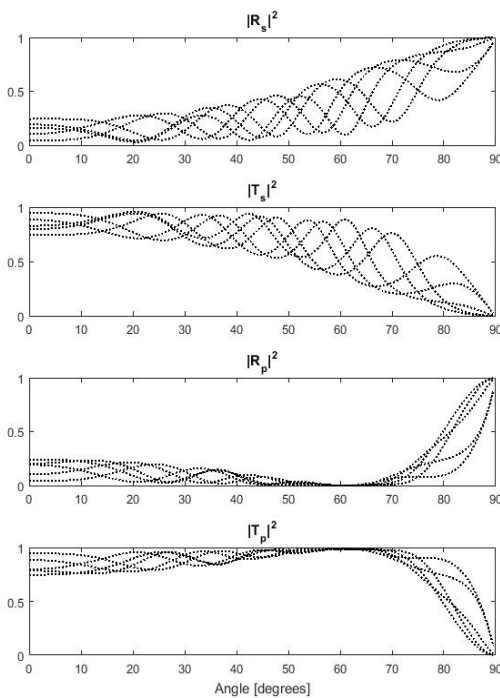


Fig. 8. The reflection and transmission coefficients of isotropic ice with a plate thickness of 98, 99, 100, 101, 102 cm.

$\lambda$  – wavelength;  $f = 14.1\text{GHz}$  – frequency;  $\Delta f = 0.02\text{ GHz}$  – radiometer band.

Fig. 9 shows the reflection and transmission coefficients for  $p$ -polarized waves with a slightly smaller thickness, 400 cm. Oscillations on curves for anisotropic ice due to interference effects are noticeable. With a larger plate thickness, the amplitudes of interference oscillations decrease, become imperceptible, but exist.

**8. CONCLUSION**

The polarization-angular dependences of the reflection and transmission coefficients of smooth ice plates for radiometric measurements at a frequency of 1.41 GHz with a bandwidth of 20 MHz are theoretically considered.

When the anisotropy coefficient of ice is 15%, the effect of anisotropy on the reflection and transmission coefficients of infinitely thick plates is insignificant, of the order of a few percent for anisotropy  $y$ - and  $z$ -, and for  $x$ -anisotropy this effect is even less. These estimates are changed when taking into account the thickness of the plates.

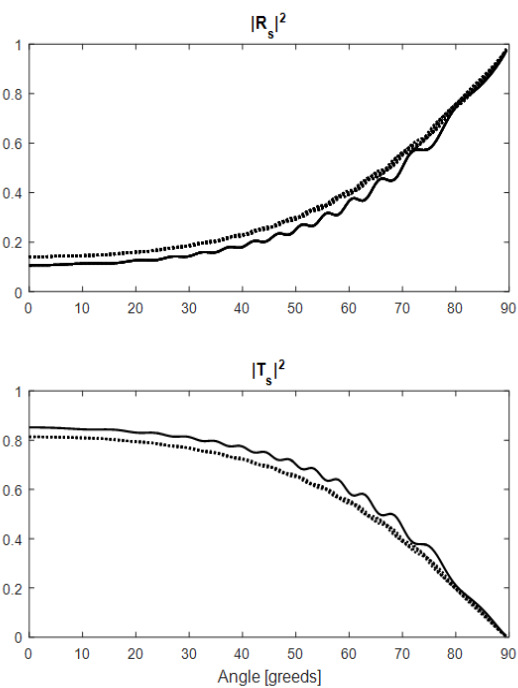


Fig. 9. Reflection and transmission coefficients of  $s$ -polarized ice at a thickness of 400 cm.

The wavelength in the direction orthogonal to the surface of the plate inside isotropic ice, at a frequency of 1.41 GHz, is  $L_x = 11.9$  cm. This means that the behavior of the reflection and transmission coefficients changes as the thickness of the ice plate changes every  $L_x/4 \approx 3$  cm. When the plate thickness changes, there are oscillations of the reflection and transmission coefficients. Between oscillations of the coefficients corresponding to the isotropic and anisotropic case, a phase difference appears that increases with increasing plate thickness, and the effect of relative errors in thickness values on the reflection and transmission coefficients increases. The decrease in the amplitude of oscillations with increasing plate thickness is due to the presence of a limited radiometer frequency band in the frequencies [11].

$$d = \frac{\lambda f}{2\Delta f} = 423 \text{ cm},$$

– maximum thickness of the ice plate, at which interference effects are already invisible.

The knowledge of more accurate values of  $L_x$  makes it possible to interpret the phenomena of extremal reflection arising in plane-parallel ice plates less than 423 cm thick, depending on polarization, viewing angle and ice anisotropy. Assuming that anisotropy is small and ice can be considered a uniaxial crystal, in which the anisotropy axis coincides with one of the coordinate axes, formulas for  $L_x$  are derived. The versions of formulas in the form of corrections due to anisotropy are given (formulas (1) - (3) in section 3).

The model of quasi-anisotropic media [15] (see also **Appendix**) makes it possible to take into account the anisotropy of the medium, without going beyond the concepts associated with the Fresnel formulas. Interference phenomena enhance the effect of anisotropy. The influence of  $x$ -anisotropy becomes significant at angles of more than  $70^\circ$  and ice thicknesses of several tens of centimeters. If the anisotropy axis is parallel to the plane of the plate, then the interference

effects of anisotropy change the reflection and transmission coefficients of the plates in the whole range of angles. The possibility of forming regions of transparency in free plates of ice is theoretically shown. It was verified that the Brewster angle does not depend on the anisotropy of ice. It is shown that transparency regions can be associated with the Brewster angle, but they can also arise at other angles. Anisotropy both destroys areas of transparency, and can contribute to the formation of such areas.

The shorter the wavelength, the smaller the required antenna size. The advantage of the  $L$ -range theoretical study is that in this range, it is possible to use simpler mathematical models with dielectric constant values known from the literature, the Debye formula remains valid. While in the range of 3 GHz – 100 GHz, the theoretical explanation of the passage of microwave radiation should be more complex. The obtained numerical estimates of the linear problem can be recalculated for radiometers with shorter wavelengths and used as an approximation for a more detailed study of the properties of ice in other ranges. However, with such a transfer of results, one should take into account the ratio of the radiometer band size to its frequency, the possibility of a more complex behavior of the dielectric constant and its dispersion.

In this paper, only free plates are considered. This fact limits the application of the numerical results obtained mainly by laboratory experiments. For solving the problems of monitoring the earth's surface (and a number of other problems), it would be useful to generalize the algorithms for obtaining transmittance for the case of arbitrary quasi-anisotropic environments. The behavior of the reflection and transmission coefficients for such cases should repeat the same oscillations as in the case of a free plate, with the same wavelengths, but with a different attenuation and phase shift.

The work was carried out within the framework of the state task.

APPENDIX

Permissible components of the dielectric and magnetic permeability tensors for quasi-anisotropic media

Restrictions on the dielectric and magnetic permeability tensors for which TE- and/or TM-waves exist (with the field structure  $(H_x, H_y, E_z)$  or  $(-E_x, -E_y, H_z)$ ) were considered in [13–15] and the corresponding generalized Fresnel formulas were obtained. In [15], the conditions for the existence of TE- and TM-waves were proposed to be considered as a definition of a special class of media: quasi-anisotropic media. Quasi-anisotropic media include all isotropic media and some anisotropic media. For multilayer plates of quasi-anisotropic media, algorithms have been constructed that generalize the Fresnel-Airy formulas [15]. The results of this paper were obtained using generalized algorithms and were verified using estimates using the usual Fresnel and Fresnel-Airy formulas. (We also used integration over the radiometer bandwidth and comparing the results with [11]). The concept of quasi-anisotropic media and the ability to solve Fresnel problems for multilayer plates with smooth boundaries from such media expands the range of solvable problems of electromagnetic wave propagation.

Let us write down the permittivity and magnetic permeability tensors admissible for quasi-anisotropic media. The icon  $\times$  indicates the permissible components on which the properties of the corresponding waves do not depend.

For  $s$ -waves with

$$\hat{\epsilon} = \begin{pmatrix} \times & \times & 0 \\ \times & \times & 0 \\ \times & \times & \epsilon_{33} \end{pmatrix}; \quad \hat{\mu} = \begin{pmatrix} \mu_{11} & \mu_{12} & \times \\ \mu_{21} & \mu_{22} & \times \\ 0 & 0 & \times \end{pmatrix}$$

Maxwell's equations for the amplitudes of monochromatic waves take the form:

$$\begin{pmatrix} \mu_{11} & \mu_{12} & -\frac{c}{\omega}k_y \\ \mu_{21} & \mu_{22} & \frac{c}{\omega}k_x \\ -\frac{c}{\omega}k_y & \frac{c}{\omega}k_x & \epsilon_{33} \end{pmatrix} \begin{pmatrix} H_x \\ H_y \\ E_z \end{pmatrix} = 0.$$

Media of this type may be called  $s$ -quasi-anisotropic.

For  $p$ -waves at

$$\hat{\epsilon} = \begin{pmatrix} \epsilon_{11} & \epsilon_{12} & \times \\ \epsilon_{21} & \epsilon_{22} & \times \\ 0 & 0 & \times \end{pmatrix}; \quad \hat{\mu} = \begin{pmatrix} \times & \times & 0 \\ \times & \times & 0 \\ \times & \times & \mu_{33} \end{pmatrix}$$

Maxwell's equations for the amplitudes of monochromatic waves take the form:

$$\begin{pmatrix} \epsilon_{11} & \epsilon_{12} & -\frac{c}{\omega}k_y \\ \epsilon_{21} & \epsilon_{22} & \frac{c}{\omega}k_x \\ -\frac{c}{\omega}k_y & \frac{c}{\omega}k_x & \mu_{33} \end{pmatrix} \begin{pmatrix} -E_x \\ -E_y \\ H_z \end{pmatrix} = 0.$$

Media of this type may be called  $p$ -quasi-anisotropic.

Maxwell's equations for  $s$ - and  $p$ -waves are satisfied simultaneously when

$$\hat{\epsilon} = \begin{pmatrix} \epsilon_{11} & \epsilon_{12} & 0 \\ \epsilon_{21} & \epsilon_{22} & 0 \\ 0 & 0 & \epsilon_{33} \end{pmatrix}; \quad \hat{\mu} = \begin{pmatrix} \mu_{11} & \mu_{12} & 0 \\ \mu_{21} & \mu_{22} & 0 \\ 0 & 0 & \mu_{33} \end{pmatrix}.$$

Environments of this type can be called quasi-anisotropic environments in the narrow sense. In media of this type, the  $s$ - and  $p$ -polarization waves do not interact. Algorithms that generalize the Fresnel and Fresnel-Airy formulas [15] are constructed. In anisotropic media, the wave vectors (wavelengths and angles of refraction) for  $s$ - and  $p$ -polarizations may differ. In uniaxial crystals, when the direction of the anisotropy axis is parallel or orthogonal to the plate surface, the  $s$ -wave and  $p$ -polarization waves can be interpreted in terms of the optics of anisotropic media as “ordinary” and “extraordinary” waves. If the anisotropy axis

is directed along the  $z$  axis, then a wave with  $p$ -polarization is an “ordinary” wave and does not depend on anisotropy; a wave with  $s$ -polarization is an “extraordinary” wave and depends on the anisotropy coefficient. If the anisotropy axis lies in the  $(x, y)$  plane, the situation is the opposite. A wave with  $p$ -polarization is an “extraordinary” wave and depends on anisotropy; a wave with  $s$ -polarization is an “ordinary” wave and does not depend on the anisotropy coefficient.

## REFERENCES

1. Landau LD, Lifshitz EM. *Course of Theoretical Physics. Volume 8. Electrodynamics of Continuous Media*. Moscow, Fizmatlit Publ., 2003, 656 p.
2. Fedorov FI. *Optika anizotropnykh sred* [Optics of anisotropic media]. Minsk, AN BSSR Publ., 1958, 380 p.
3. Agronovich VM, Ginzburg VL. *Kristallogoptika s uchetom prostranstvennoy dispersii i teoriya eksitonov* [Crystal optics with spatial dispersion and the theory of excitons]. Moscow, Nauka Publ., 1965, 374 p.
4. Born M, Wolf E. *Principles of optics. Electromagnetic Theory of Propagation, Interference and Diffraction of Light*. Pergamon Press, 1964.
5. Rozenberg GV. *Optika tonkosloynnykh pokrytiy* [Optics of thin-layer coatings]. Moscow, State Publishing House of Fizmatlit, 1958, 570 p.
6. Brekhovskikh LM. *Volny v sloistykh sredakh*. [Waves in stratified medium]. Moscow, Nauka Publ., 1973, 343p.
7. Gorshkov MM. *Ellipsometriya*. [Ellipsometry]. Moscow, Sovetskoe radio Publ., 1974, 200p.
8. Pirozhkov AS, Ragozin EN. Aperiodic multilayer structures in soft X-ray optics. *Phys. Usp.*, 2015, 58 1095-1105.
9. Bushuev VA, Roshchupkina OD. Vliyaniye tolshchin perekhodnykh sloev na effektivnost vzbuzhdeniya tonkoplenochnogo volnovoda [Influence of the thicknesses of transition layers on the excitation efficiency of a thin-film x-ray waveguide]. *Bull. Russ. Acad. Sci., Ser. Phys.*, 2007, 71:59 (in Russ.), <https://doi.org/10.3103/S1062873807010157>.
10. Shutko AM. *SVCH-radiometriya vodnoy poverkhnosti i pochvogruntov* [Microwave radiometry of water and ground surfaces]. Moscow, Nauka Publ., 1986, 188 p.
11. Evtikhov MG. Primeneniye modeli Frenelya-Eyri pri issledovanii rezonansnykh oscillyatsiy ploskikh elektromagnitnykh voln [The application of Fresnel-Airy model for research of resonance oscillations of plane electromagnetic waves]. *Zhurnal Radioelektroniki (elektronny zhurnal)*, 2017, No. 9. Available at <http://jre.cplire.ru/jre/sep17/11/text.pdf> (in Russ.).
12. Bespyatykh YI, Bugaev AS, Dikshtein IE. Poverkhnostnye polyaritony v kompozitnykh sredakh s vremennoy dispersiey dielektricheskoy i magnitnoy pronitsaemostey [Surface polaritons in composite media with temporal dispersion of dielectric and magnetic permeabilities]. *FTT*, 2001, 43(11):2043-2047 (in Russ.).
13. Evtikhov MG, Nikitov SA, Novichihin EP. *Teoreticheskoe issledovanie spektrov TE-voln v mnogosloynnykh plenkakh iz ferromagnitnykh i dielektricheskikh materialov* [Theoretical study of spectra of TE-waves in multilayer films of ferromagnetic and dielectric materials]. Saratov, Saratov University Publishing House, 2013, 68 p.
14. Evtikhov MG. The Snellius and Fresnel ratios for electromagnetic waves with constant linear polarization. *Journal of Communications Technology and Electronics*, 2010, 55(8):855.
15. Evtikhov MG. Fresnel-Airy formulas for quasi-anisotropic media. *Radioelectronics. Nanosystems. Information Technologies (RENSIT)*, 2018, 10(1):91-100, doi: 10.17725/rensit.2018.091.
16. Basharinov AE, Tuchkov LT, Polyakov VM, Ananov N.I. *Izmereniye radioteplovih i plazmennih izlucheniy* [Measurement of radiothermal and

- plasma radiation]. Moscow, Sovetskoe radio Publ., 1968, 390 p.
17. Armand NA, Tishchenko YuG, Savorskiy VP, Smirnov MT. O nauchnoy programme kosmicheskikh eksperimentov v khode ekspluatatsii KA "MKA-PN1" [About scientific program of space experiments in the course of exploitation of the space apparatus MKA-PN1]. *Sovremennyye problemy distantsionnogo zondirovaniya zemli iz kosmosa*, 2009, 6(1):15-21 (in Russ.).
  18. Tikhonov VV, Rayev MD, Sharkov EA, Boyarskiy DA, Repina I A, Komarova NYu. Cputnikovaya mikrovolnovaya radiometriya morskogo l'da polyarnykh regionov. Obzor. [Satellite microwave radiometry of sea ice of polar regions. Review]. *Issledovaniye zemli iz kosmosa*, 2016, 4:65-84 (in Russ.).
  19. Golunov VA, Barabanenkov YuN. Radiometricheskie metody izmereniya obshchey otrazhatelnoy sposobnosti, obshchey pronitsaemosti i kogerentnoy pronitsaemosti slabo pogloshchayushchego sloya sluchaynoy diskretnoy sredy v millimetrovom diapazone dlin voln [Radiometric methods of measurement of the total reflectivity, the total transmissivity and the coherent transmissivity of a weakly absorbing random discrete medium layer in the millimeter wavelengths range]. *Proc. Progress In Electromagnetics Research Symp. (PIERS-2012)*. Moscow, Russia, August 19-23, 2012, pp. 1415-1418 (in Russ.).
  20. Golunov VA, Korotkov VA. Radiometricheskoye issledovaniye dielektricheskikh svoystv presnovodnogo l'da v diapazone millimetrovykh voln [Radiometric study of the dielectric properties of freshwater ice in the range of millimeter waves.]. *Preprint №24(499) IRE RAN*, 1988, 24 p. (in Russ.).
  21. Golunov VA, Kuz'min AV, Skulachev DP, Khokhlov GI. Eksperimental'nyye spektry oslableniya, rasseyaniya i pogloshcheniya millimetrovykh voln v sukhom svezhevypavshem snege [Experimental spectra of attenuation, scattering and absorption of millimeter waves in dry freshly fallen snow.]. *Zhurnal radioelektroniki [elektronnyy zhurnal]*. 2016, №9. (in Russ.). URL: <http://jre.cplire.ru/jre/sep16/4/text.pdf>.
  22. Smirnov MT, Yermakov DM, Maklakov SM, Khaldin AA, Maksimov AYe. Eksperiment po distantsionnomu SVCH radiometricheskomu sondirovaniyu Zemli v L-diapazone s malogo kosmicheskogo apparata, pervye rezultaty [Experiment in passive microwave remote sensing of the Earth in L-band from a small satellite, the first results]. *Sovremennyye problemy distantsionnogo zondirovaniya zemli iz kosmosa*, 2013, 10(3):142-149 (in Russ.).
  23. Kaleschke L, Tian-Kunze X, Maaß N, Mäkynen M, Drusch M. Sea ice thickness retrieval from SMOS brightness temperatures during the Arctic freeze-up period. *Geophysical Research Letters*, 2012, 39:L05501, doi: 10.1029/2012GL050916.
  24. Bordonskiy GS, Gurulev AA, Krylov SD, Tsyrenzhapov SV. Izucheniye voln Ginzburga-Pekara v ledyanykh pokrovakh v mikrovolnovom diapazone [Study of Ginzburg-Pekar waves in ice sheets in the microwave range]. *Sovremennyye problemy distantsionnogo zondirovaniya zemli iz kosmosa*, 2007, 4(1):267-272 (in Russ.).
  25. Bordonskiy GS, Gurulev AA, Krylov SD, Tsyrenzhapov SV, Orlov AO. O koeffitsiyente otrazheniya elektromagnitnykh voln ot granitsy vozdukh-led v santimetrovom diapazone [On the reflection coefficient of electromagnetic waves from the air-ice boundary in the centimeter range]. *Sovremennyye problemy distantsionnogo zondirovaniya zemli iz kosmosa*, 2008, 5(2):30-32 (in Russ.).
  26. Lebedev GA, Sukhorukov KK. Rasprostraneniye elektromagnitnykh i

- akkusticheskikh voln v morskoy l'du [Electromagnetic and acoustic waves propagation in sea ice]. Saint-Petersburg, Gidrometeoizdat Publ., 2001, 81 p.
27. Zatsypina GN. *Svoystva i struktura vody* [Properties and structure of water]. Moscow, Lomonosov MGU Publ., 1974, 168 p.
28. Bogorodskiy VV, Khokhlov GP. Anizotropiya dielektricheskoy pronitsayemosti i udel'nogo pogloshcheniya arkticheskogo dreyfuyushchego l'da v diapazone SVCH [Anisotropy of dielectric constant and specific absorption of arctic drift ice in the microwave range]. *Zhurnal tekhnicheskoy fiziki*, 1977, 47(6):1301-1305 (in Russ.).
29. Liebe HJ, Hufford GA, Manabe T. A model for the complex permittivity of water at frequencies below 1 THz. *International Journal of Infrared and Millimeter Waves*, 1991, 12(7):659-675.
30. Jonathan H. Jiang, Dong L. Wu. Ice and water permittivities for millimeter and sub-millimeter remote sensing applications. *Atmos. Sci. Let.*, 2004, 5:146-151.

# COMPARISON OF INTERPOLATION METHODS WHEN ACHIEVING SUPER-RESOLUTION OF IMAGES BASED ON THE ANALYSIS OF SEVERAL FRAMES

Alexander V. Kokoshkin, Vadim A. Korotkov, Evgeny P. Novichikhin

Kotelnikov Institute of Radioengineering and Electronics of RAS, Fryazino Branch, <http://fire.relarn.ru>  
Fryazino 141190, Moscow Region, Russian Federation  
shvarts65@mail.ru, 138kirill@mail.ru, epnov@mail.ru

*Abstract.* Increasing the resolution based on the use of multiple frames of the same object leads to additional errors. These errors are the result of errors in determining the position of frames, as well as the result of interpolation inaccuracy. In this paper, only errors caused by interpolation are analyzed. We consider the dependence of errors on the number of frames used, the type of interpolation, the type of the original image. It is shown that after averaging over the positions of individual frames, the key dependencies are the dependence of errors on the number of frames and the type of interpolation. It is shown that it does not make sense to analyze interpolation errors immediately after the interpolation procedure. After the required spectral filtering procedure, relatively small interpolation errors will increase significantly. Change and the type of dependence of errors on the number of frames. Therefore, it is advisable to draw the main conclusions based on the analysis of interpolation errors after the filtering procedure. From the point of view of error minimization, it is preferable to use interpolation by a cubic spline and spectral interpolation.

*Keywords:* interpolation, superresolution, image, frame

UDC 621.369

*Bibliography* - 18 references

Received 08.04.2019, accepted 18.04.2019

RENSIT, 2019, 11(1):85-91

DOI: 10.17725/rensit.2019.11.085

## CONTENTS

1. INTRODUCTION (85)
  2. BASIC ASSUMPTIONS (86)
  3. THE FORMATION OF THE TEST IMAGE (87)
  4. INTERPOLATION (87)
    - 4.1. ONE TEST IMAGE (87)
    - 4.2. FIVE TEST IMAGES (89)
  5. CONCLUSION (90)
- REFERENCES (90)

## 1. INTRODUCTION

Increasing the resolution of images obtained by aircraft is an important task. A detailed review of ultra-high resolution (super resolution) methods was given in [1] for reconstructing an image based on several low-resolution frames. The main source of additional information for super-resolution is a number of images of the same object, slightly shifted in successive frames. The pixels of the camera that receives the image have a non-zero size; therefore, the observed pixel value does not correspond to the value at a specific point on the real image, but is averaged over some neighborhood of the point. The object is shifted, as a rule, by a non-integer

number of pixels, therefore, it is possible to use the information of several frames to build a single high-resolution image.

**Fig. 1** shows the scheme of the super-resolution method, which consists of three stages. At the first stage (Fig. 1, numbers 1, 2 and 3) it is determined the shift of low-resolution frames. After determining the frame shift with pixel accuracy, they proceed to the stage of determining the sub-pixel shift (Fig. 1, figure 4). At the same time, the definition of sub-pixel frame shift can be performed in different ways, in particular, using neural networks [2], with a preliminary increase in frames and image search, which, when reduced with taken a motion into the account, will give the minimum total quadratic deviation from the original low-resolution images [3, 4], by directly determining the sub-pixel offset from the position of the maximum of the cross-correlation function of image frames [5]. At the final stage, the existing series of frames are combined with known sub-pixel offsets, which is performed using interpolation [1] (Fig. 1, image 5).

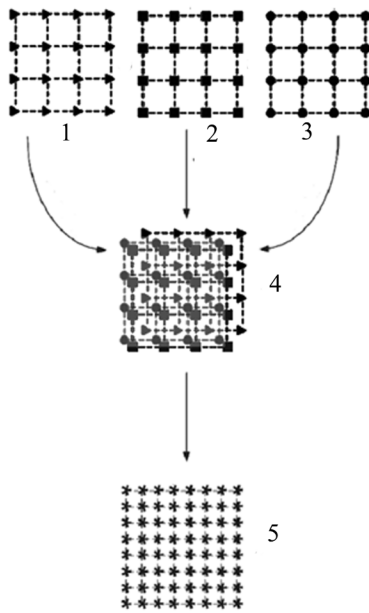


**Fig. 1.** The scheme of the method of super-resolution. The numbers 1, 2, 3 denote low-resolution frames. The number 4 denotes an image of low-resolution frames combined with subpixel offsets. The number 5 corresponds to the interpolated image obtained from image 4.

During of such processing some errors occur, associated with the definition of sub-pixel displacements, and with the properties of the interpolation method itself. The evaluation of errors arising from this is an important, urgent task [6]. Indeed, it is not enough in one way or another (by the method) to obtain an image of an increased resolution, it is also necessary to find out to what extent the result is adequate to reality.

Information on subpixel offsets can be obtained from the resulting low-resolution frames and measurement conditions. For example, if you know the speed and direction of the photo camera, you can ignore the presence of vibration and other uncontrolled factors. Therefore, the magnitude of errors in determining sub-pixel frame offsets largely depends on the measurement conditions controlled by the person. At the same time, interpolation errors depend both on the interpolation method, on the set of sub-pixel offsets, and on the resulting image. Previously, interpolation error estimates were made only when using test images or any assumptions about the properties of images [1, 5-11]. It is assumed that the magnitude of errors for the selected interpolation method depends only on the type of image. At the same time, the algorithm proposed in [7] could allow the creation of a method

to evaluate the interpolation errors of experimental data without using test images and the expected properties of the resulting image. The method [7] does not allow to calculate the exact value of the interpolation error, it can only be used to estimate the possible interpolation error.

The paper [15] analyzed the possibilities of such a method for estimating interpolation errors without using test images and the expected properties of the resulting image to estimate errors in the synthesis of images with superresolution obtained using several frames.

It should be noted that the magnitude of interpolation errors does not determine the magnitude of image reconstruction errors with an increased resolution compared to the original frames. The fact is that after receiving an interpolated image, spectral filtering is performed to improve the quality of the reconstructed high-resolution image [15]. During this filtering, the magnitude of the errors increases. However, depending on the type of interpolation, the same magnitude of interpolation errors can lead to different errors after filtering the interpolated images.

In this paper, we examine the dependence of the magnitude of the difference between the reconstructed image and the number of frames used and the type of interpolation.

We will consider the following interpolation methods:

- a) interpolation of inverse weighted distances (IWD) [11] used in cartography;
- b) interpolation by a cubic spline [10, 16];
- c) spectral interpolation [17];
- d) linear interpolation based on triangulation [18].

## 2. BASIC ASSUMPTIONS

1. The lens forming the image is ideal. The phenomenon of diffraction is absent. Only geometric optics is valid.
2. The limitation of the resolution of images is determined only by the number of photosensitive elements (pixels) per unit area.
3. Light-sensitive pixels are packed tightly and do not have gaps between them. Due to this condition, an image that contains small objects and narrow stripes can be fully restored, since there are no image elements that fall between the pixels.

4. The image within one pixel is averaged evenly.
5. Pixels are square.
6. Subpixel frame shift relative to each other is set.

**3. THE FORMATION OF THE TEST IMAGE**

The purpose of this item is to form a series of low resolution test images from a single high resolution image. A low-resolution image produces a low-resolution photosensitive matrix whose pixel sizes are  $N_p$  times larger than that of the test image. To get one frame, we need to average the test image over  $N_p$  pixels horizontally and vertically. Figure 2 shows the original (128×128 pixels) and averaged ( $N_p = 4$ ) image of the “Bishkek 2,512” aerial photograph. The averaged image demonstrates the possible image quality with perfect recovery from  $N_p$  frames.

When forming a test image, suppose that individual frames are formed along the horizontal axis, but a sub-pixel offset occurs along both axes at the same time.

From the average test image to form one frame, we can take each  $N_p$  pixel horizontally and vertically. We start counting the pixels of the first frame from the upper left corner. The beginning of each subsequent frame occurs with a horizontal and vertical shift. The magnitude of the shift may not to be an integer one and to lay within the limits multiplied by  $N_p$ . To ensure no integer shift, interpolation must be applied. If the shift is greater than  $N_p$ , then we make a combination with pixel accuracy as in [5].

Thus, when modeling a quasi-continuous image, it is proposed to take a discretization step for each coordinate  $N_p$  times smaller than matrix photodetectors are formed. When processing a digital image (with a large, i.e., “single” step), it is

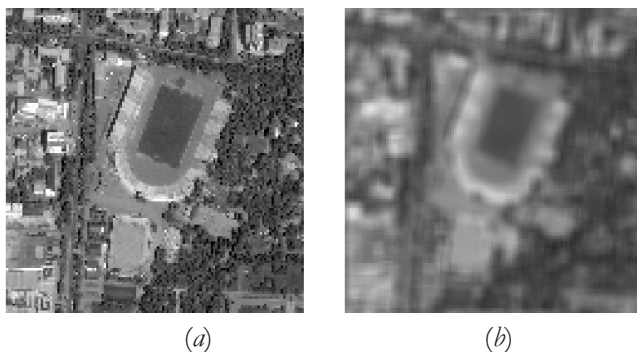


**Fig. 2.** The original image (a) is 128×128 pixels and averaged (b).

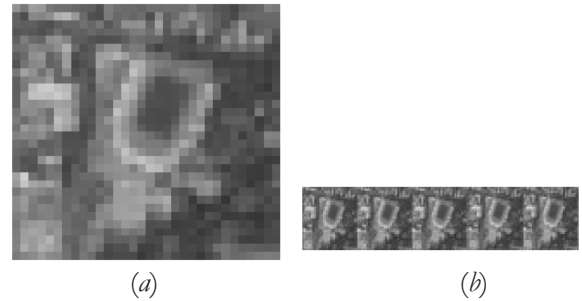


**Fig. 3.** Images: a) - the first frame; b) - the first  $N = 5$  frames out of 16 located in series with each other.

proposed to consider as a super-resolution a return to this small step.

All the frames obtained in the above manner can be represented in the form of a general picture - Fig. 3 (fragment of Fig. 2b).

Upon receipt of Fig. 3, the matrix of shifts  $S_m$  of frames relative to the first frame was set:

At this stage, the formation of the test image is completed. Further we will use only Fig. 3b and Table 1.

**4. INTERPOLATION**

**4.1. ONE TEST IMAGE**

Based on the specified subpixel shifts  $S_m$  and a series of consecutive frames (Fig. 3b), you can use interpolation to obtain an image with a resolution larger than that on the original frames.

**Fig. 4** presents the interpolation results obtained on the basis of 5 frames from the image of Fig. 3b.

Fig. 4 illustrates the fact that the image quality as a result of interpolation is weakly dependent on the type of interpolation. **Table 2** shows the standard deviations of the images shown in Fig. 4 from the averaged source image presented in Fig. 2b.

**Fig. 5** presents the graphs of the standard deviation (RMS) of interpolated (Fig. 5a) and filtered with the help of the Wiener filter [8] (Fig. 5b) images depending on the number of frames used.

The graphs shown in Fig. 5 show that the Wiener filter leads to an increase in the root-mean-square

*Table 1.*

The matrix of shifts of  $S_m$  frames relative to the first frame. 1 line - frame number. 2 and 3 line, respectively, the magnitude of the shifts in the horizontal and vertical in fractions of a pixel.

1	2	3	4	...
0	0.375	0.625	0.875	...
0	0.625	0	0.375	...

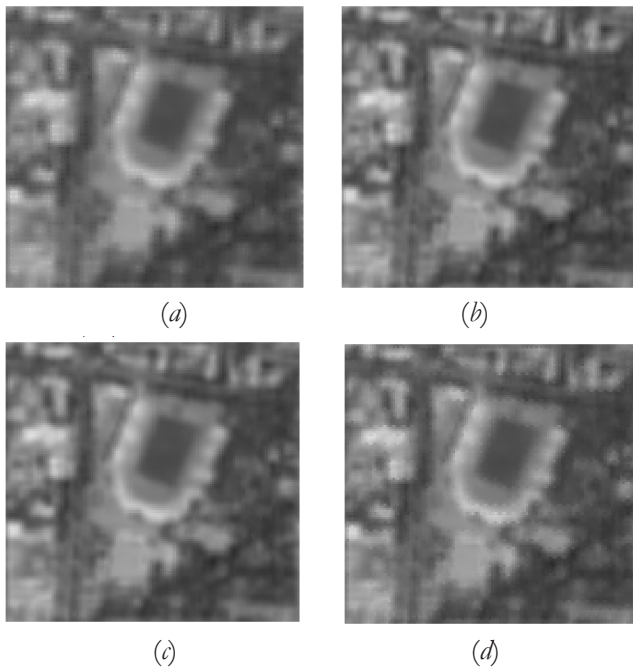


**Fig. 4.** The results of the interpolation of the image obtained from 5 frames Fig. 3b. The images shown in Fig. 4 are the result: a) - interpolation of inverse weighted distances (IWD); b) - interpolation by a cubic spline; c) - spectral interpolation; d) - linear interpolation based on triangulation.

error. This fact is illustrated with the data given in Table 2.

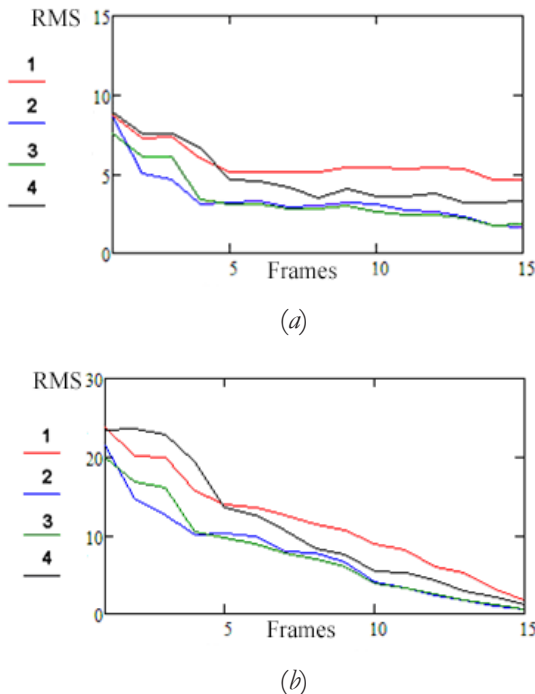


**Fig. 5.** Graphs of the standard deviation of interpolated - (a) and filtered - (b) images depending on the number of frames used. The graphs correspond to: IWD - red line, cubic spline - green line, spectral interpolation - blue line, linear interpolation - black line.

Table 2.

Root-mean-square deviations of images				
	IWD	cubic spline	spectral interpolation	linear interpolation
Average Image	6.296	4.596	4.642	6.101
Filtered image	17.248	14.087	14.693	17.795

**Fig. 6** shows images obtained from images of Fig. 4 using the Wiener filter.

Comparison of images in Fig. 4 and Fig. 6 allows us to conclude that the artifacts that appeared on the interpolated images depend on the type of interpolation used. It should be noted that the minimum standard deviation of the images is obtained with using spline interpolation and spectral interpolation.

**Fig. 7** shows the deviations of the average deviation of the average resolution over 20 realizations of the low resolution Sm frames.

The graphs in Fig. 7 indicate that large standard deviations are caused by the use of IVR and linear interpolation. Smaller mean-square deviations are obtained using cubic spline and spectral interpolation.

The analysis of the graphs in Fig. 7 suggests that under the condition of rationing, the graphs of frame shifts averaged over different implementations

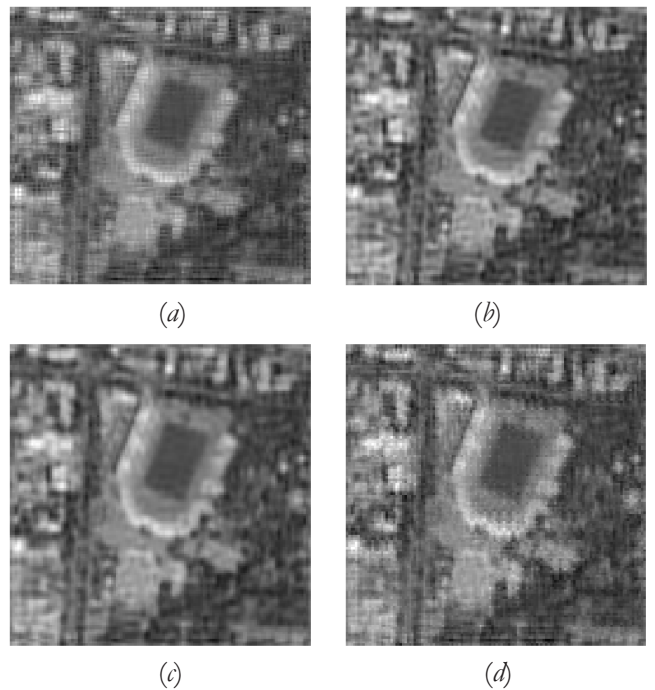


**Fig. 6.** Images obtained from images in Fig.4 using the Wiener filter. Images correspond to: a) - interpolation of inverse weighted distances (IWD); b) - interpolation by a cubic spline; c) - spectral interpolation; d) - linear interpolation based on triangulation.

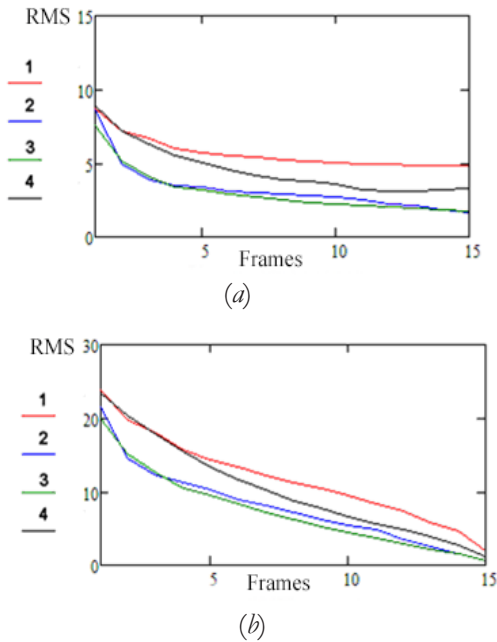


**Fig. 7.** RMS graphs averaged over 20 implementations, interpolated - (a) and filtered - (b) images depending on the number of frames used. The graphs correspond to: IWD - red line, cubic spline - green line, spectral interpolation - blue line, linear interpolation - black line.

of the  $S_m$  matrix will weakly depend on the image and be determined by the type of interpolation.

**4. 2. FIVE TEST IMAGES**

**Fig. 2 and 8** show the original test images used below to test this hypothesis.

**Fig. 9** shows the deviations for the IVR in the case of the test images shown above (Fig. 2, Fig. 8).

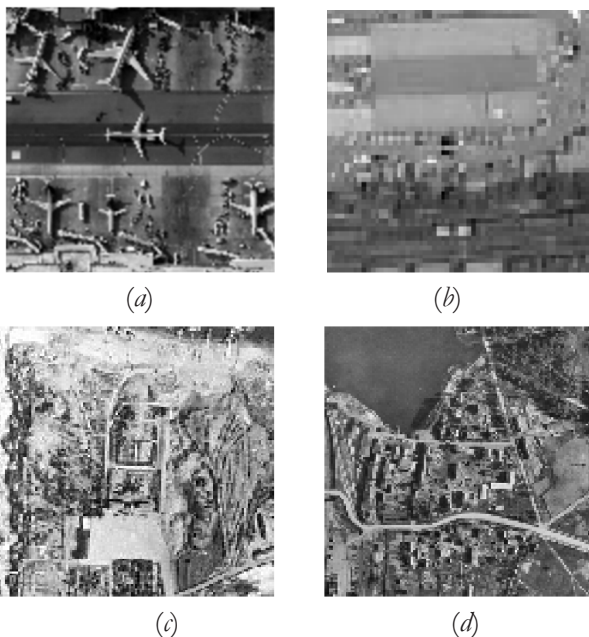


**Fig. 8.** Additional test images.

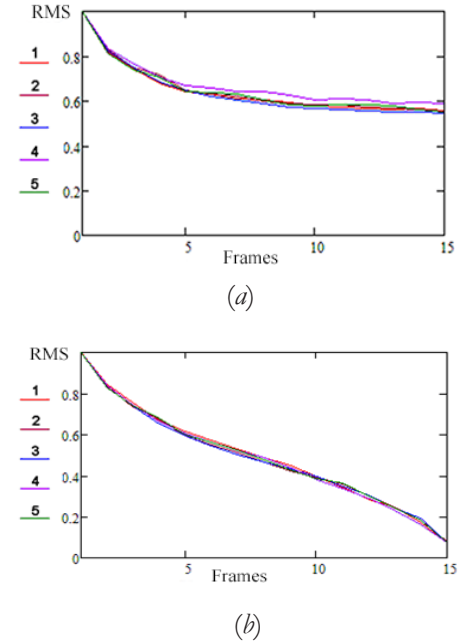


**Fig. 9.** Graphs of normalized standard deviation, averaged over 20  $S_m$  implementations for 5 images, are presented in Fig. 2 and Fig. 8. The graphs corresponding to the images are highlighted in color: Fig. 8a - red line, Fig. 8b - maroon line, Fig. 2a - blue line, Fig. 8g - purple line, Fig. 8d - green line. Fig. 8a and Fig. 8b illustrate respectively the cases of images interpolated and filtered by a Wiener filter.

The graphs in Fig. 9 show that the dependence of the standard deviation on the number of frames used is more pronounced than the dependence on the test image. This allows you to further consider analyzing the dependence of the standard deviation on the number of frames and the type of image, using graphical standard deviations averaged over the images.

Fig. 9 shows the deviations for various types of interpolations depending on the number of frames used. These graphs were obtained by averaging over the images presented in Fig. 2 and Fig. 8 and the corresponding normalization.

The graphs in **Fig. 10** allow us to conclude that if we average the mean distortion of the implementations of the shift matrix  $S_m$  and normalize it to the mean deviation value for one frame, then the dependence of the mean deviation from the type of image is significantly weakened. This makes it possible to predict the value of the normalized standard deviation, depending on the interpolation method and the number of frames used - Fig. 10.

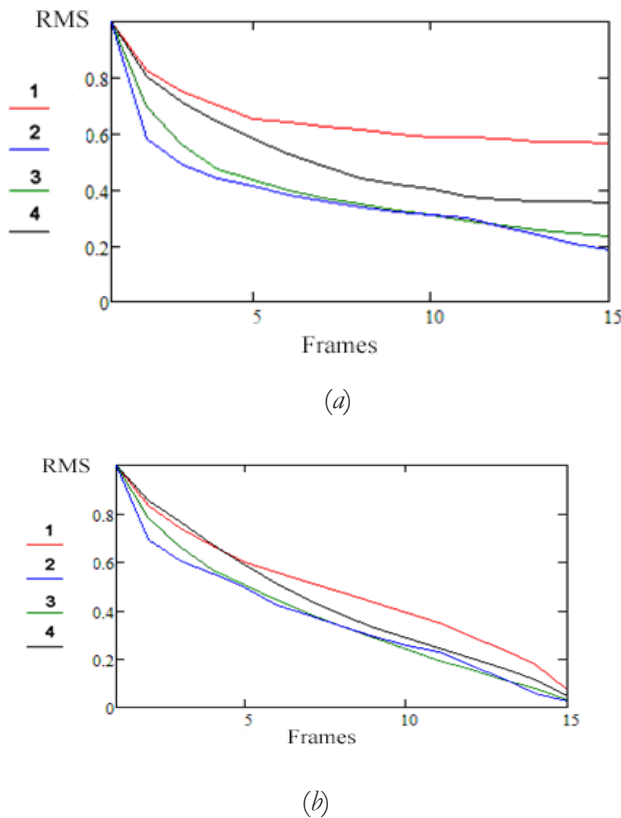


**Fig. 10.** The RMS diagrams, averaged over 20 realizations of  $S_m$  and averaged over 5 images, are presented in Fig.2 and Fig.8. Graphs of the RMS of interpolated - (a) and filtered - (b) images depending on the number of frames used. The graphs correspond to: IWD - red line, cubic spline - green line, spectral interpolation - blue line, linear interpolation - black line.

## 5. CONCLUSION

Using multiple low-resolution frames to produce a high-resolution image requires several steps. The resulting low-resolution frames must be analyzed to determine the amount of displacement relative to each other. The results of solving this non-simple task significantly affect the final result. The second stage corresponds to obtaining a high-resolution image using interpolation based on the already calculated displacement values of low-resolution frames. With an increase in the number of source frames, the deviation decreases. However, the magnitude of the standard deviation depends on the type of interpolation used. Usually interpolation errors are considered when comparing with a test image. But comparison of the average image with the interpolated image does not give a complete picture (Fig. 7a). In our case, it is advisable to consider the standard deviation on the basis of a comparison of the filtered image with the original non-averaged image (Fig. 7b). Such a comparison

suggests that it is advisable to use cubic spline and spectral interpolation. In addition, it follows from Fig. 10 that spectral interpolation can have a certain advantage over interpolation by a cubic spline in the case of small amounts of low-resolution frames used.

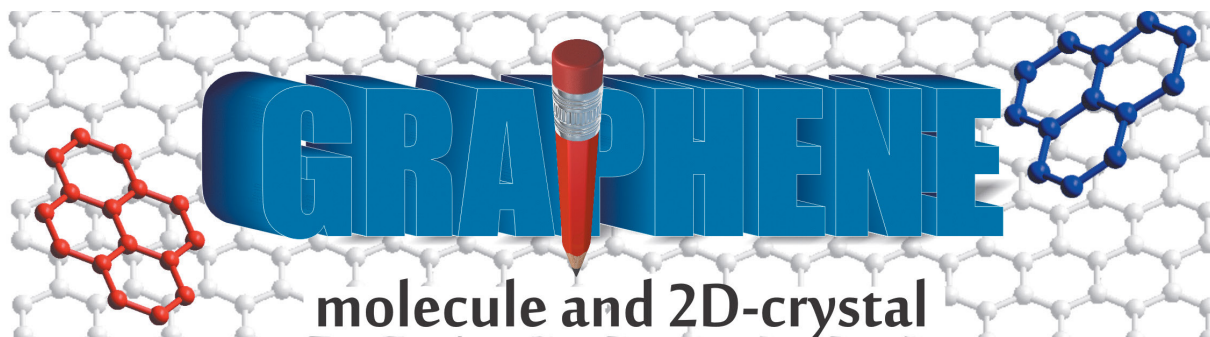
*The work was carried out within the framework of the state task*

## REFERENCES

1. Elham K, Kaveh K, Javadi S. A Survey on Super-Resolution Methods for Image Reconstruction. *Int. J. of Computer Applications*, 2014, 90(3):32-39.
2. Mishin AB. Method, algorithm and adaptive image processing device based on CMOS video sensors using neural-like structures. *Thesis for the degree of candidate of technical sciences. Southwestern State University, Kursk*, 2014.
3. Markelov KS. Model of increasing informativeness of digital images based on the super-resolution method. *Engineering Bulletin 77-48211/552065, MSTU MIREA Publ.*, 2013, № 03 (in Russ.).
4. Nasonov AV. Regularizing methods for improving image resolution and super resolution. *Thesis for the degree of Candidate of Physical and Mathematical Sciences. Lomonosov Moscow State University Publ.*, Moscow, 2011.
5. Goshin EV, Kotov AP, Fursov VA. Dvukhetapnoe formirovanie prostranstvennogo preobrazovaniya dlya sovmeshcheniya izobrazheniy [Two-stage formation of spatial transformation for image alignment]. *Komp'yuternaya optika*, 2014, 38(4):886-891 (in Russ.).
6. Ermakov DM, Sharkov EA, Chernushich AP. Assessment of the accuracy of the interpolation scheme of satellite radiothermovision. *Modern problems of remote sensing of the Earth from space*. 2015, 12(2):77-88.
7. Kokoshkin AV, Korotkov VA, Korotkov KV, Novichikhin EP. On the use of a simple method for estimating the interpolation error of experimental data. *Zhurnal radioelektroniki [online journal]*, 2016, №9, Access Mode: <http://jre.cplire.ru/jre/sep16/5/text.pdf>. (the date of the appeal is May 23, 2017) (in Russ.).
8. Gonzalez R, Woods R. *Digital Image Processing*. Moscow, Technosphaera Publ., 2005, 1071 p.

9. Shary SP. *Course of computational methods*. Novosibirsk, ICT SB RAS Publ., 2016.
10. Forsyth J, Malcolm M, Mowler C. *Machine methods of mathematical calculations*. Moscow, Mir Publ., 1980, 279 p.
11. Shutko AM, Alexander Haldin, Vladimir Krapivin, Evgenij Novichikhin, Igor Sidorov, Yuriy Tishchenko, Roland Haarbrink, Georgi Georgiev, Rumiana Kancheva, Hristo Nikolov, Tommy Coleman, Fr. Camps Carmona. Microwave Radiometry in the High-Sealage and Dangerously High Groundwaters. *Journal of Telecommunications and Information Technology*, 2007, 1:76-82.
12. Ivanov VA, Kirichuk VS, Kosykh VP. Estimation of subpixel shift of discrete images. *Avtometriya*, 2007, 43(3):15-30 (in Russ.).
13. Gudkov SA. The method of processing signals eddy current sensor control parameters of dispersed media. *XVIII International Scientific and Practical Conference "Modern technology and technology", Section 2: Instrumentation*, Tomsk, 2012, pp. 183-184.
14. Babak VP, Ponomarenko PV. Lokalizatsiya mesta polozheniya skvoznykh defektov po signalam akusticheskoy emissii [Localization of the location of through defects by acoustic emission signals]. *Automatics, automatization, electrotechnical complexes and systems*, 2007, 1(19):39-46 (in Russ.).
15. Kokoshkin AV, Korotkov VA, Korotkov KV, Novichikhin EP. Otsenka oshibok sinteza izobrazheniy s superrazresheniem na osnove ispol'zovaniya neskol'kikh kadrov [Evaluation of image synthesis errors with SUPER resolution based on the use of multiple frames]. *Komp'yuternaya optika*, 2017, 41(5):701-711 (in Russ.).
16. Nesterenko EA. Possibility of using spline surfaces for surface plotting by results of surveying. *Journal of Mining Institute (St. Petersburg)*, 2013, 204:127-133 (in Russ.).
17. Kokoshkin AV, Korotkov VA, Korotkov KV, Novichikhin EP. Using the Fourier spectrum of the image for retouching and restoring the missing parts of the image distorted by the hardware function. *Zhurnal radioelektroniki [online journal]*. 2016, №7, Access Mode: <http://jre.cplire.ru/jre/jul16/4/text.html> (in Russ.).
18. Skvortsov AV. *Delaunay triangulation and its application*. Tomsk, TSU Publ., 2002. 128 p.

## Third Russian Conference



## molecule and 2D-crystal

August 5 - 9, 2019

Russian Federation, 630090 Novosibirsk

<http://grapheneconf.nsu.ru>

PACS: 01.10 Fv

DOI: 10.17725/rensit.2019.11.092

**GENERAL CHAIRS:**

**ALEXANDER V. OKOTRUB**  
*Dr.Sci. Phys&Math, prof., NIIC SB RAS, Novosibirsk*  
 spectrum@niic.nsc.ru

**PROGRAM COMMITTEE**

**VALERY I. BUKHTIYAROV**  
*Corr. Memb. RAS, BIC SB RAS, Novosibirsk*

**VIKTOR A. BYKOV**  
*Dr.Sci. Techn., prof., NIIFP — NTMDT, Zelenograd*

**SERGEY P. GUBIN**  
*Dr.Sci. Chem, prof., IGIC RAS, Moscow*

**ALEXANDER V. ELETSKY**  
*Dr.Sci. Phys&Math, prof., NRC KI, Moscow*

**ZINFER R. ISMAGILOV**  
*Corr. Memb. RAS, ICCMS SB RAS, Novosibirsk*

**VLADIMIR L. KUZNETSOV**  
*PhD Chem., BIC SB RAS, Novosibirsk*

**ALEXANDER V. LATYSHEV**  
*Corr. Memb. RAS, ISP SB RAS, Novosibirsk*

**SERGEY A. MAKSIMENKO**  
*Dr.Sci. Phys&Math, prof., BSU, Minsk*

**KONSTANTIN S. NOVOSELOV**  
*PhD, prof., University of Manchester, United Kingdom*

**ALEXANDER N. OBRATZOV**  
*Dr.Sci. Phys&Math, prof., MSU, Moscow*

**ELENA D. OBRATZOVA**  
*PhD Phys&Math, GPI RAS, Moscow*

**VLADIMIR P. FEDIN**  
*Corr. Memb. RAS, NIIC SB RAS, Novosibirsk*

**LEONID A. CHERNOZATONSKII**  
*Dr.Sci. Phys&Math, prof., IBCP RAS*

**GM2dC'2019/NOVOSIBIRSK SECRETARIAT**

**IRINA V. ANTONOVA**  
*Dr.Sci. Phys&Math, ISP SB RAS, Novosibirsk*  
 antonova@isp.nsc.ru

**ELENA YU. BUSLAEVA**  
*Dr.Sci. Chem., IGIC RAS, Moscow*  
 eyubuslaeva@inbox.ru  
 +7 495 633 8559

**YULIYA V. FEDOSEEVA**  
*PhD Phys&Math, NIIC SB RAS, Novosibirsk*  
 fedoseeva@niic.nsc.ru  
 graphene@niic.nsc.ru  
 +7 383 330 5352 (NIIC)

*Novosibirsk State University  
 Nikolaev Institute of Inorganic Chemistry SB RAS  
 Borekrov Institute of Catalysis SB RAS  
 Rzhanov Institute of Semiconductor Physics SB RAS  
 Kurnakov Institute of General and Inorganic Chemistry RAS*

GM2dC'2019 - brand of the Russian conference "GRAPHENE – MOLECULE AND 2D CRYSTAL", devoted to the results and prospects of research on graphene and related materials. Conference is purposely interdisciplinary, as the problem itself. One of the conference objectives is to develop a common language (terminology) in the discussion of the unique properties of graphene for professionals from various fields of science, a single view of the prospects in this direction.

Conference language is Russian and English  
 (with synchronical translation)

**GMC SUGGESTED TOPICS**

- Chemical and CVD synthesis of graphene and related materials
- Chemical modification of graphene and hybrid 2D materials
- Weil's topological insulators and semimetals
- Diagnostics of graphene and other 2D materials
- Theory, structure and modeling of properties of graphene and related low-dimensional materials
- Graphene electronics
- Mechanical and electromechanical properties and applications
- Optical and Electromagnetic Properties and Applications
- The use of graphene and related materials in electrochemistry

**IMPORTANT DATES**

Call for applications	January 01. 2019
Acceptance of theses	March 01. 2019
Payment of the registration fee	May 01. 2019
Acceptance of articles in the Journal of Structural Chemistry	September 10. 2019

**VENUE**

Novosibirsk, Academgorodok, Novosibirsk State University

**ACCOMMODATION OF PARTICIPANTS**

Hotel "Golden Valley" (with transfer from the airport to the hotel)



Radioelectronics. Nanosystems. Information Technologies (abbr. RENSIT)

Certificate El. no. FS77-60275 on 19.12.2014 of the Ministry of Telecom and Mass Communications of Russian Federation, Moscow

ISSN: 2414-1267online. [Http://www.rensit.ru](http://www.rensit.ru). Publisher - Vladimir I. Grachev. 2019, 30 April.

Computer printing, page-proofs, graphics, photos of work - the editors RENSIT.